Power System Stability Improvement with Decommissioned Synchronous Machine Using Koopman Operator Based Model Predictive Control

Xiawen Li

Dissertation submitted to the faculty of the Virginia Polytechnic Institute and State University in partial fulfillment of the requirements for the degree of

Doctor of Philosophy

In

Electrical Engineering

Jaime De La Reelopez, Chair
Virgilio A Centeno
Rolando Burgos
Steve C Southward
Robert P Broadwater
Chetan Mishra

July 29th, 2019

Blacksburg, VA

Keywords: Inertia, Koopman Operator, Time-Delay Embedding, Model Predictive Control

Power System Stability Improvement with Decommissioned Synchronous Machine Using Koopman Operator Based Model Predictive Control

Xiawen Li

ABSTRACT

Traditional generators have been decommissioned or replaced by renewable energy generation due to utility long-standing goals. However, instead of flattening the entire plant, the rotating mass of generator can be utilized as a storage unit (inertia resource) to mitigate the frequency swings during transient caused by the renewables. The goal of this work is to design a control strategy utilizing the decommissioned generator interfaced with power grid via a back-to-back converter to provide inertia support. This is referred to as decoupled synchronous machine system (DSMS). On top of that, the grid-side converter is capable of providing reactive power as an auxiliary voltage controller. However, in a practical setting, for power utilities, the detailed state equations of such device as well as the complicated nonlinear power system are usually unobtainable making the controller design a challenging problem. Therefore, a model free, purely data-driven strategy for the nonlinear controller design using Koopman operator-based framework is proposed. Besides, the time delay embedding technique is adopted together with Koopman operator theory for the nonlinear system identification. Koopman operator provides a linear representation of the system and thereby the classical linear control algorithms can be applied. In this work, model predictive control is adopted to cope with the constraints of the control signals. The effectiveness and robustness of the proposed system are demonstrated in Kundur two-area system and IEEE 39-bus system.

Power System Stability Improvement with Decommissioned Synchronous Machine Using Koopman Operator Based Model Predictive Control

Xiawen Li

GENERAL AUDIENCE ABSTRACT

Power system is facing an energy transformation from the traditional fuel to sustainable renewable such as solar, wind and so on. Unlike the traditional fuel energized generators, the renewable has very little inertia to maintain frequency stability. Therefore, this work proposes a new system referred to as decoupled synchronous machine system (DSMS) to support the grid frequency. DSMS consists of the rotating mass of generator and a back-to-back converter which can be utilized as an inertia resource to mitigate the frequency oscillations. In addition, the grid-side converter can provide reactive power to improve voltage performance during faults. This work aims to design a control strategy utilizing DSMS to support grid frequency and voltage. However, an explicit mathematical model of such device is unobtainable in a practical setting making data-driven control the only option. A data-driven technique which is Koopman operator-based framework together with time delay embedding algorithm is proposed to obtain a linear representation of the system. The effectiveness and robustness of the proposed system are demonstrated in Kundur two-area system and IEEE 39-bus system.

Acknowledgments

I would like to thank Dr. Jaime De La Ree for providing me the opportunity to be his student and guiding me throughout the entire doctoral studies. Dr. Jaime De La Ree has been my professor, mentor and friend. He has the very insight of power system and therefore provides me great directions and suggestions of research. Thanks to his encouragement, I have gained confidence to deal with all the difficulties in the past, and also, I am ready for the future challenges. I would like to express my sincere gratitude to Dr. Virgilio Centeno for giving me the opportunity to be a member of Power and Energy Center. Furthermore, I am fortunate to invite Dr. Rolando Burgos, Dr. Steve Southward, Dr. Robert Broadwater and Dr. Chetan Mishra to be my committee advisors.

Last but most importantly, I want to thank my fiancé and my dear families who are always supporting me not only in study but also in my daily life.

Table of Contents

List of figures

List of Tables

Chapter 1 Introduction

1.1 Motivation and Background

1.1.1 Problems Introduced by Renewable Integration

In recent years, atmospheric pollutants such as carbon monoxide, sulfur oxide, nitrogen dioxide are mainly produced by conventional fossil fuel power generations, leading to severe environmental hazard likes haze, acid rain, greenhouse effect and etc [1], [2]. Particularly, about 2.2 billion tons of carbon dioxide has been emitted by fossil fuel power plants annually [2]. Therefore, due to the recent EPA regulations [3], power utilities are forced to decommission more and more conventional fossil fuel units. On top of that, owing to many states renewable-friendly policies, the penetration of renewable energy resources (RESs) is expected to increase. In order to undertake the enormous need for energy while controlling pollutions growth, more and more countries have been involved in facilitating the penetration of RESs. For instance, in February 2019, U.S. Energy Information Administration (EIA) updated renewable portfolio standards (RPS) [4]. Washington D.C. and New Jersey increased their RPS goals to 100% and 50% share of sales by 2040 and 2030 respectively [4]. Besides, California has set a higher RPS target which is up to to a 60% renewable generation share of sales by 2030. In addition, by 2045, California is expected to have a total of 100% carbon-free power [4]. Figure 1.1 provides more details RPS targets for selected states. As a result, more renewable electricity generations are foreseeable in the next decades.

However, the increasing penetration of RESs is expected to introduce serious reliability concerns, such as voltage and frequency stability issues [5]. Particularly, frequency stability is the major one, appearing a great challenge to power system operators. Conventionally, synchronous generators maintain the generation and load balance by means of mechanical torque from governors. Due to the high moment of inertia of these conventional rotating masses, the frequency oscillations are maintained within a small range such that the transient stability can be assured. However, unlike the traditional system, RESs have very low or even non-existent inertial response unless those grid support functionalities are built in specifically [2], [6].

Table 1-1 2010-2050 Renewable portfolio standards targets of percent of retail electricity sales for selected states [4]

States	RPS 1st target	RPS 2nd target
Connecticut	27% by 2020	48% by 2030
New Jersey	24% by 2024	50% by 2030
Massachusetts	46% by 2050	55% by 2050
California	50% by 2030	100% by 2045
Washington, D.C.	50% by 2032	100% by 2032

That being said, currently, it is difficult to enforce those functionalities especially for widely distributed resources. Eventually, this becomes a serious issue, especially for systems with high penetration of PV generation since the yearly electricity peaks are during light load months leading to scenarios where a high percentage of the generations online is effectively inertialess and thus making the frequency less robust to disturbances [6], [2]. Although the variable speed wind turbines have a certain amount of inertia, they are usually decoupled from the network by power converters unless extra controls are designed [6]. Furthermore, according to the current trends in the growth of these generations, this problem is expected to magnify [7].

To provide sufficient moment of inertia, the fast frequency control techniques have been studied in many research. [8]–[10] emulate the inertia response of conventional generators using power converters. In order to have partial reserved energy to regulate frequency, the work in [11] runs PV generation at a so-called deloading operating condition which is away from the Maximum Power Point Tracking (MPPT) point. Besides, the cooperation between energy storage systems (ESSs) and variable-speed wind turbine generators (WTGs) is commonly used to improve transient frequency performance [12].

Regarding the voltage control, power electronic converters are capable of regulating terminal bus voltages by running at P-V or P-Q mode which can be achieved by modulating switching-signal generators [13]. In addition, the switched or static shunt capacitors are typically installed on the bus to provide auxiliary reactive power to regulate bus voltage [14].

1.1.2 Distributed Control

Communication infrastructure of a large-scale system is usually cost prohibitive. As a result, wide area control in large-scale systems is usually not a practical option. Unlike the wide area control, the scope of distributed control technologies is within the area of the controlled unit where it is distributed in. When performing distributed control methods, the power system operators only require partial parameters from others through communication. Since distributed control algorithms require only limited amounts of knowledge shared between agents, cybersecurity can also be improved while reducing the costly communication facilities. In addition, distributed algorithms have the ability to perform faster computation and to solve bigger problem size. Moreover, distributed control has higher robustness against the failure of other agents [15].

1.1.3 Model Predictive Control

Nearly every control application imposes constraints on the controls signals and the system states. The existence of hard constraints results in the need for control strategy for dealing with them. Normally, without the corresponding solution of Hamilton Jacobi-Bellman differential or difference equation, the feedback solution for the objective function satisfying all of those constraints cannot be found analytically. However, solving Hamilton differential equation is an extremely difficult task [16], [17]. Model predictive control (MPC) algorithm circumvents the close solution by repeatedly solving a finite-window open-loop optimization problem using the current states of the system as the initial states. This characteristic makes itself one of the few suitable options. [18]–[20] show the effectiveness of MPC. Power systems are very typical nonlinear systems [21] requiring models for predicting the evolutional trajectory of the system states which is called as nonlinear MPC [17]. However, nonlinear MPC is computationally prohibitive and that is why a lot of researchers have been using linear MPC for predicting and controlling nonlinear dynamical systems [22], [23]. In order to implement linear MPC in regions further from the equilibrium, a linear representation of the nonlinear system in a large region is needed to improve the accuracy of prediction for the nonlinear system.

1.1.4 Koopman Operator

That being said, due to the inherently nonlinear nature of the power system and uncertain characteristics of the converter-interfaced generation, an accurate explicit model of the power grid is of the great challenge making a data driven control the only practical option [6]. The Koopman operator theory is a popular and powerful tool which is capable of the analysis and prediction of the nonlinear dynamical system using measurement data [24]–[28] making it a data driven approach. Koopman operator theory has also been utilized in power system recently such as power system coherency identification, electrical drive speed control, transient stability control and so on [29]–[32]. Basically, Koopman operator utilizes a set of scalable observable functions to reconstruct the underlying dynamical system from measurement data in a linear but high-dimension space [25] i.e. the system is linear in this new space which makes it an attractive option to be used with linear MPC. The effectiveness of the Koopman operator-based MPC has been found in [25], [31], [33]

1.1.5 Time-Delay Embedding

A classical method for nonlinear system identification is to use time-delayed embedding coordinates [33]. Time delay embedding is able to unfold the underlying dynamics which makes itself a good choice of observable which is required by the Koopman operator theory. The process of going from observed measurements to a dynamical model is fundamental in engineering. Typically, Takens embedding theorem provides the theoretical basis of nearly all analysis of time series embedding analysis. In general, by constructing a new state space by means of consecutive observed scalar time series values, we will be able to reconstruct the underlying unknown dynamical system [34]. In Takens theory, it is assumed that the dynamical system is autonomous, which means that the system is independent of time and of any external influence. However, this is very rare in many real systems. Especially in power system, in order to obtain stability, many controllers have been deployed. Consequently, an extended version of Takens theory which is generalized to input-output systems was introduced in [35]. The main idea drawn from this paper is that an extended phase space can be reconstructed from the input and output time series [35].

The embedding dimension d and the delay time τ are the key factors to reconstruct the system successfully. In the past few decades, a number of methods have been developed for determining

the optimal embedding dimension and delay time τ. Mutual information has been widely used to calculate the optimal time delay of the sampled data. It aims to seek an optimal time delay such that the time series data and its time-shifted version is independent of each other. Regarding the embedding dimension, in Takens theory, the embedding dimension *d* should be sufficiently large so that this condition $d \geq 2D_n + 1$ is satisfied, where D_n is the dimension of the original system. However, it is noticed that this is a sufficient but not necessary condition [34]. Besides, the lowest embedding dimension is preferred in practice while the reconstructed diffeomorphism remains. Kennel *et al* introduced False Nearest Neighbor (FNN) algorithm. It was developed based on the fact that the point identified as the nearest neighbor of a certain point in a too small embedding space is actually far apart in the original phase space. While having a large enough embedding space, all neighbors of every point will be true neighbors [34]. However, the subjective choice of the parameter R_{tol} and A_{tol} used as the criterion to distinguish false neighbors may lead to different results. The average FNN proposed by Cao in [36] overcomes this shortcoming. Cao computes how the average distances between the nearest neighbors vary as the dimension increasing from *d* to *d*+1 other than evaluating the validity of neighbors. The smallest embedding dimension which properly unfolds the dynamics of the system is taken as the one which stops the change. It has been shown in [37], [38] that FNN also works in the input-output system by including input data into the delay embedding vectors.

1.2 Research Objective and Significance

My proposed approach utilizes the rotating mass of a decommissioned conventional generator as a storage unit interfacing it to the power grid via the AC-DC-AC converter configuration for frequency control. Time delay embedding together with Koopman operator theory is utilized to transform the nonlinear dynamical system to a linear system. In order to determine the optimal time delay and embedding dimension of the embedding coordinates, the mutual information method and the Cao's method are extended to the multivariate input-output system. Building upon the recent development of the Koopman model predictive control (KMPC) framework [33], a robust feedback control of the local frequency of the DSMS is proposed. Besides, KMPC is applied to design the voltage controller using the reactive power provided by the grid-side converter. The locally trained KMPC is also able to work with another KMPC located in another

area without negative interaction. Furthermore, KMPC is sufficiently robust to cope with system topology changes.

1.3 Dissertation Organization

This dissertation is organized as follows.

Chapter 2 provides the derivation of the dynamical models of the synchronous generator, the rotating mass as well as the back-to-back converter.

Chapter 3 gives the methodology for the controller design of both the back-to-back converter and rotating mass.

Chapter 4 presents the fundamental of nonlinear system, Koopman operator theory, and the data-driven numerical method to estimate Koopman operator.

Chapter 5 illustrates the time-delay embedding technique. The algorithm named as Auto Mutual Information to determine the optimal time lag is explained. In addition, the algorithm for determining the minimum embedding dimension named as False Nearest Neighbor and its extension are presented. These methods are extended to cope with the input-output system.

Chapter 6 briefly introduces the model predictive control. The objective functions along with the constraints are given. The procedure for designing the Koopman operator-based model predictive control is also provided.

Chapter 7 showcases the effectiveness of the proposed method in power system sample cases. The first case is the classical Kundur two-area system and the second case is the IEEE 39-bus system. The comparisons between the true measurements and predictions are provided. Different fault scenarios are applied to the system with generator replaced by the proposed system and controllers, the system without controllers, and the original system respectively.

Chapter 8 provides the conclusions of this dissertation as well as the research directions in the future.

Chapter 2 System Models

2.1 Reference frame theory

In the study of power systems as well as power electronics systems, we are used to referring all the variables to a common reference frame by means of applying mathematical transformations. This creates a lot of convenience for analyzing the behaviors and designing the controllers of the time-varying systems. In order to obtain the time-invariant reference frame, we usually transform *abc* reference frame into *qd0* reference frame via the well-known Park's transformation [39].

We first consider three-phase variables expressed as

$$\vec{x}_{abc} = \begin{bmatrix} x_a \\ x_b \\ x_c \end{bmatrix} = \begin{bmatrix} X_m \cos(\theta_q) \\ X_m \cos(\theta_q - \frac{2\pi}{3}) \\ X_m \cos(\theta_q + \frac{2\pi}{3}) \end{bmatrix} = \begin{bmatrix} X_m \cos(\omega_e t) \\ X_m \cos(\omega_e t - \frac{2\pi}{3}) \\ X_m \cos(\omega_e t + \frac{2\pi}{3}) \end{bmatrix} \tag{2.1.1}$$

where $\theta_q = \omega_e t$ with the assumption that *q*-axis is coincided with *a*-axis at time t = 0s. In other words, the initial angle between q-axis and a-axis is 0.

The relationship between *abc*-frame and *qd0*-frame is given in Figure 2.1. According to this figure, we can derive the *qd0* quantities as

$$\vec{x}_{qd0} = \begin{bmatrix} x_q \\ x_d \\ x_0 \end{bmatrix} = T_{qd0/abc} \vec{x}_{abc} \tag{2.1.2}$$

where the transformation matrix is defined as

$$T_{qd0/abc} = \frac{2}{3} \begin{bmatrix} \cos\omega_e t & \cos(\omega_e t - \frac{2\pi}{3}) & \cos(\omega_e t + \frac{2\pi}{3}) \\ \sin\omega_e t & \sin(\omega_e t - \frac{2\pi}{3}) & \sin(\omega_e t + \frac{2\pi}{3}) \\ \frac{1}{2} & \frac{1}{2} & \frac{1}{2} \end{bmatrix} \tag{2.1.3}$$

The inverse transformation is given by

$$\vec{x}_{abc} = T^{-1}_{qd0/abc}\vec{x}_{qd0} \tag{2.1.4}$$

where the inverse transformation matrix is defined as

$$T^{-1}_{qd0/abc} = \begin{bmatrix} \cos\theta_q & \sin\theta_q & 1 \\ \cos(\theta_q - \frac{2\pi}{3}) & \sin(\theta_q - \frac{2\pi}{3}) & 1 \\ \cos(\theta_q + \frac{2\pi}{3}) & \sin(\theta_q + \frac{2\pi}{3}) & 1 \end{bmatrix} \tag{2.1.5}$$

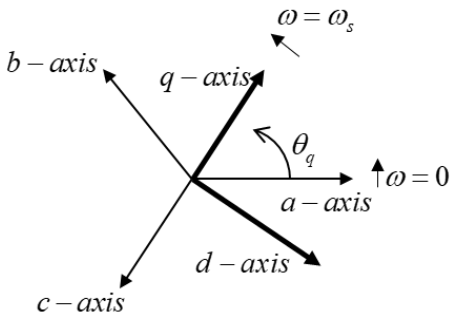

Figure 2.1 *abc*-frame v.s. *qd0*-frame

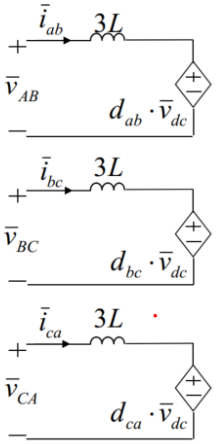

Figure 2.2 *abc* three-phase circuit

Consider the three-phase circuits given in Figure 2.2. The corresponding differential equations are

$$L\frac{di_a}{dt} = -i_a r + v_a \tag{2.1.6}$$

$$L\frac{di_b}{dt} = -i_b r + v_b \tag{2.1.7}$$

$$L\frac{di_c}{dt} = -i_c r + v_c \tag{2.1.8}$$

We can write (2.1.6) to (2.1.8) in a state-space form

$$\begin{bmatrix} \frac{di_a}{dt} \\ \frac{di_b}{dt} \\ \frac{di_c}{dt} \end{bmatrix} = \begin{bmatrix} \frac{-r}{L} & 0 & 0 \\ 0 & \frac{-r}{L} & 0 \\ 0 & 0 & \frac{-r}{L} \end{bmatrix} \begin{bmatrix} i_a \\ i_b \\ i_c \end{bmatrix} + \frac{1}{L} \begin{bmatrix} v_a \\ v_b \\ v_c \end{bmatrix} \tag{2.1.9}$$

We have the following coordination transformation relationships according to inverse Park's transformation

$$\begin{cases} \vec{i}_{abc} = T_{qd0/abc}^{-1} \vec{i}_{qd0} \\ \frac{d\vec{i}_{abc}}{dt} = \frac{dT_{qd0/abc}^{-1} \vec{i}_{qd0}}{dt} = \frac{dT_{qd0/abc}^{-1}}{dt} \vec{i}_{qd0} + T_{qd0/abc}^{-1} \frac{d\vec{i}_{qd0}}{dt} \\ \vec{v}_{abc} = T_{qd0/abc}^{-1} \vec{v}_{qd0} \end{cases} \tag{2.1.10}$$

Substituting the above equations into (2.1.9), we have

$$\frac{dT_{qd0/abc}^{-1}}{dt} \vec{i}_{qd0} + T_{qd0/abc}^{-1} \frac{d\vec{i}_{qd0}}{dt} = \begin{bmatrix} \frac{-r}{L} & 0 & 0 \\ 0 & \frac{-r}{L} & 0 \\ 0 & 0 & \frac{-r}{L} \end{bmatrix} T_{qd0/abc}^{-1} \vec{i}_{qd0} + \frac{1}{L} T_{qd0/abc}^{-1} \vec{v}_{qd0} \tag{2.1.11}$$

$$\xrightarrow{\times T_{qd0/abc}} \frac{d\vec{i}_{qd0}}{dt} = -T_{qd0/abc} \frac{dT_{qd0/abc}^{-1}}{dt} \vec{i}_{qd0} + \begin{bmatrix} \frac{-r}{L} & 0 & 0 \\ 0 & \frac{-r}{L} & 0 \\ 0 & 0 & \frac{-r}{L} \end{bmatrix} \vec{i}_{qd0} + \frac{1}{L} \vec{v}_{qd0} \tag{2.1.12}$$

According the trigonometric relationships given in [40], we have

$$T_{qd0/abc}\frac{dT_{qd0/abc}^{-1}}{dt}=\omega_e\begin{bmatrix}0 & -1 & 0\\ 1 & 0 & 0\\ 0 & 0 & 0\end{bmatrix} \tag{2.1.13}$$

Finally, we have

$$\frac{d\vec{i}_{qd0}}{dt}=\begin{bmatrix}\frac{-r}{L} & \omega_e & 0\\ -\omega_e & \frac{-r}{L} & 0\\ 0 & 0 & \frac{-r}{L}\end{bmatrix}\vec{i}_{qd0}+\frac{1}{L}\vec{v}_{qd0} \tag{2.1.14}$$

2.2 Synchronous machine model

2.2.1 Synchronous generator equivalent circuits

The synchronous machine used in this research is represented in generator mode. After applying Park's transformation and the procedure derived in the last section, we can obtain (2.2.1) to (2.2.6) [40], the equivalent circuit is provided in Figure 2.3[1]. The circuit is expressed in the rotor reference frame and all quantities are viewed from the stator side. Besides, as in the case of generator study, it is usually more convenient to express flux linkages and voltages in terms of reactances instead of inductance (2.2.7-2.2.12) .

[1] Noted that 0-channel is eliminated in a balanced three-phase circuit

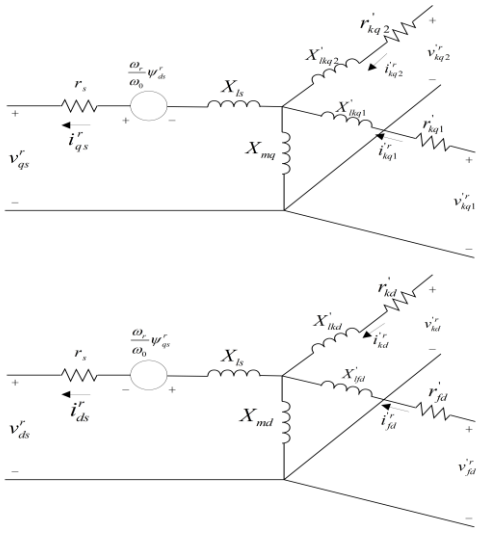

Figure 2.3 Equivalent generator circuits [40]

$$v_{qs}^{r} = -r_s i_{qs}^{r} + \frac{\omega_r}{\omega_0}\psi_{ds}^{r} + \frac{d}{dt}\frac{\psi_{qs}^{r}}{\omega_0} \tag{2.2.1}$$

$$v_{ds}^{r} = -r_s i_{ds}^{r} - \frac{\omega_r}{\omega_0}\psi_{qs}^{r} + \frac{d}{dt}\frac{\psi_{ds}^{r}}{\omega_0} \tag{2.2.2}$$

$$v_{kq1}^{'r} = r_{kq1}^{'} i_{kq1}^{'r} + \frac{d}{dt}\frac{\psi_{kq1}^{'r}}{\omega_0} \tag{2.2.3}$$

$$v_{kq2}^{'r} = r_{kq2}^{'} i_{kq2}^{'r} + \frac{d}{dt}\frac{\psi_{kq2}^{'r}}{\omega_0} \tag{2.2.4}$$

$$v_{kd}^{'r} = r_{kd}^{'} i_{kd}^{'r} + \frac{d}{dt}\frac{\psi_{kd}^{'r}}{\omega_0} \tag{2.2.5}$$

$$v_{fd}^{'r} = r_{fd}^{'} i_{fd}^{'r} + \frac{d}{dt}\frac{\psi_{fd}^{'r}}{\omega_0} \tag{2.2.6}$$

where ω_0 is the nominal electrical angular velocity. The flux linkages are given by

$$\psi_{qs}^{r} = -X_{ls} i_{qs}^{r} + X_{mq}(-i_{qs}^{r} + i_{kq1}^{'r} + i_{kq2}^{'r}) \tag{2.2.7}$$

$$\psi_{ds}^{r} = -X_{ls} i_{ds}^{r} + X_{md}(-i_{ds}^{r} + i_{kd}^{'r} + i_{fd}^{'r}) \tag{2.2.8}$$

$$\psi'^{r}_{kq1} = X'_{lkq1} i'^{r}_{kq1} + X_{mq}(-i^{r}_{qs} + i'^{r}_{kq1} + i'^{r}_{kq2}) \tag{2.2.9}$$

$$\psi'^{r}_{kq2} = X'_{lkq2} i'^{r}_{kq2} + X_{mq}(-i^{r}_{qs} + i'^{r}_{kq1} + i'^{r}_{kq2}) \tag{2.2.10}$$

$$\psi'^{r}_{kd} = X'_{lkd} i^{r}_{kd} + X_{md}(-i^{r}_{ds} + i'^{r}_{kd} + i'^{r}_{fd}) \tag{2.2.11}$$

$$\psi'^{r}_{fd} = X'_{lfd} i^{r}_{fd} + X_{md}(-i^{r}_{ds} + i'^{r}_{kd} + i'^{r}_{fd}) \tag{2.2.12}$$

By substituting (2.2.7–2.2.12) into (2.2.1-2.2.6), we have

$$\begin{bmatrix} v^{r}_{qs} \\ v^{r}_{ds} \\ v'^{r}_{kq1} \\ v'^{r}_{kq2} \\ v'^{r}_{kd} \\ v'^{r}_{fd} \end{bmatrix} = \begin{bmatrix} -r_s - \frac{d}{dt}\frac{X_q}{\omega_0} & -\frac{\omega_r}{\omega_0} X_d & \frac{d}{dt}\frac{X_{mq}}{\omega_0} & \frac{d}{dt}\frac{X_{mq}}{\omega_0} & \frac{\omega_r}{\omega_0} X_{md} & \frac{\omega_r}{\omega_0} X_{md} \\ \frac{\omega_r}{\omega_0} X_q & -r_s - \frac{d}{dt}\frac{X_d}{\omega_0} & -\frac{\omega_r}{\omega_0} X_{mq} & -\frac{\omega_r}{\omega_0} X_{mq} & \frac{d}{dt}\frac{X_{md}}{\omega_0} & \frac{d}{dt}\frac{X_{md}}{\omega_0} \\ \frac{d}{dt}\frac{X_{mq}}{\omega_0} & 0 & r'_{kq1} + \frac{d}{dt}\frac{X'_{kq1}}{\omega_0} & \frac{d}{dt}\frac{X_{mq}}{\omega_0} & 0 & 0 \\ \frac{d}{dt}\frac{X_{mq}}{\omega_0} & 0 & \frac{d}{dt}\frac{X_{mq}}{\omega_0} & r'_{kq2} + \frac{d}{dt}\frac{X'_{kq2}}{\omega_0} & 0 & 0 \\ 0 & -\frac{d}{dt}\frac{X_{md}}{\omega_0} & 0 & 0 & r'_{kd} + \frac{d}{dt}\frac{X'_{kd}}{\omega_0} & \frac{d}{dt}\frac{X_{md}}{\omega_0} \\ 0 & -\frac{d}{dt}\frac{X_{md}}{\omega_0} & 0 & 0 & \frac{d}{dt}\frac{X_{md}}{\omega_0} & r'_{fd} + \frac{d}{dt}\frac{X'_{fd}}{\omega_0} \end{bmatrix} \begin{bmatrix} i^{r}_{qs} \\ i^{r}_{ds} \\ i'^{r}_{kq1} \\ i'^{r}_{kq2} \\ i'^{r}_{kd} \\ i'^{r}_{fd} \end{bmatrix} \tag{2.2.13}$$

where [40]

$$X_q = X_{ls} + X_{mq} \tag{2.2.14}$$

$$X_d = X_{ls} + X_{md} \tag{2.2.15}$$

$$X'_{kq1} = X'_{lkq1} + X_{mq} \tag{2.2.16}$$

$$X'_{kq2} = X'_{lkq2} + X_{mq} \tag{2.2.17}$$

$$X'_{kd} = X'_{lkd} + X_{md} \tag{2.2.18}$$

$$X'_{fd} = X'_{lfd} + X_{md} \tag{2.2.19}$$

Since we only energize field winding, (2.2.27) becomes

$$\begin{bmatrix} v_{qs}^{r} \\ v_{ds}^{r} \\ 0 \\ 0 \\ 0 \\ v_{fd}^{'r} \end{bmatrix} = \begin{bmatrix} -r_s - \frac{d}{dt}\frac{X_q}{\omega_0} & -\frac{\omega_r}{\omega_0}X_d & \frac{d}{dt}\frac{X_{mq}}{\omega_0} & \frac{d}{dt}\frac{X_{mq}}{\omega_0} & \frac{\omega_r}{\omega_0}X_{md} & \frac{\omega_r}{\omega_0}X_{md} \\ \frac{\omega_r}{\omega_0}X_q & -r_s - \frac{d}{dt}\frac{X_d}{\omega_0} & -\frac{\omega_r}{\omega_0}X_{mq} & -\frac{\omega_r}{\omega_0}X_{mq} & \frac{d}{dt}\frac{X_{md}}{\omega_0} & \frac{d}{dt}\frac{X_{md}}{\omega_0} \\ \frac{d}{dt}\frac{X_{mq}}{\omega_0} & 0 & r_{kq1}^{'} + \frac{d}{dt}\frac{X_{kq1}^{'}}{\omega_0} & \frac{d}{dt}\frac{X_{mq}}{\omega_0} & 0 & 0 \\ \frac{d}{dt}\frac{X_{mq}}{\omega_0} & 0 & \frac{d}{dt}\frac{X_{mq}}{\omega_0} & r_{kq2}^{'} + \frac{d}{dt}\frac{X_{kq2}^{'}}{\omega_0} & 0 & 0 \\ 0 & -\frac{d}{dt}\frac{X_{md}}{\omega_0} & 0 & 0 & r_{kd}^{'} + \frac{d}{dt}\frac{X_{kd}^{'}}{\omega_0} & \frac{d}{dt}\frac{X_{md}}{\omega_0} \\ 0 & -\frac{d}{dt}\frac{X_{md}}{\omega_0} & 0 & 0 & \frac{d}{dt}\frac{X_{md}}{\omega_0} & r_{fd}^{'} + \frac{d}{dt}\frac{X_{fd}^{'}}{\omega_0} \end{bmatrix} \begin{bmatrix} i_{qs}^{r} \\ i_{ds}^{r} \\ i_{kq1}^{'r} \\ i_{kq2}^{'r} \\ i_{kd}^{'r} \\ i_{fd}^{'r} \end{bmatrix} \tag{2.2.20}$$

Besides, the electromechanical torque developed by a *p*-pole machine and the equation of motion in generator convention are given as

$$T_e[p.u.] = \psi_{ds}^{r} i_{qs}^{r} - \psi_{qs}^{r} i_{ds}^{r} \tag{2.2.21}$$

$$\frac{2H}{\omega_0}\frac{d\omega_r}{dt} = T_m - T_e \tag{2.2.22}$$

And if interested in rotor angle, it is $\frac{d\theta_r}{dt} = \omega_r - \omega_s$.

Driving synchronous generator in simulation software such as *Matlab/Simulink* can be done by using three-phase stator currents as output and three-phase stator voltages as input. Besides, the field winding voltage which is supplied by the excitation system, as well as the mechanical power supplied by the governor are also inputs to the machine. The stator voltages in (2.2.20) along with other inputs can be used to solve for the windings flux linkages if we formulate the voltages in terms of the flux linkages as the integral equations given below [41]

$$\begin{cases} \psi_{qs}^{r} = \dfrac{1}{s}\omega_0\left\{v_{qs}^{r} - \dfrac{\omega_r}{\omega_0}\psi_{ds}^{r} + \dfrac{r_s}{X_{ls}}\left(\psi_{mq} - \psi_{qs}^{r}\right)\right\} \\ \psi_{ds}^{r} = \dfrac{1}{s}\omega_0\left\{v_{ds}^{r} + \dfrac{\omega_r}{\omega_0}\psi_{qs}^{r} + \dfrac{r_s}{X_{ls}}\left(\psi_{md} - \psi_{ds}^{r}\right)\right\} \\ \psi_{kq1}^{'r} = \dfrac{1}{s}\dfrac{\omega_0 r_{kq1}^{'}}{X_{lkq1}^{'}}\left(\psi_{mq} - \psi_{kq1}^{'r}\right) \\ \psi_{kq2}^{'r} = \dfrac{1}{s}\dfrac{\omega_0 r_{kq2}^{'}}{X_{lkq2}^{'}}\left(\psi_{mq} - \psi_{kq2}^{'r}\right) \\ \psi_{kd}^{'r} = \dfrac{1}{s}\dfrac{\omega_0 r_{kd}^{'}}{X_{lkd}^{'}}\left(\psi_{md} - \psi_{kd}^{'r}\right) \\ \psi_{fd}^{'r} = \dfrac{1}{s}\dfrac{\omega_0 r_{fd}^{'}}{X_{md}}\left\{E_f + \dfrac{X_{md}}{X_{lfd}^{'}}\left(\psi_{md} - \psi_{fd}^{'r}\right)\right\} \end{cases} \tag{2.2.23}$$

where

$$\begin{cases} \psi_{mq} = X_{mq}(-i_{qs}^{r} + i_{kq1}^{'r} + i_{kq2}^{'r}) \\ \psi_{md} = X_{md}(-i_{ds}^{r} + i_{kd}^{'r} + i_{fd}^{'r}) \\ E_f = X_{md}\dfrac{v_{fd}^{'r}}{r_{fd}^{'}} \end{cases} \tag{2.2.24}$$

With (2.2.24), (2.2.7) to (2.2.12) can be rewritten as

$$\begin{cases} \psi_{qs}^{r} = -X_{ls}i_{qs}^{r} + \psi_{mq} \\ \psi_{ds}^{r} = -X_{ls}i_{ds}^{r} + \psi_{md} \\ \psi_{kq1}^{'r} = X_{lkq1}^{'}i_{kq1}^{'r} + \psi_{mq} \\ \psi_{kq2}^{'r} = X_{lkq2}^{'}i_{kq2}^{'r} + \psi_{mq} \\ \psi_{kd}^{'r} = X_{lkd}^{'}i_{kd}^{r} + \psi_{md} \\ \psi_{fd}^{'r} = X_{lfd}^{'}i_{fd}^{r} + \psi_{md} \end{cases} \tag{2.2.25}$$

We can further express the mutual flux linkages as

$$\begin{cases} \psi_{mq} = X_{MQ}\left(\dfrac{\psi_{qs}^{r}}{X_{ls}} + \dfrac{\psi_{kq1}^{'r}}{X_{lkq1}^{'}} + \dfrac{\psi_{kq2}^{'r}}{X_{lkq2}^{'}}\right) \\ \psi_{md} = X_{MD}(\dfrac{\psi_{ds}^{r}}{X_{ls}} + \dfrac{\psi_{kd}^{'r}}{X_{lkd}^{'}} + \dfrac{\psi_{fd}^{'r}}{X_{lfd}^{'}}) \end{cases} \tag{2.2.26}$$

where

$$\begin{cases} \dfrac{1}{X_{MQ}} = \dfrac{1}{X_{ls}} + \dfrac{1}{X_{mq}} + \dfrac{1}{X'_{lkq1}} + \dfrac{1}{X'_{lkq2}} \\ \dfrac{1}{X_{MD}} = \dfrac{1}{X_{ls}} + \dfrac{1}{X_{md}} + \dfrac{1}{X'_{lkd}} + \dfrac{1}{X'_{lfd}} \end{cases} \tag{2.2.27}$$

Having (2.2.25) to (2.2.27) we can derive the winding currents as

$$\begin{cases} i_{qs}^{r} = \dfrac{\psi_{mq} - \psi_{qs}^{r}}{X_{ls}} \\ i_{ds}^{r} = \dfrac{\psi_{md} - \psi_{ds}^{r}}{X_{ls}} \\ i_{kq1}^{'r} = \dfrac{\psi_{kq1}^{'r} - \psi_{mq}}{X'_{lkq1}} \\ i_{kq2}^{'r} = \dfrac{\psi_{kq2}^{'r} - \psi_{mq}}{X'_{lkq2}} \\ i_{kd}^{r} = \dfrac{\psi_{kd}^{'r} - \psi_{md}}{X'_{lkd}} \\ i_{fd}^{r} = \dfrac{\psi_{fd}^{'r} - \psi_{md}}{X'_{lfd}} \end{cases} \tag{2.2.28}$$

The terminal variables can be calculated by

$$\begin{cases} V_t = \sqrt{\left(v_{ds}^{r}\right)^2 + \left(v_{qs}^{r}\right)^2} \\ I_t = \sqrt{\left(i_{ds}^{r}\right)^2 + \left(i_{qs}^{r}\right)^2} \\ P_e = v_{ds}^{r} i_{ds}^{r} + v_{qs}^{r} i_{qs}^{r} \\ Q_e = v_{qs}^{r} i_{ds}^{r} - v_{ds}^{r} i_{qs}^{r} \end{cases} \tag{2.2.29}$$

Using (2.2.21) to (2.2.29) we are now ready to simulate the synchronous generator in *Simulink*, see Fig.2.4-2.7[41]. Examining the introduced generator in Kundur two-area system with a line fault occurred in the double transmission line between the two areas, we can evaluate the generator transient response given in Figure 2.8. According to the transient response, we can find that the two q-axis damper windings and the d-axis damper windings present very fast transient

during the simulation which does not have an obvious effect on the generator itself neither the network. In other words, these windings can be eliminated in the transient study.

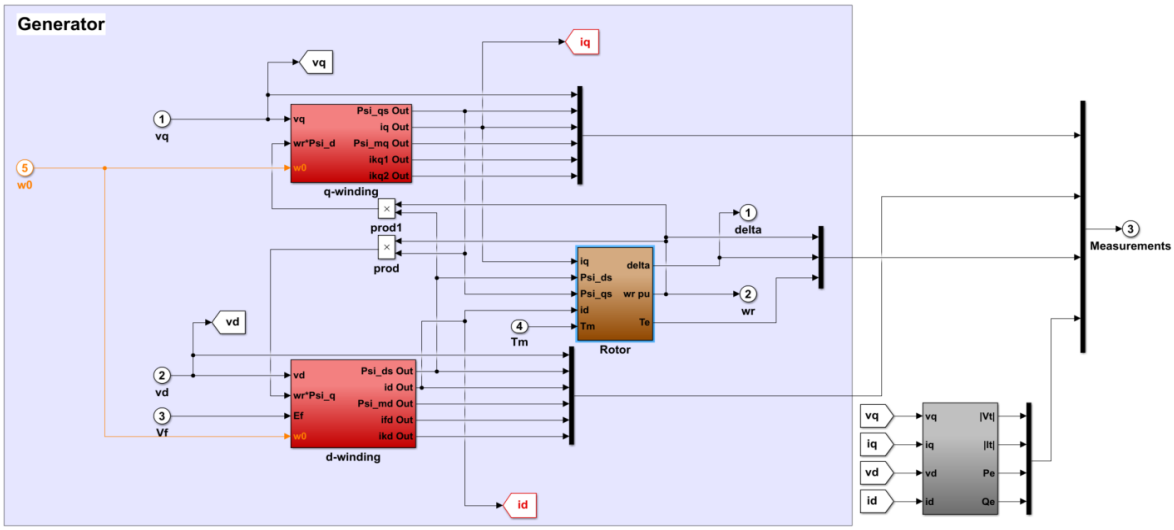

Figure 2.4 Simulink model structure

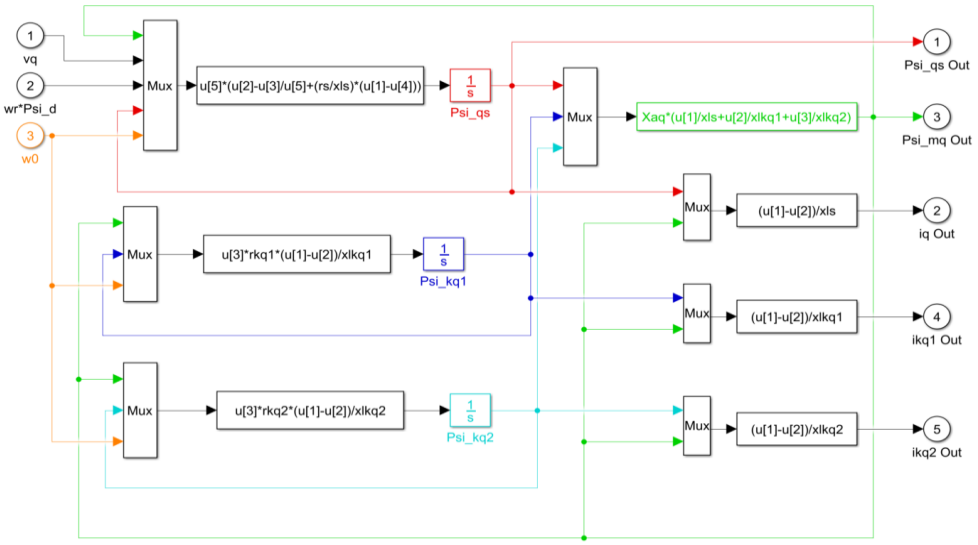

Figure 2.5 Simulink model inside q-winding block

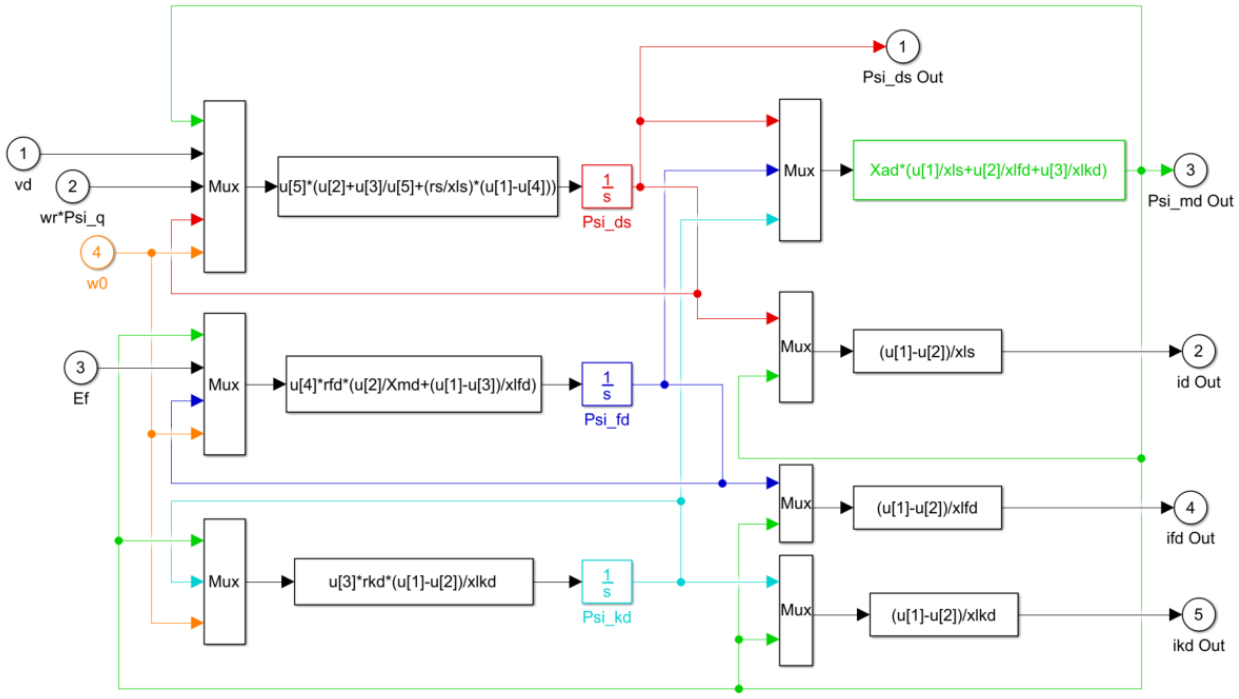

Figure 2.6 Simulink model inside d-winding block

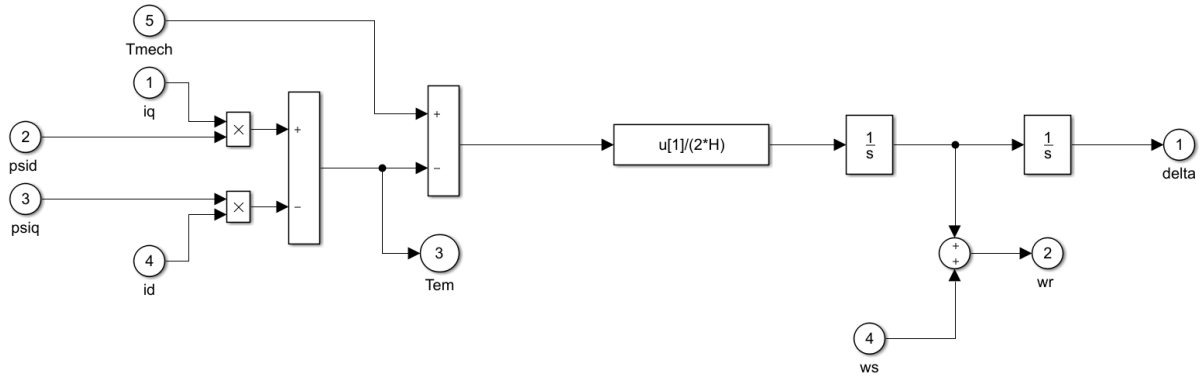

Figure 2.7 Simulink model inside rotor block

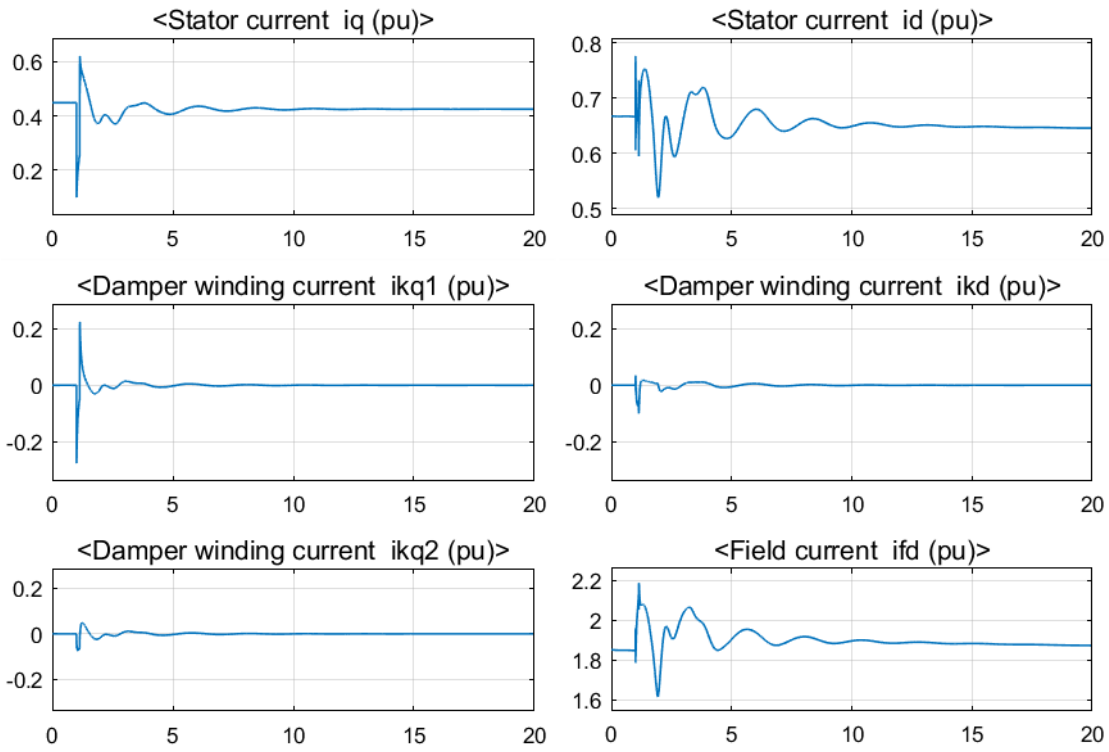

Figure 2.8 Simulation results of dq-winding currents

2.2.2 Simplified decommissioned generator model for transient study

The classical generator model is widely used in transient stability study. With a set of assumptions such as ignoring the fast damper windings and etc., the machine model can be represented by a constant voltage source behind transient reactance $r_s + jX_s$ [42] [The yellow book] as shown in Figure 2.9. With q-axis of the rotating frame aligned with the terminal voltage, the machine model can be written as below. However, since this decommissioned generator is used as an energy storage device, the governor system is removed while the excitation system remains to provide the constant internal voltage. Therefore, the equation of motion (2.2.32) is replaced by (2.2.33).

$$\frac{X_s}{\omega_r}\frac{di_{sd}}{dt} = X_s i_{sq} - r_s i_{sd} - v_{sd} \tag{2.2.30}$$

$$\frac{X_s}{\omega_r}\frac{di_{sq}}{dt} = -X_s i_{sd} - r_s i_{sq} - v_{sq} + E_q \tag{2.2.31}$$

$$\frac{2H}{\omega_0}\frac{d\omega_r}{dt} = T_m - T_e = P_m - P_e \tag{2.2.32}$$

$$\frac{2H}{\omega_0}\frac{d\omega_r}{dt} = -P_e \tag{2.2.33}$$

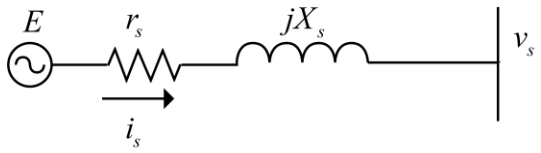

Figure 2.9 Classical synchronous machine one-line diagram

2.3 Back-to-back converter model

The DSMS system proposed in this work is interfaced with the grid via back-to-back converter which is inspired by the voltage sourced converter HVDC (VSC-HVDC) model [18], [43]. The converter structure is given in Figure 2.10.

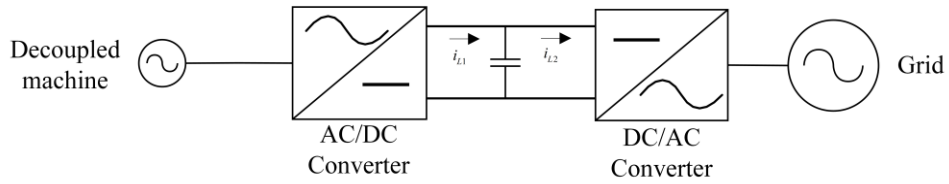

Figure 2.10 Back-to-back converter structure

Using the transformation given in section 2.1, with *q*-axis aligned with AC-side voltage, the differential equations of the grid-side converter and the DC-link can be expressed as

$$\frac{X_g}{\omega_g}\frac{di_{gd}}{dt} = X_g i_{gq} - r_g i_{gd} - v_{cd} \tag{2.3.1}$$

$$\frac{X_g}{\omega_g}\frac{di_{gq}}{dt} = -X_g i_{gd} - r_g i_{gq} - v_{cq} + V_{gq} \tag{2.3.2}$$

$$\frac{dv_{dc}}{dt} = \frac{1}{C_{dc}}\left(i_{L1} - i_{L2}\right) \tag{2.3.3}$$

where i_{gd} and i_{gq} are the *dq*-axis currents of the grid-side converter. $r_g + jX_g$ is the grid-side converter phase reactor. v_{cd} and v_{cq} are the *dq*-axis voltages of grid-side converter. ω_g is the grid frequency in radians per second [rad/s]. V_{gq} is the q-axis grid voltage. The DC circuit is modeled by the equivalent DC capacitance C_{dc}, the DC-link voltage v_{dc}, the machine-side line current i_{L1} and the grid-side line current i_{L2}.

2.4 Decoupled synchronous machine system model

As shown in Figure 2.11, the DSMS contains the retired synchronous machine without governor and the AC-DC-AC converter. Equations (2.2.30), (2.2.31), (2.2.33), (2.3.1-2.3.3) together comprise the model of the proposed system

$$\begin{cases} \dfrac{X_s}{\omega_r}\dfrac{di_{sd}}{dt} = X_s i_{sq} - r_s i_{sd} - v_{sd} \\ \dfrac{X_s}{\omega_r}\dfrac{di_{sq}}{dt} = -X_s i_{sd} - r_s i_{sq} - v_{sq} + E_q \\ \dfrac{2H}{\omega_0}\dfrac{d\omega_r}{dt} = -P_e \\ \dfrac{X_g}{\omega_g}\dfrac{di_{gd}}{dt} = X_g i_{gq} - r_g i_{gd} - v_{cd} \\ \dfrac{X_g}{\omega_g}\dfrac{di_{gq}}{dt} = -X_g i_{gd} - r_g i_{gq} - v_{cq} + V_{gq} \\ \dfrac{dv_{dc}}{dt} = \dfrac{1}{C_{dc}}\left(i_{L1} - i_{L2}\right) \end{cases} \tag{2.4.1}$$

It is worth mentioning that E_q is not constant during the active power adjustment. The fundamental operating principle of generators and electrical drives is Faraday's Law of Induction. It describes how the magnetic field will interact with an electric circuit to produce an electromotive force (EMF). According to Faraday's law, EMF in the field winding $\mathbf{e}_{fd}$ is produced by the rate of change of its magnetic flux [44]

$$\mathbf{e}_{fd} = \frac{d\Phi_{fd}}{dt} = \frac{dL_{fd} i_{fd}}{dt} \tag{2.4.2}$$

whose RMS amplitude satisfies the following relationship when the inductance remains the same

$$E_{fd} \propto \omega_r I_{fd} \tag{2.4.3}$$

As mentioned earlier, the voltage supply of the field winding keeps the same which leads to the constant I_{fd}. Therefore, the internal voltage E_q will follow the pattern of rotor speed in this work.

Chapter 3 Decoupled Synchronous Machine System Controller Design

3.1 Decoupled decommissioned synchronous machine controller

The proposed decoupled generator with no governor system but the constant field winding voltage is essentially equivalent to the permanent-magnet AC machine (PMAM) configuration. Therefore, it can be controlled in the similar way that the PMAM is controlled. This remaining of this section will illustrate the control mechanism of PMAM.

As mentioned earlier, the machine is connected to AC/DC converter which transforms either the power from the rotating mass to the DC-link, or converts the electrical power from DC-link to mechanical energy to drive the rotating mass. According to command such as the electrical power, the controller will solve for the gate switching signals to the semiconductors of the converter, see Figure 3.1.

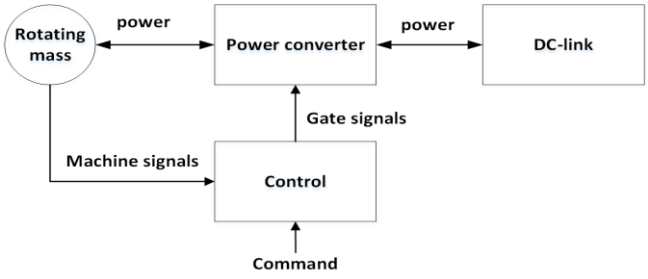

Figure 3.1 Rotating mass control structure

The power transmission is regulated through the adjustment of stator currents. One important feature of the current-regulated converters is the robustness with respect to machine parameter

change such as stator leakage inductance [40]. Besides, the stator currents are restricted due to the corresponding command which can prevent damage to the power electronics devices in the event of machine starting-up as well as the winding-to-winding short circuit [40]. The control mechanism is given in Figure 3.2. In a word, the inner-loop current commands are generated by the outer power control loop. The current commands are then used to generate the duty cycles (gate signals) to converter.

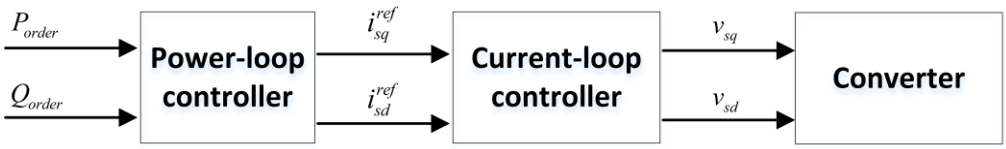

Figure 3.2 Machine-side control scheme[1]

At the meantime, grid-side converter is responsible for maintaining DC-link voltage while providing reactive power to the grid.

3.1.1 Current controller design

Now, we begin with the controller design of the inner current loop. The purpose of current loop is to produce the proper converter voltage command which can be scaled to duty cycles. There are several ways to achieve the inner loop control design. According to [40], by using the classical PI controller, the converter voltage reference can be assumed to be

$$v_{sq}^{ref} = -X_s i_{sd} + E_q + (K_{P,is} + K_{I,is}/s)(i_{sq}^{ref} - i_{sq}) \tag{3.1.1}$$

$$v_{sd}^{ref} = -X_s i_{sq} + (K_{P,is} + K_{I,is}/s)(i_{sd}^{ref} - i_{sd}) \tag{3.1.2}$$

where K_{Pis} and K_{Iis} are the proportional and integral terms of PI controller respectively. s is the Laplace operator. Assume the *qd*-axis converter voltage reference are equal to the actual ones i.e. let (3.1.1) and (3.1.2) equals to (2.2.30) and (2.2.31) respectively, we have

[1]Reactive power reference is set to zero since the DC-link only allows real power goes through.

$$
\begin{aligned}
& v_{sq}^{ref} = v_{sq} \\
& \rightarrow -X_s i_{sd} + E_q + (K_{P,is} + K_{I,is}/s)(i_{sq}^{ref} - i_{sq}) = -X_s i_{sd} - r_s i_{sq} + E_q - \frac{X_s}{\omega_r} s i_{sq} \\
& \rightarrow (K_{P,is} + K_{I,is}/s)(i_{sq}^{ref} - i_{sq}) = -r_s i_{sq} - \frac{X_s}{\omega_r} s i_{sq} \\
& \rightarrow \frac{i_{sq}}{i_{sq}^{ref}} = \frac{\frac{\omega_r}{X_s} K_{P,is}\left(s + \frac{K_{I,is}}{K_{P,is}}\right)}{s^2 + s\left(K_{P,is} - r_s\right)\frac{\omega_r}{X_s} + K_{I,is}\frac{\omega_r}{X_s}}
\end{aligned}
\tag{3.1.3}
$$

The *d*-channel current close loop transfer function is the same as the *q*-channel. The scheme of current loop is given in Figure 3.3. As can be seen, the system is obviously coupled. Two extra terms in the forward path are used to decouple the two channels

$$
\begin{cases} X_s i_{sq} \\ -X_s i_{sd} \end{cases}
\tag{3.1.4}
$$

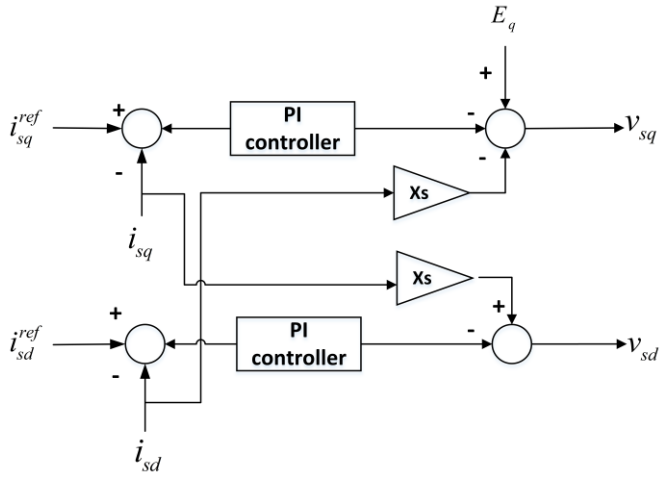

Figure 3.3 Inner current-loop control scheme

A case study of this quasi-PMAM machine during different active power commands is informative. The parameters of a high-speed steam turbine generator are given in Table 3-1 (winding parameters are given in per unit) [40].

Table 3-1 Steam turbine generator parameters

Rating	$\text{Voltage}_{\text{L-L}}$	Power factor	Poles	Speed	Inertia
835MW	26kV	0.85	2	3600 r/min	H=5.6seconds
$r_s + jX_{ls}$	$X_q = X_d$	$r'_{kq1} + jX'_{lkq1}$	$r'_{kq2} + jX'_{lkq2}$	$r'_{kd} + jX'_{lkd}$	$r'_{fd} + jX'_{lfd}$
0.003+0.j19	1.8	0.00178+j0.8125	0.00841+j0.0939	0.01334+j0.08125	0.000929+j0.1414

Let us first derive the transient reactance of the generator listed in Table 3-1 by following the formula given in [45]

$$\begin{aligned} X'_d &= X_{ls} + \frac{1}{\frac{1}{X_{md}} + \frac{1}{X'_{lfd}}} \\ &= X_{ls} + \frac{X_{md} X'_{lfd}}{X_{md} + X'_{lfd}} \end{aligned} \tag{3.1.5}$$

We can derive X_{md} from

$$\begin{aligned} X_d &= X_{ls} + X_{md} \\ \rightarrow X_{md} &= X_d - X_{ls} \end{aligned} \tag{3.1.6}$$

Substituting the parameters in Table 3-1 into (3.1.5) we have

$$X'_d = X_{ls} + \frac{X_{md} X'_{lfd}}{X_{md} + X'_{lfd}} = 0.19 + \frac{1.61 \times 0.1414}{1.61 + 0.1414} = 0.32 \; p.u. \tag{3.1.7}$$

where $X_{md} = 1.8 - 0.19 = 1.61 \; p.u.$ Substituting $X_s = X'_d = 0.32$, $r_s = 0.003$, $\omega_r = 2\pi 60$ and the pole locations of $s_1 = -10$ and $s_2 = -1000$ into (3.1.3) yields

$$\begin{cases} K_{I,is} = 8.4883 \\ K_{P,is} = 0.8603 \end{cases} \tag{3.1.8}$$[1]

[1] The *d*-channel PI controller parameters are the same as *q*-channel

Figure 3.3 showcases the resultant current step responses as the *qd* current commands step from zero to 0.2 and 0.1 respectively. It can be seen that the machine performs extremely well.

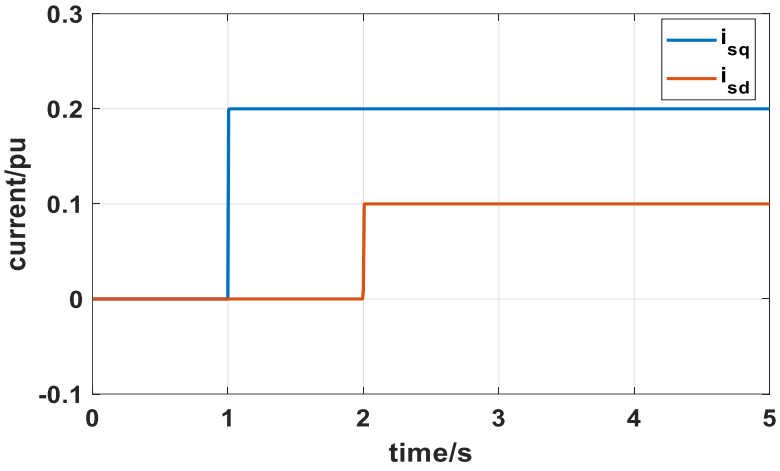

Figure 3.4 Generator current step responses with user-defined pole locations

Here comes another problem which is the pole locations selection. According to [18], the open loop transfer function is

$$G_{is} = \frac{K_{P,is}\left(s + K_{I,is} \middle/ K_{P,is}\right)}{s\frac{X_s}{\omega_r}\left(s + r_s\frac{\omega_r}{X_s}\right)} \tag{3.1.9}$$

The second-order transfer function can be transformed into first-order transfer function by cancelling the pole of (3.1.9) with the following specific zero

$$s = -\frac{K_{I,is}}{K_{P,is}} = -r_s\frac{\omega_r}{X_s} \tag{3.1.10}$$

As a result, the closed loop transfer function becomes

$$\frac{i_{sq}}{i_{sq}^{ref}} = \frac{1}{\tau_{is}s + 1} \tag{3.1.11}$$

where

$$\tau_{is} = \frac{X_s}{\omega_r K_{P,is}} \tag{3.1.12}$$

Therefore, the PI controller parameters can be derived as

$$\begin{cases} K_{P,is} = \dfrac{X_s}{\omega_r \tau_{is}} \\ K_{I,is} = \dfrac{r_s}{\tau_{is}} \end{cases} \tag{3.1.13}$$

Note that the rise time constant τ_{is} is a user-defined parameter. It is worth noting that the parameter should be adequately small such that the fast response of inner current loop can be guaranteed. In this work, τ_{is} is set to 1 ms to ensure fast and good inner loop response. The PI controller parameters are given in (3.1.14). As can be seen clearly in Figure 3.4, *qd*-axis currents reach their references 0.3 and -0.1 as fast as expected.

$$\begin{cases} K_{P,is} = 0.8488 \\ K_{I,is} = 3 \end{cases} \tag{3.1.14}$$

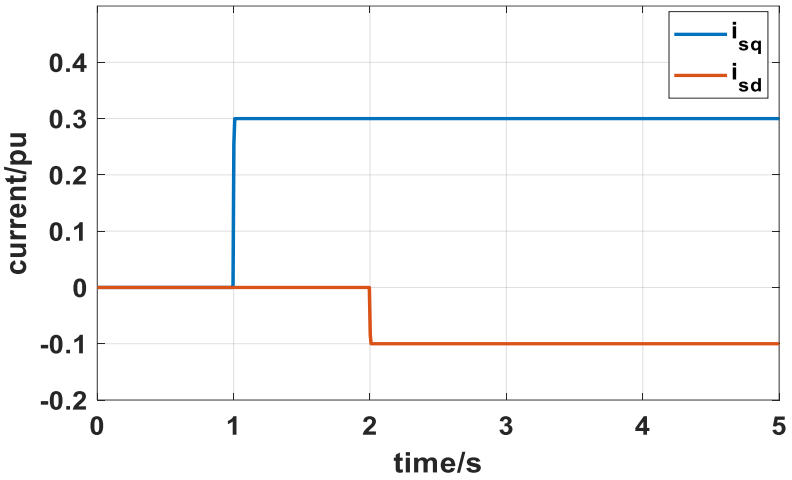

Figure 3.5 Generator current step responses with user-defined rise time

3.1.2 Power controller design

Next, we need to design the outer power loop controller as indicated in Figure 3.2. Recall the power expression in *qd*-frame

$$\begin{cases} P_e = v_{ds}^r i_{ds}^r + v_{qs}^r i_{qs}^r \\ Q_e = v_{qs}^r i_{ds}^r - v_{ds}^r i_{qs}^r \end{cases} \tag{3.1.15}$$

which can be written as (3.1.16) with *q*-axis aligned with AC-side voltage (*d*-axis voltage equals to zero).

$$\begin{cases} P_e = v_{ds}^r i_{ds}^r \\ Q_e = v_{qs}^r i_{ds}^r \end{cases} \tag{3.1.16}$$

As a result, active and reactive powers can be regulated independently by providing the corresponding current commands. These commands are the references for the inner current loop as shown in Figure 3.5. The active power loop shows a second-order dynamic [46] which can be formulated in this standard form

$$\frac{P_e}{P_e^{ref}} = \frac{\frac{1}{\alpha\zeta\omega_n}s+1}{\left(\frac{s}{\omega_n}\right)^2 + 2\frac{\zeta}{\omega_n}s+1} \tag{3.1.17}$$

where α is a scaling factor of the zero, ζ is the damping ratio and ω_n is the natural frequency. After solving the close loop transfer function of active power, we have (see derivation details in [18], [46])

$$\begin{cases} \alpha = \dfrac{2K_{I,P_e}\tau_{is}}{\left(K_{P,P_e}E_q+1\right)K_{P,P_e}} \\ \omega_n^2 = \dfrac{E_q K_{I,P_e}}{\tau_{is}} \\ \zeta = \dfrac{E_q K_{P,P_e}+1}{2\omega_n\tau_{is}} \end{cases} \tag{3.1.18}$$

where K_{P,P_e} and K_{I,P_e} are the active power loop PI-controller parameters.

The damping ratio and natural frequency are calculated by the pre-defined peak time T_p and the maximum overshoot M_p of the standard second-order responses [47]

$$M_p = e^{-\frac{\pi\zeta}{\sqrt{1-\zeta^2}}} \qquad \Rightarrow \qquad \zeta = -\ln\left(M_p\right)\frac{1}{\sqrt{\ln\left(M_p\right)^2+\pi^2}} \tag{3.1.19}$$

$$T_p = \frac{\pi}{\omega_n \sqrt{1-\zeta^2}} \quad \Rightarrow \quad \omega_n = \frac{\pi}{T_p \sqrt{1-\zeta^2}} \tag{3.1.20}$$

From (3.1.18) to (3.1.20), we can derive the PI-controller parameters as following

$$\begin{cases} K_{P,P_e} = \dfrac{2\zeta\omega_n\tau_{is} - 1}{E_q} \\ K_{I,P_e} = \dfrac{\omega_n^2 \tau_{is}}{E_q} \end{cases} \tag{3.1.21}$$

Choosing $M_p = 0.15$ and $T_p = 3\tau_{is}$, with the method described above, the parameters for the active power controller are calculated as

$$\begin{cases} K_{P,P_e} = 0.1030 \\ K_{I,P_e} = 1346.6 \end{cases} \tag{3.1.22}$$

Figure 3.6-3.8 shows the active power, rotor speed and the current responses. It can be seen that the active power reaches its commands very fast with about 0.15 overshoot which is acceptable. The rotating mass slows down when it is required to provide power while it speeds out to absorb power from the grid. In addition, Figure 3.7 proves that E_q is proportional to rotor speed leading to the same dynamical pattern. Again, the inner current loops implement the commands precisely as shown in Figure 3.8.

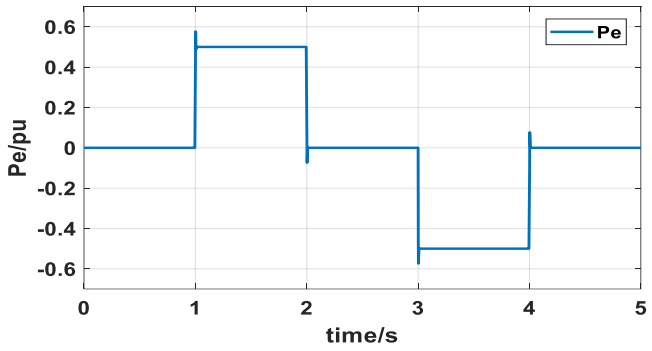

Figure 3.6 Active power response

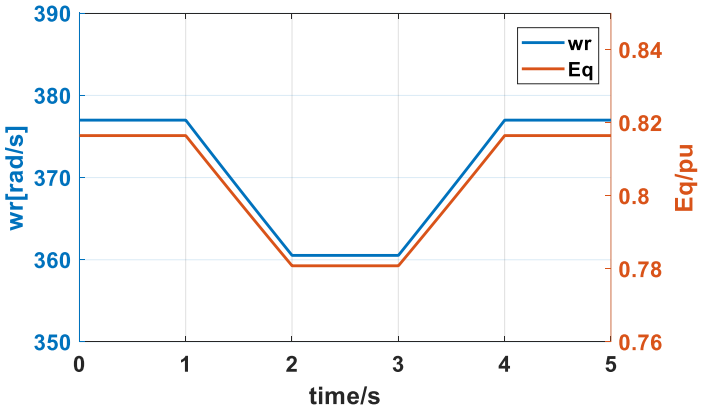

Figure 3.7 Rotor speed and field winding voltage responses

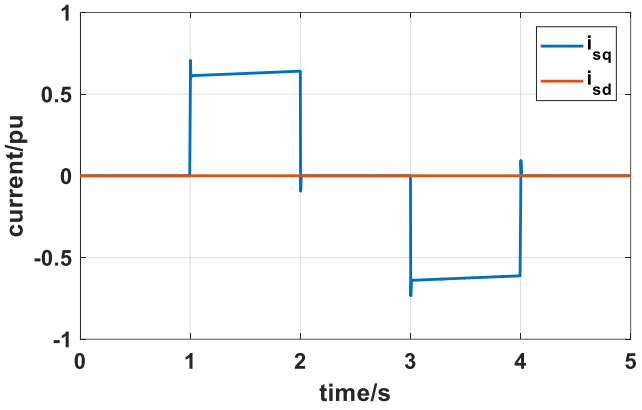

Figure 3.8 Stator dq-current responses

3.2 Grid-side converter controller

Recall the grid-side converter model and the DC-link model

$$\begin{cases} \dfrac{X_g}{\omega_g}\dfrac{di_{gd}}{dt} = X_g i_{gq} - r_g i_{gd} - v_{cd} \\ \dfrac{X_g}{\omega_g}\dfrac{di_{gq}}{dt} = -X_g i_{gd} - r_g i_{gq} - v_{cq} + V_{gq} \\ \dfrac{dv_{dc}}{dt} = \dfrac{1}{C_{dc}}\left(i_{L1} - i_{L2}\right) \end{cases} \tag{3.2.1}$$

Follow the same procedure of the current loop controller design in section 3.1.1 we can obtain

$$\frac{i_{gq}}{i_{gq}^{ref}} = \frac{\frac{\omega_g}{X_g} K_{P,ig} \left(s + \frac{K_{I,ig}}{K_{P,ig}} \right)}{s^2 + s\left(K_{P,ig} - r_g \right) \frac{\omega_g}{X_g} + K_{I,ig} \frac{\omega_g}{X_g}} \tag{3.2.2}$$

Similarly, this second-order transfer function can be turned in to first-order transfer function by setting the zero as

$$s = -\frac{K_{I,ig}}{K_{P,ig}} = -r_g \frac{\omega_g}{X_g} \tag{3.2.3}$$

which leads to

$$\frac{i_{gq}}{i_{gq}^{ref}} = \frac{1}{\tau_{ig} s + 1} \tag{3.2.4}$$

and its corresponding PI-controller parameters

$$\begin{cases} K_{P,ig} = \dfrac{X_g}{\omega_g \tau_{ig}} \\ K_{I,ig} = \dfrac{r_g}{\tau_{ig}} \end{cases} \tag{3.2.5}$$

Based on the power rating of the machine, the parameters of the grid-side converter and DC-link can be chosen as in Table 3-2 [18]. Choosing the same rise time constant as the machine-converter τ_{ig} =1 ms the PI-controller parameters can be calculated as

$$\begin{cases} K_{P,ig} = 0.4393 \\ K_{I,ig} = 1 \end{cases} \tag{3.2.6}$$

Table 3-2 Grid-side converter parameters

Power rating	Voltage base	r_g	X_g	C_{dc}	V_{dc}
1000 MW	26kV	0.001	0.1656	0.004	7.5

The DC voltage controller parameters are firstly tuned with the similar approach as the power loop in last section (see details in [46]) then manually tuned to obtain a more satisfying response. The reactive power loop is tuned heuristically using PI tuning tool in *Matlab*. Table 3-3 shows the tuning results.

Table 3-3 PI-controller parameters of DC-link voltage and reactive power

$K_{P,v}$	$K_{I,v}$	$K_{P,Q}$	$K_{I,Q}$
-4.2	-25.6	0.4	1169.2

Figure 3.9 and 3.10 show the DC voltage and reactive power responses with 7.6 pu and 0.3 pu commands respectively. DC voltage response has a 0.021 overshoot while reactive power has 0.067 overshoot. They are all acceptable.

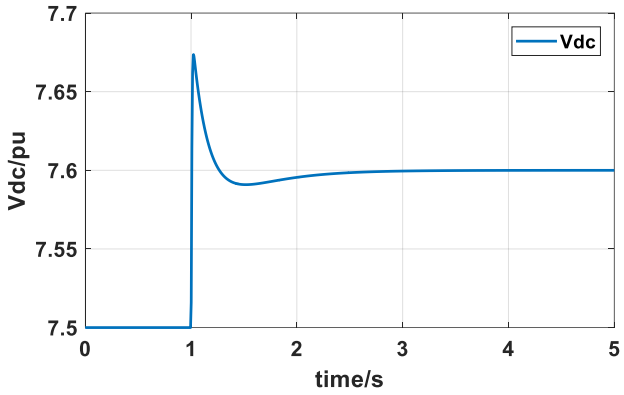

Figure 3.9 DC-link voltage responses

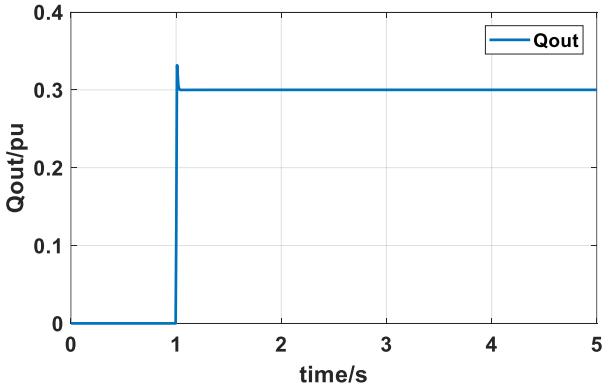

Figure 3.10 Reactive power response

3.3 Overall performance of the system

In this study, the machine is connected to infinite bus whose characteristics such as voltage and frequency do not change in spite of the power delivered or absorbed by the machine. The infinite bus may not be practical in real life scenario, however, looking out from point where the machine is connected to, the size of the rest of the power system is much larger than the machine itself regarding to the power ratings. That is to say, the characteristics of the infinite bus should be sufficiently approached to reality. It can be seen from Figure 3.11 to 3.13 that the system follows its command very well. Different loops are able to implement their commands individually in a fast and satisfying manner.

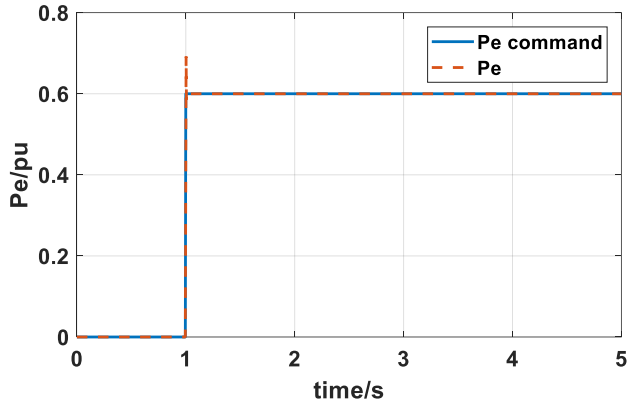

Figure 3.11 Active power response

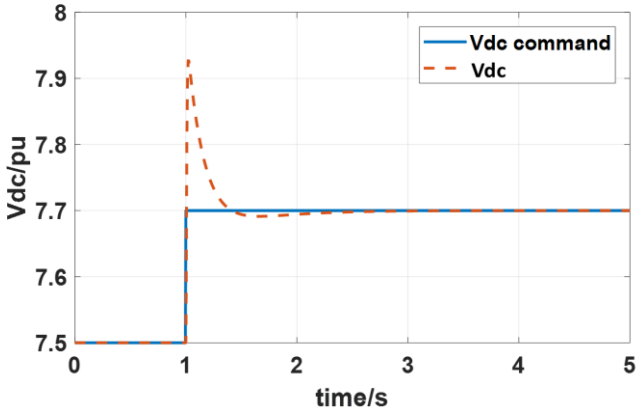

Figure 3.12 DC-link voltage & reactive power responses

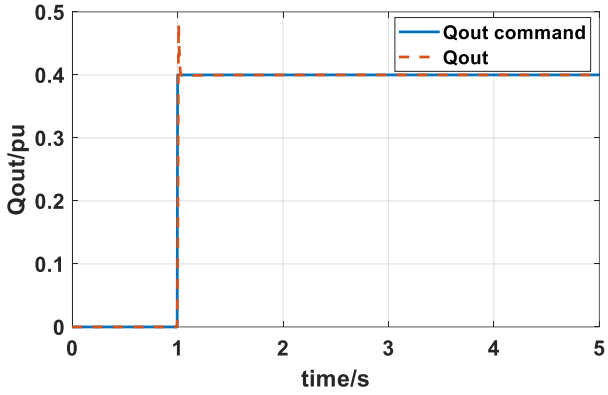

Figure 3.13 Reactive power response

Chapter 4 Koopman Operator Theory

In the previous chapters, the controller design methodology of DSMS has been introduced. The main goal of the proposed system is to eliminate frequency oscillation and improve voltage profile by varying active power output, the variation of DC-link voltage and reactive powers as Figure 4.1 indicates. Note that the active power and DC-link voltage are used to damp frequency oscillation while the reactive power is used to improve the voltage transient performance[1]. Now the task is to design the external controllers which produces those reference signals. The external controllers consist of the frequency controller and voltage controller respectively. Conventionally, in order to design a controller to enhance system stability during the disturbances caused by physical events[2], we need to derive the system equations and linearize them around the equilibrium points. However, an explicit dynamical model shown in the black box including the external power grid is of the great challenge due to the uncertain characteristics of the converter-interfaced generation. This makes the data-driven control the only practical option. The Koopman operator theory is a popular and powerful tool which is capable of the analysis and prediction of the nonlinear dynamical system using measurement data [25] making it a data driven approach. The Koopman operator utilizes a set of scalable

[1] The DC-link voltage is used as an auxiliary functionality for frequency control as given in [48].

[2] The physical events applied are essentially different perturbations (we also call them disturbances) in power system. Those perturbations are different from exogenous inputs. They are equivalent to the change of the system structure, parameters, or operating conditions.

observable functions to reconstruct the underlying dynamical system from measurement data in a linear but high-dimension space i.e. the system is linear in this new space, see an example shown in Figure 4.2. In order to understand Koopman operator theory, we will start with the basic concepts and geometric properties of nonlinear dynamical systems.

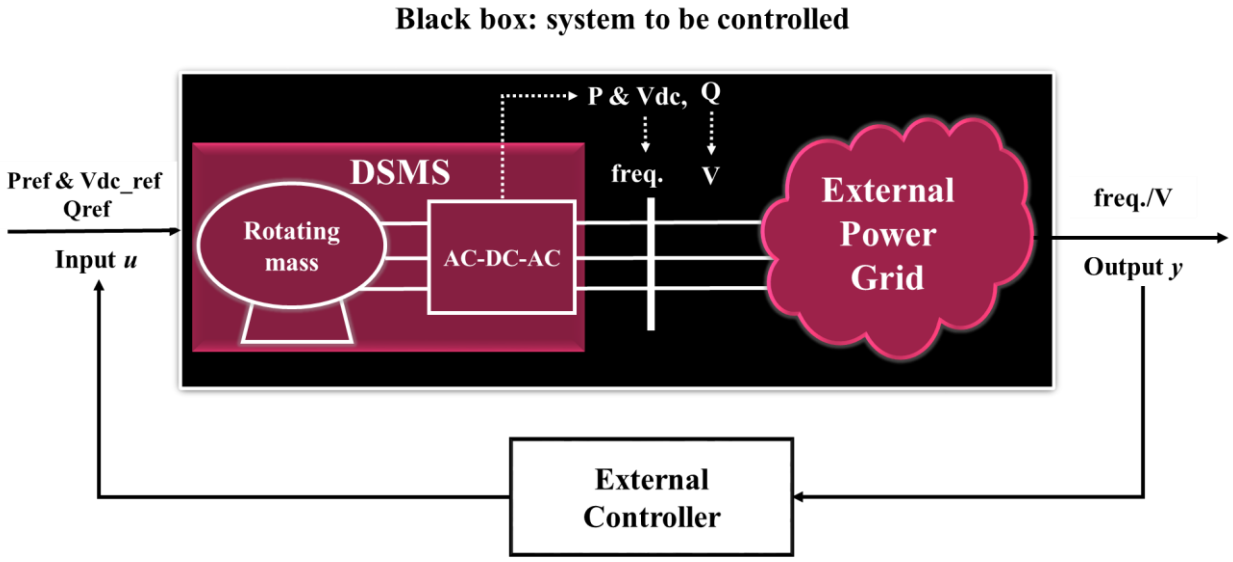

Figure 4.1 General system structure

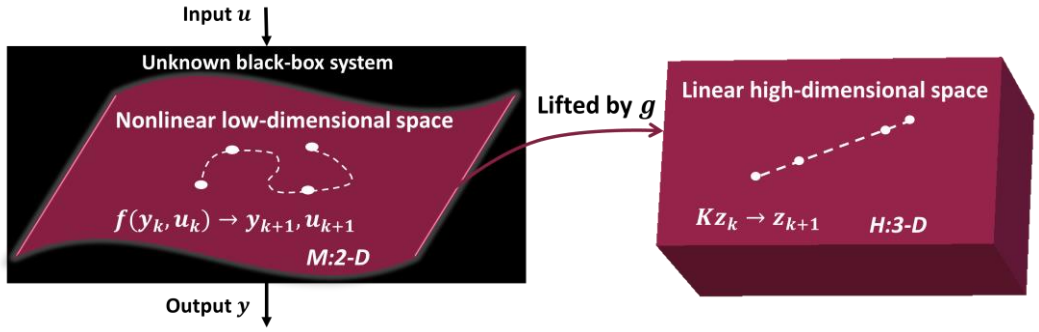

Figure 4.2 Koopman operator theory schematic diagram

4.1 Nonlinear dynamical systems

4.1.1 The nonlinear dynamical viewpoint of systems

Dynamical systems are the systems that evolve and change in time. The systems either settle down to their equilibrium points, repeat periodically, or behave in more sophisticated way. Let us consider this differential equation

$$a\frac{d^2x}{dt^2}+b\frac{dx}{dt}+cx=0 \tag{4.1.1}$$

which can be written in another form by introducing new variables $x_1 = x$, $x_2 = \dot{x}$

$$\begin{aligned}\dot{x}_1 &= x_2\\ \dot{x}_2 &= -\frac{1}{a}\left(b\dot{x}_1 + cx_1\right)\end{aligned} \tag{4.1.2}$$

For the system with *n* variables we have (4.1.3). This is referred to as *n*-dimensional system with *n* states x_i . It has an *n*-dimensional phase space.

$$\begin{aligned}\dot{x}_1 &= f_1(x_1,...,x_n)\\ &\vdots\\ \dot{x}_n &= f_n(x_1,...,x_n)\end{aligned} \tag{4.1.3}$$

Since all the variables are of the first-order, (4.1.3) provides a linear system. If the equations contain other terms of x_i such as products $x_i x_j$, function $f(x_i)$, higher order x_i^4 and etc., then the system is nonlinear. For example, the motor of rotor differential equation

$$2H\frac{d^2\theta_r}{dt^2} = P_M - \frac{E_q V_t \sin\left(\theta_r - \theta_{V_t}\right)}{X_s} \tag{4.1.4}$$

where θ_{V_t} is the terminal bus radian angle, V_t is terminal bus voltage, θ_r is rotor radian angle, E_q is internal voltage, X_s is the generator equivalent reactance, P_M is mechanical power. The windage friction is neglected here. Nonlinear system is difficult to solve analytically. The most commonly way is to linearize the nonlinear system around its equilibrium point with small disturbance such as $\sin\theta_r = \theta_r$ for $\theta_r \ll 1$. However, this leads to another problem: the large disturbance will not be caught up.

[49] illustrates an idea to solve the nonlinear system using geometric methods. The aim is to extract information from the system trajectories in its phase space. Trajectory is defined as the path that an object moves or changes as a function of time starting from an initial condition. For instance, Figure 4.3 shows $\theta_r - \omega_r$ curve which is the transient trajectory of generator No.3 in the Kundur two-area system starting from $\left[\theta_r(0), \omega_r(0)\right]$. The coordinates $\left[\theta_r(k), \omega_r(k)\right]$ at different

time stamp $k = 1, ..., t$ are the solution of this nonlinear system. The corresponding space of (θ_r, ω_r) is the **phase space** of the system.

In general, we want to solve the *n*-dimensional system (4.1.3) using its trajectories in the *n*th-order phase space without analytical solutions. Therefore, obtaining the correct dimension of the system will be the first task. This will be discussed in Chapter 5. In most cases, the systems not only depend on the states but also depend on inputs u_m. To take the effects of inputs into account, we can expend the system dimension by adding the space of u_m. By doing that, under the controlled setting, it allows us to visualize the phase space with the trajectories which also contain functions depending on input.

The reason why the linear systems can be solved analytically is that linear systems can be decomposed into pieces using various methods such as Fourier transformation, Laplace transformation while nonlinear system cannot. However, our daily life does not work in such a simple linear way. For instance, optics subjects and power system operations behave in the nonlinear way since their components or elements are interfered and correlated with each other [50]–[53]. The rest of this chapter will start with the basis of nonlinear system then transient to the notable Koopman theory.

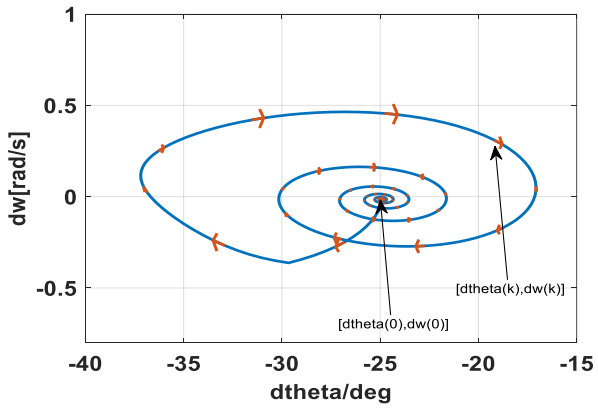

Figure 4.3 Trajectory and phase space of generator No.3

4.1.2 Basic geometric concepts

- Equilibrium of system: Fixed points [49]

Consider a vector field in a continuous time system

$$\dot{x} = f\left(x\right) \tag{4.1.5}$$

where $x \in \mathbb{R}^n$ is the vector of states and $f : \mathcal{M} \to \mathbb{R}^n$ is the vector field on the state space.

Let us define a flow map $F : \mathcal{M} \to \mathcal{M}$

$$F^t(x_{t_0}) = x_{t_0+t} = x_{t_0} + \int_{t_0}^{t_0+t} f(x(\tau))d\tau \tag{4.1.6}$$

which can maps the current state x_{t_0} to the future state x_{t_0+t} at time *t* with the assumption that solution of (4.1.5) exists[1]. This induces the discrete-time system

$$x_{k+1} = T(x_k) \tag{4.1.7}$$

where the sequence $\left[x_0, x_1, \ldots\right]$ is called the orbit starting from x_0 and $T : \mathcal{M} \to \mathcal{M}$ is the dynamic map.

The **fixed point** of this system is the solution which does not vary in time. In other word, the fixed point is the equilibrium solution $\bar{x}$ of (4.1.5) such that

$$f\left(\bar{x}\right) = 0, \bar{x} \in \mathbb{R}^n \tag{4.1.8}$$

or the orbit of remains at x^* forever, then x^* is the fixed point which can be written as

$$x_{k+1} = f\left(x_k\right) = f\left(x^*\right) = x^* \tag{4.1.9}$$

In general, the fixed point in (4.1.8) is **stable**[2] if it is able to return to its equilibrium region (neighbor) after disturbance as time goes to infinity. Or the fixed point in (4.1.9) is stable if its neighbor orbit is attracted. Figure 4.4 provides the examples of stable and unstable trajectories obtained from Kundur two-area system. As can be seen, the left trajectory converges after applying small disturbance while the right one diverges after large disturbance.

---

[1] The flow map satisfies the semi-group property [28].

[2] The stability refers to the asymptotic stability for simplicity.

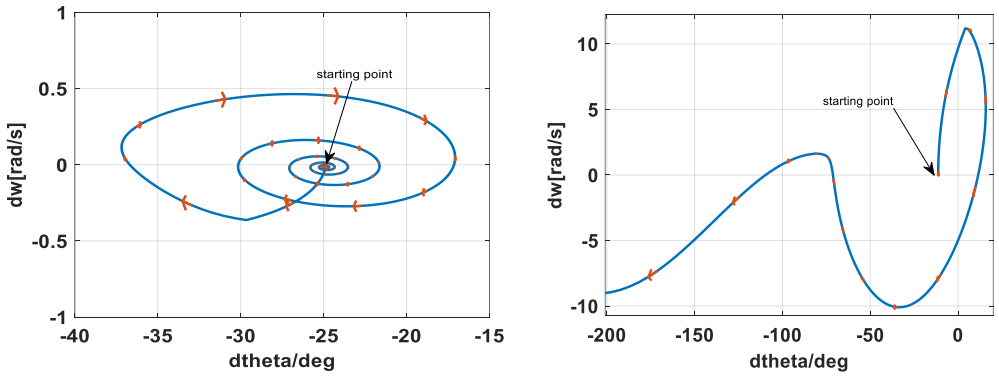

a) Converge case (small disturbance) b) Diverge case (large disturbance)

Figure 4.4 Converge and diverge case study of generator No.3

- Limit cycle

  The **limit cycles** are the isolated closed curves (trajectories) of the dynamical system [1]. If all the neighboring curves approach the corresponding limit cycle, then this limit cycle is stable. Otherwise it is unstable or half-stable [49]. The major difference between the limit cycle and closed orbit is that limit cycle only exists in nonlinear system. If you perturb a stable nonlinear system, if will return to the limit cycle. However, if you perturb a stable linear system, the disturbance will persist forever (it will jump to another closed orbit) if it has a periodic solution.

- Attractor

  An attractor *A* has the following properties [49]:

  a) It is an **invariant set**; *S* is an invariant set if any trajectory starting in *S* remains in *S* for all time.

  b) It attracts an open set *U* of initial conditions. The largest *U* is called the **basin of attraction** of *A.*

  c) It has no subset which can satisfies both a) and b). In other word, it is *minimal.*

[1] Isolated means that the neighboring curves are not closed.

The attractor can be a stable fixed point or a limit cycle. Any point in U will converge to it as time goes to infinity. Sometime the systems have more than one attractor but the union of the attractors is called attracting set.

- Bifurcation

  Bifurcation is the qualitative changes in the dynamics such as the fixed points creation/destruction, stability change and etc. For instance, the qualitative structure of the system can change along with its parameter variation [49], [54], [55].

4.1.3 Motivation of data-driven techniques

As mentioned in the beginning of this chapter, linear systems are easier to solve because they can be represented by the sum of several small parts by using Fourier analysis, Laplace transforms and so on. However, those methods fail in nonlinear systems because there are nonlinear interactions going on. Particularly, the solution becomes more complicated if the external force is added. The traditional way to solve the nonlinear system is to linearize it around the equilibriums. What if the system has a pretty high dimension such that the numerical solutions is unavailable? For example, turbulence system and power system are extremely nonlinear system with very high dimensions. Particularly, for the latter one, the uncertainties of renewable energy sources (RESs) increase the complexity of the system and also introduce uncountable degrees of freedom, because the renewable sources are varying as weather changes, temperature changes and so on [32], [56]. Besides, in a lot of cases, due to the interference of human beings the complexity of model increases dramatically [57]. As a result, the model of the system is unreachable. For instance, our brains which interact with the internal neural network do not follow simply differential or difference equations. The basic geometric properties and objects for those systems are extremely difficult to discover. Moreover, what if the system is perturbed by a large disturbance much further from the equilibrium? Do we have a robust model to deal with the large disturbance?

All the problems arisen force us to seek for other ways out. Thanks to the boost development in computers the data-driven methodologies have caused attention. Especially in the recent decades, data-driven methods for system identification and control have been undergoing a revolution due to the rise of big data applied in machine learning. Data-driven methodologies as the name

suggested, it is a technology that studies system from data [58]–[61]. It is especially suitable for designing controller of the systems who are characterized by strongly nonlinear and high-dimensional.

Koopman operator theory is a data-driven methodology which has recently gaining significant research interests as a systematic framework to obtain linear representation of nonlinear systems. Koopman operator theory will be illustrated in next section.

4.2 Koopman operator of autonomous nonlinear system

B. O. Koopman showed that a nonlinear dynamical system can be represented by a linear operator with infinite dimension on the Hilbert space of observables [62]. This linear operator is referred to as Koopman operator. Koopman operator is unitary meaning that it is a one to one transformation of the points in Hilbert space and such that the inner product of any two observables stay unchanged [62]. Many researches have shown that a lot of the classical properties of dynamical systems can be extended to Koopman formalism. For instance, it has been shown that the level sets of Koopman eigenfunctions can form the invariant partitions of the state space of the dynamical system [63]. An extension of the local linearization of the Hartman–Grobman theorem to the entire basin of attraction of a stable equilibrium or limit cycle has been shown by using the theory of Koopman operator. In addition, this linearization can be applied to flows as well as maps [64].

By applying Koopman operator the nonlinear system is turned into linear and high-dimensional which introduces new challenges. People are seeking for a way to obtain a finite approximation of Koopman operator which reserves the dynamical properties of the original system [24]. This approximated operator is promising for controlling and predicting the nonlinear system. Obtaining Koopman operator first requires the measurements of observables. Koopman operator is attractive in the ear of big data not only because it is only built upon measurement data, but also it can promise that a linear approximation of the nonlinear system can be obtained without the traditional linearization around one particular fixed point. A proper approximation can even enlarge the stability region around the equilibrium which will be shown in the case study in Chapter 7.

Here comes a new problem – what data should we use? In other word, which variables should we pick to form Koopman operator? Roughly speaking, these variables which can be utilized to generate the Koopman operator are called observables. In general, the observables are the functions of system states such that the observables contain the knowledge of the dynamics we are interested in. For example, considering the power system dominated by the swing equation given in (2.2.22) of each generator. Then rotor speeds and angles are governing the system dynamics. The good candidates of observables are the terminal bus voltages, the electrical power of generators and also the system frequency. Because the systems states (rotor speeds and angles) and the function of them determine where those observables are heading to. On the contrary, reactive power of the generator is not a good option of observable because it does not majorly depend on rotor angle and speed.

However, the system to be controlled given in Figure 4.1 is too complex to neither access to all the system states nor determining the observables using simple power system knowledge [65]. Thus, a method of determining observables that can deal with partial states or even no state information is required. To this end, a method for constructing Koopman operator for such a system (i.e. input-output system) will be illustrated in the last section of this chapter and next chapter. Now, let us start with the fundamental theory of Koopman operator.

4.2.1 Koopman operator for discrete-time system

In this section, the fundamental of Koopman operator will be reviewed. Discrete-time dynamics are consistent with experimental or simulation measurements. The collected measurement data has the nature of discrete-time. Besides, the discrete-time systems are more general than continuous-time system systems [24]. Therefore, we will begin with the discrete-time systems and then extend to the input-output system.

Recall the discrete-time system

$$x_{k+1} = T(x_k)$$

where $x_k \in \mathcal{M} \subset \mathbb{R}^n$ is the state vector of the system at time step *k*. It can also be written as

$$x^+ = T(x) \tag{4.2.1}$$

where x^+ is the future (successor) state. The Koopman operator $\mathcal{K}: \mathcal{F} \to \mathcal{F}$ is a linear transformation defined in the following form

$$\mathcal{K}g(x) = g(x) \circ T(x) \tag{4.2.2}$$

where $g: \mathbb{R}^n \to \mathbb{R}$ is named as **observable** of the system. g belongs to $\mathcal{F}$ which is the vector space (typically infinite-dimensional) formed by the set of all the observables. g is invariant under the action of Koopman operator. And $\circ$ denotes the composition of g with *T*, i.e.

$$\mathcal{K}g(x) = g(T(x)) \tag{4.2.3}$$

The Koopman operator $\mathcal{K}$ is a linear representation of the nonlinear dynamical system on space $\mathcal{F}$, meaning that the Koopman operator advances the observables linearly

$$g(x_{k+1}) = \mathcal{K}g(x_k) \tag{4.2.4}$$

It is worth noted that this operator significantly captures dynamics of the underlying system in the space of observables $\mathcal{F}$ which consists of the components of x's including x itself. The key property of Koopman operator is the linearity, i.e.,

$$\mathcal{K}(\alpha g_1 + \beta g_2) = \alpha \mathcal{K} g_1 + \beta \mathcal{K} g_2 \tag{4.2.5}$$

where α and β are constants, g_1 and g_2 are two observables. We call (ϕ_i, λ_i) an eigenfunction-eigenvalue pair of Koopman operator if they satisfy [25]

$$\mathcal{K}\phi_i = e^{\lambda_i t}\phi_i \tag{4.2.6}$$

where $\lambda_i \in \mathbb{C}$. Koopman eigenfunctions have the property that if (ϕ_i, λ_i) and (ϕ_j, λ_j) are two distinct eigenfunction-eigenvalue pairs, we have

$$\mathcal{K}(\phi_i, \phi_j) = (\phi_i, \phi_j) \circ \mathcal{K} = \mathcal{K}\phi_i \cdot \mathcal{K}\phi_j = e^{\lambda_i t}\phi_i \cdot e^{\lambda_j t}\phi_j = e^{(\lambda_i + \lambda_j)t}\phi_i\phi_j \tag{4.2.7}$$

Therefore, $\left(\phi_i\phi_j, \lambda_i + \lambda_j\right)$ is also an eigenfunction-eigenvalue pair. The state space dynamics can be characterized by the spectral properties of Koopman operator. For instance, since the Koopman eigenvalues are the point spectrums of Koopman operator, we can use Koopman

eigenvalues to evaluate the stability of the system. More properties can be found in [66]–[68]. With the assumption that all the observables of the system lie in the linear span, i.e.

$$g(x) = \sum_{i=0}^{\infty} v_i \phi_i(x) \tag{4.2.8}$$

where v_i's are the coefficient of the this Koopman expansion. Namely v_i's are Koopman modes associated with the Koopman eigenfunction-eigenvalue couple (ϕ_i, λ_i). According to (4.2.8), Koopman modes can be obtained by the projection of the corresponding observable and the eigenfunction. Then we can describe the evolution of the observables as

$$\mathcal{K}g(x) = \sum_{i=0}^{\infty} v_i \phi_i(x) e^{\lambda_i t} \tag{4.2.9}$$

It has been proved that Koopman linear expansion in (4.2.9) applies to a large class of nonlinear dynamical systems such as the one with limit cycles, hyperbolic fixed points and etc. see [69] for detailed examples.

4.2.2 Koopman operator for continuous-time system

Previously, we have focused on the Koopman operator formalism for discrete-time system in order to be consistent with the measurement data from real-life experiments or simulations. Now, the analysis carries over to continuous-time systems for the purpose of completeness of the dissertation.

Consider the continuous-time system

$$\dot{x} = f(x)$$

Since it is continuous-time system, we can define a one-parameter semi-group of Koopman operators $\{\mathcal{K}^t\}_{t \geq 0}$ such that each component of this group is given by

$$\mathcal{K}^t g(x) = g(x) \circ F^t(x) \tag{4.2.10}$$

where g is again the observable of the system. The above equation can be written as

$$\mathcal{K}^t g(x) = g(F^t(x)) \tag{4.2.11}$$

This system also follows the linearity of the composition operation and the property given in (4.2.7) and the evolution of observables

$$\mathcal{K}^t g(x) = \sum_{i=0}^{\infty} v_i \phi_i(x) e^{\lambda_i t} \tag{4.2.12}$$

which shows that $\mathcal{K}^t g(x)$ is sum of infinite terms of sinusoid and exponential.

4.3 Koopman linear predictor of non-autonomous nonlinear system[1]

4.3.1 Koopman linear predictor basis

In this section, Koopman operator is extended to the non-autonomous systems (controlled systems), i.e.

$$x^+ = T(x, u) \tag{4.3.1}$$

where $u \in \mathcal{U} \in \mathbb{R}^m$ is the control input. The goal of this work is to reconstruct the nonlinear dynamics in a linear framework such that the trajectory of the nonlinear system can be predicted by the linear predictor; this predictor is an approximation of Koopman operator, i.e.

$$\begin{cases} z^+ = Az + Bu \\ \hat{x} = Cz \end{cases} \tag{4.3.2}$$

where $z \in \mathbb{R}^N$ with some $N \gg n$, and $\hat{x}$ is the prediction of x, $A \in \mathbb{R}^{N \times N}$, $B \in \mathbb{R}^{N \times m}$ and $C \in \mathbb{R}^{n \times N}$ [33]. The initial condition of (4.3.2) is given by

$$z_0 = g(x_0) = \left[g_1(x_0), ..., g_N(x_0) \right]^T \tag{4.3.3}$$[2]

where $g_i : \mathbb{R}^n \to \mathbb{R}, i = 1, ..., N$ are the user-defined observables (typically nonlinear). We can also call it as lifting function since its responsibility is to lift the low-dimensional nonlinear system to a high-dimensional linear system. The resultant state z is referred to as the lifted state.

---

[1] We only consider the discrete-time system from now.

[2] Unlike the previous definition, the number of g is finite due to the approximation of Koopman operator.

This linear predictor enables the application of the existing powerful optimal and robust control technologies for linear systems such as H_∞ , LQR, model predictive control (MPC) and etc. to fulfill the frequency/voltage control in Figure 4.1. It is worth to note that the control input u will remain unlifted and therefore we can impose linear constraints on the input signals [33]. Furthermore, linear constraints can also be imposed to $\hat{x}$ since it is a linear function of z .

However, the predictor is not always accurate for all future time. Fortunately, if the predictor can provide prediction within long enough time interval, it will be readily facilitating the use of linear control technologies. Particularly, MPC is suitable for this purpose since it only requires the prediction of a finite-time window to calculate the control signals.

4.3.2 Koopman operator for non-autonomous system

A lot of work has been done to generalize the Koopman operator to controlled systems [27], [70]. In this work, in order to obtain the linear predictor (4.3.2), a rigorous and practical generalization presented in [33] is adopted. The Koopman operator under controlled setting is working with the extended state space which is defined as the Cartesian product of the original state space and the space of all the control sequences, i.e.

$$\mathcal{S} = \mathbb{R}^n \times \ell(\mathcal{U}) \tag{4.3.4}$$

where $\ell(\mathcal{U}) = \left\{(u_i)_{i=0}^{\infty} \mid u_i \in \mathcal{U}\right\}$ is the space of all input sequences u_i . The extended state

$$\chi = \begin{bmatrix} x \\ \boldsymbol{u} \end{bmatrix} \tag{4.3.5}$$

is descried by

$$\chi^+ = T(\chi) = \begin{bmatrix} T(x, u_0) \\ S_u \boldsymbol{u} \end{bmatrix} \tag{4.3.6}$$

where S_u denotes the shift operator which shift the i$^{\text{th}}$ of input sequence $\boldsymbol{u}$ to the next one, i.e. $S_u u_i = u_{i+1}$ [33]. Given the observable $\psi : \mathcal{S} \to \mathbb{R}$, the Koopman operator of the controlled system can be defined as

$$\mathcal{K}\psi(\chi) = \psi\left(T(\chi)\right) = \mathcal{K}\psi(x, (u_i)_{i=0}^{\infty}) = \psi\left(T(x, u_0), (u_i)_{i=1}^{\infty}\right) \tag{4.3.7}$$

4.3.3 EDMD for non-autonomous systems

In this section, a finite-dimensional approximation of the Koopman operator $\mathcal{K}$ is constructed using the extended dynamic mode decomposition algorithm (EDMD) proposed in [71] under controlled setting. EDMD is a data-driven algorithm that only requires (a) a data set of snapshot pairs

$$(\chi_j, \chi_j^+), \quad j = 1,...,K \tag{4.3.8}$$

and (b) a dictionary of scalar observables

$$\psi(\chi) = \left[\psi_1(\chi),...,\psi_{N_\psi}(\chi)\right] \tag{4.3.9}$$

which is a vector of the observables $\psi_i : \mathcal{S} \to \mathbb{R}, i = 1,...N_\psi$. According to [33], the observables ψ_i's are imposed in the special form

$$\psi_i(\chi) = \psi_i(x, \boldsymbol{u}) = g_i(x) + \mathcal{L}_i(\boldsymbol{u}) \tag{4.3.10}$$

where g_i is the same as in (4.3.3) and $\mathcal{L}_i : \ell(\mathcal{U}) \to \mathbb{R}$ is linear. With the assumption that $N_\psi = N + m$, the vector of the observables can be expressed as

$$\psi(x, \boldsymbol{u}) = \begin{bmatrix} g(x) \\ u_0 \end{bmatrix} \tag{4.3.11}$$

where $g = \left[g_1,..., g_N\right]^T$ and u_0 is the first element in input sequence. The approximation $\boldsymbol{K}$ of $\mathcal{K}$ is then given by the solution of the least-squares problem[1]

$$\min_{\boldsymbol{K}} \sum_{j=1}^{K} \left\| \psi(\chi_j^+) - \boldsymbol{K}\psi(\chi_j) \right\|_2^2 \tag{4.3.12}$$

However, the future values of the control sequence are out of interest. As a result, the last m terms of (4.3.12) can be discarded [33]. Let us only consider the first N rows of $\boldsymbol{K}$ denoting by $\boldsymbol{K}^N$, this matrix can be decomposed as

[1] This problem does not have multiple isolated local minima. It must have either a unique global minimizer (solution) or a continuous family (or families) of minimizers [71].

$$\boldsymbol{K}^N = [A, B] \tag{4.3.13}$$

where $A \in \mathbb{R}^{N\times N}$ and $B \in \mathbb{R}^{N\times m}$ are the ones defined in the linear predictor (4.3.2). With these notation, (4.3.12) can be rewrite as

$$\min_{\boldsymbol{A},\boldsymbol{B}} \sum_{j=1}^{K} \left\| g(x_j^+) - \boldsymbol{A} g(x_j) - \boldsymbol{B} u_{j,0} \right\|_2^2 \tag{4.3.14}$$

where $u_{j,0}$ is the first element of the control sequence at time *j*. The matrix *C* is obtained by another least-squares problem

$$\min_{C} \sum_{j=1}^{K} \left\| x_j - \boldsymbol{C} g(x_j) \right\|_2^2 \tag{4.3.15}$$

The solutions of (4.3.14) and (4.3.15) give us the predictor of the form (4.3.2) which starts from the initial condition $z_0 = g(x_0) = [g_1(x_0), ..., g_N(x_0)]^T$.

4.3.4 Numerical solution for the Koopman linear predictor

In order to obtain the numerical solution of matrices ***A***, ***B***, and ***C***, the first step is to collect the following data sets from experiments or simulations

$$\begin{cases} \boldsymbol{X} = [x_1, ..., x_K] \\ \boldsymbol{Y} = [x_1^+, ..., x_K^+] \\ \boldsymbol{U} = [u_1, ..., u_K] \end{cases} \tag{4.3.16}$$

where $x_j^+ = T(x_j, u_j)$. [1] Next, the data sets are lifted by a given vector of observables[2]

$$\begin{cases} \boldsymbol{X}_{lift} = [g(x_1), ..., g(x_K)] \\ \boldsymbol{Y}_{lift} = [g(x_1^+), ..., g(x_K^+)] \\ \boldsymbol{U} = [u_1, ..., u_K] \end{cases} \tag{4.3.17}$$

where

---

[1] Note that we neither need to arrange the data in any temporal order nor to collect the data from single trajectory.

[2] We do not lift ***U*** data set to remain the linear dependence of the predictor on the original control signals.

$$g(x_j) = \left[g_1(x_j), ..., g_N(x_j) \right], \; j = 1, ..., K \tag{4.3.18}$$

Matrices $\boldsymbol{A}$, $\boldsymbol{B}$, and $\boldsymbol{C}$ are obtained by solving the least-squares problems [33]

$$\min_{\boldsymbol{A},\boldsymbol{B}} \left\| \boldsymbol{Y}_{lift} - \boldsymbol{A}\boldsymbol{X}_{lift} - \boldsymbol{B}\boldsymbol{U} \right\|_F, \;\; \min_{\boldsymbol{C}} \left\| \boldsymbol{X} - \boldsymbol{C}\boldsymbol{X}_{lift} \right\|_F \tag{4.3.19}$$

where $\|\cdot\|_F$ denotes the Frobenius norm. The analytical solution of these two optimizing problems are

$$\begin{bmatrix} \boldsymbol{A} & \boldsymbol{B} \\ \boldsymbol{C} & \boldsymbol{0} \end{bmatrix} = \begin{bmatrix} \boldsymbol{Y}_{lift} \\ \boldsymbol{X} \end{bmatrix} \begin{bmatrix} \boldsymbol{X}_{lift} \\ \boldsymbol{U} \end{bmatrix}^{\dagger} \tag{4.3.20}$$

In practice, if the size of the data sets are too large $K \gg N$, it is more computational friendly to solve this equation [33]

$$\boldsymbol{V} = \boldsymbol{M}\boldsymbol{G} \tag{4.3.21}$$

where

$$\begin{cases} \boldsymbol{V} = \boldsymbol{Y}_{lift} \begin{bmatrix} \boldsymbol{X}_{lift} \\ \boldsymbol{U} \end{bmatrix}^T \\ \boldsymbol{G} = \begin{bmatrix} \boldsymbol{X}_{lift} \\ \boldsymbol{U} \end{bmatrix} \begin{bmatrix} \boldsymbol{X}_{lift} \\ \boldsymbol{U} \end{bmatrix}^T \end{cases} \tag{4.3.22}$$

The solution is then given by

$$\boldsymbol{M} = [\boldsymbol{A}, \boldsymbol{B}] \tag{4.3.23}$$

Note that, as indicated in section 4.2.1, the observables also include the original state *x*'s. Hence, matrix $\boldsymbol{C} = [\boldsymbol{I}, \boldsymbol{0}]$ after a proper reorder of the observables. By doing so, the sizes of $\boldsymbol{G}$ and $\boldsymbol{V}$ are $(N+m)\times(N+m)$ and $N\times(N+m)$ respectively which is decoupled from the number of data points *K*.

4.4 Construction of Koopman operator for Input-Output systems

Previously, we assume that the system states are all available. However, we are facing a large power system which contains a large number of states and most of them are not readily measureable. The system to be controlled in Figure 4.1 is a typical Input-Output system whose

internal dynamics is unknown likes a "*Black box*". Only the input-output data pairs (u, y) are reachable. For example, $(P \,||\, Q, \textit{frequncy} \,||\, \textit{voltage})$ is the input-output data pair of the system in Figure 4.1. In this respect, we consider the system of this form

$$y = h(x) \tag{4.4.1}$$

where y is the instantaneously measured output of the system and $h : \mathbb{R}^n \to \mathbb{R}^h$. x satisfies $x^+ = T(x,u)$. Now a correct choice of observable is extremely important to have a truly linear system in a large region in the original state space. A single frequency/voltage measurement is insufficient to observe the system dynamics and therefore we can take high order derivatives of the output and input themselves in the form of time-delay embedding ζ given by

$$\begin{aligned} \zeta_k &= \left[y_k^T, ..., y_{k+n_{dy}-1}^T, u_k^T, ..., u_{k+n_{du}-1}^T \right]^T \\ \zeta_k{}^+ &= \left[y_{k+1}^T, ..., y_{k+n_{dy}}^T, u_{k+1}^T, ..., u_{k+n_{du}}^T \right]^T \end{aligned} \tag{4.4.2}$$

where n_{dy} and n_{du} are the number of output and input delay embedding respectively. Delay embedding is a classical theory in system identification [72] as well as in the Koopman operator approximation [25], [26], [33], [73]. By embedding the time-delay measurements on all input and output data, we can form the new matrices

$$\begin{cases} \boldsymbol{X}^{'} = [\zeta_1, ..., \zeta_K] \\ \boldsymbol{Y}^{'} = [\zeta_1^+, ..., \zeta_K^+] \end{cases} \tag{4.4.3}$$

Similarly, after applying the observable functions *g*, we have

$$\begin{cases} \boldsymbol{X}_{lift}^{'} = [g(\zeta_1), ..., g(\zeta_K)] \\ \boldsymbol{Y}_{lift}^{'} = [g(\zeta_1^+), ..., g(\zeta_K^+)] \end{cases} \tag{4.4.4}$$

The least-squares problems become

$$\min_{\boldsymbol{A},\boldsymbol{B}} \left\| \boldsymbol{Y}_{lift}^{'} - \boldsymbol{A}\boldsymbol{X}_{lift}^{'} - \boldsymbol{B}\boldsymbol{U} \right\|_F, \quad \min_{\boldsymbol{C}} \left\| \zeta_y - \boldsymbol{C}\boldsymbol{X}_{lift}^{'} \right\|_F \tag{4.4.5}$$

where ζ_y is the most recent embedding coordinate. The linear predictor is constructed as

$$\begin{cases} z^{+} = Az + Bu \\ \hat{y} = Cz \end{cases} \tag{4.4.6}$$

where $\hat{y}$ is the prediction of the output most recent output *y*. The resultant initial condition of this predictor is $z_0 = g(\zeta_0)$ [25], [33].

More rationale behind the time-delay embedding technique will be given in Chapter 5 including Takens theory and the algorithms for choosing optimal embedding dimension.

Chapter 5 Time-Delayed Embedding

As mentioned in the previous chapters, it is extremely rare that we can measure all the states of the nonlinear systems. So how do we discover the underlying dynamical system with limited information? In this chapter, a classical technique called time-delayed embedding which can be utilized to reveal the unknown system dynamics will be introduced. The process of going from observed measurements to a dynamical model is fundamental in engineering. In general, we can reconstruct the unknown nonlinear dynamical system by constructing a new state space by means of the delayed version of the measured data itself. Typically, Takens theorem provides the theoretical foundation of basically all time-delayed embedding analyses. In general, by constructing a new state space by means of consecutive observed scalar time series values, we will be able to reconstruct the underlying unknown dynamical system.

5.1 Takens embedding theorem

Takens embedding theorem is very powerful theorem proved by Floris Takens that generically the one can reconstruct a shadow version of the original manifold simply by looking at one of its time series projections. Here is Theorem 1 of Takens' paper [74]:

Theorem 1 (Takens 1981) *Let M be a compact manifold of dimension n. For pairs* (φ, y) , $\varphi : M \to M$ *a smooth diffeomorphism which is at least* C^2 *and* $y : M \to \mathbb{R}$ *a smooth observable function, it is a generic*[1] *property that the map* $\Phi_{(\varphi,y)} : M \to \mathbb{R}^{2n_d+1}$ *is an embedding, defined by*

$$\Phi_{(\varphi,y)}(x) = (y(x), y(\varphi(x)), ..., y(\varphi^{2n_d}(x))) \tag{5.1.1}$$

The word '*diffeomorphism'* means a one-to-one mapping from the one to the other which is invertible and differentiable in both directions. According to Takens theory, if you have the correct data and you also do the embedding correctly, the results are guaranteed to be '*topologically'* identical to the true dynamics. Here comes the question, how the word topologically is related to diffeomorphic? '*Topology'* is the fundamental mathematics of shape. This is very different from the word '*geometry'.* Geometry has the word metric buried in it. And metric is a way to measure something which topology does not have. Roughly speaking, when we discuss about the topology of an object, only the number of pieces or the number of holes matters. For instance, the colander in Figure 5.2 has very different topology than the bowl because the colander has hundreds of holes in it although they do have the same geometry. However, the coffee mug and donut in Figure 5.1 has the same topology but different geometry because they both have one hole and one piece. This is a very famous example of topology. Imagine the mug and donut are both made out of clay or plasticine, the mug can be continually deformed without piercing any holes or creating pieces to a donut and vice versa. The mathematical form of transformation like this deforming of clay that does not create or break pieces or holes is called a diffeomorphism. Therefore, a diffeomorphism which preserves topology has the same shape as the original manifold qualitatively. Many of the important properties such as the Lyapunov exponents are invariant under this transformation. And a correct embedding is related to the true dynamics by such a transformation if the conditions in Theorem 1 are met. All of that means that we can measure one variable from a very complex system and form the embedding coordinates to reconstruct the original dynamics.

---

[1] Generic means open and dense, and we use C^1 topology. The functions $y \in C^2(M, \mathbb{R})$ is referred to as measurement functions.

Figure 5.1 Objects have same topology

Figure 5.2 Objects have same geometry

Now let us connect Takens theory to the autonomous n-dimensional nonlinear discrete system of the form

$$\begin{aligned} x_{k+1} &= T(x_k) \\ y_k &= h(x_k) \end{aligned} \tag{5.1.2}$$

where $x \in \mathbb{R}^n$ is the system state the at time step *k*. and $T : \mathcal{M} \to \mathcal{M}$ is the dynamic map. y_k is a measurement and $h : \mathcal{M} \to \mathbb{R}$ is the measurement function. According to Taken theory, by constructing the scalar time-delay coordinate $\zeta_{n_d,k}$ of any individual point y_k with its past history from system trajectory, we can reconstruct the nonlinear system under mild conditions.

$$\zeta_{n_d,k} = \left[y_k, y_{k+\tau}, ..., y_{k+\tau n_d} \right],\ k = 1, ..., K - \tau n_d \tag{5.1.3}$$

where n_d is the embedding dimension and τ is the time delay. K is the number of the data points.

5.2 Extension of Takens theory - input-output systems

Modelling input-output systems is necessary in many applications. For instance, the conventional synchronous generator requires governor and exciter to maintain the power system stability. Takens theorem was extended to non-autonomous (forced) systems in [35], [75], [76]. However, we may only have access to the input-output data pairs for those systems. In 1992, the input-output systems have been considered in this context by Martin Casdagli [35]. He proposed a method of constructing time-delay embedding coordinates adapted to the input-output systems. Consider such a system in Figure 5.3

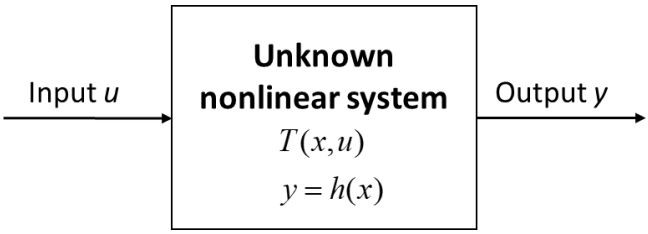

Figure 5.3 Input-output system diagram

which is defined as

$$\begin{aligned} x_{k+1} &= T(x_k, u_k) \\ y_k &= h(x_k), \quad h: \mathbb{R}^n \to \mathbb{R}^h \end{aligned} \tag{5.2.1}$$

[1]

where $y \in \mathbb{R}^h$ is the measured output of the system and $u \in \mathbb{R}^m$ is the input. It is hypothesized that the following relationship holds

$$y_k = T(\zeta_{N_d,k}) \tag{5.2.2}$$

where

$$\zeta_{N_d,k} = \left[y_k^T, y_{k+\tau}^T, ..., y_{k+\tau n_{dy}}^T, u_k^T, u_{k+}^T, ..., u_{k+\tau n_{du}}^T \right]^T \tag{5.2.3}$$

is the delay embedding coordinate, k is the time stamp. And T is a function fitted to the input-output sequential data. The results from [75], [76] in essence prove Casdagli's conjecture [35] on

[1] In [35], u and y are both scalars. Here they are generalized to multidimensional vector.

embedding such systems[1]. However, in Casdagli's paper [35], there is no direct method to determine the embedding dimensions for both input and output. Next section will introduce two algorithms to determine optimal embedding dimension as well as their extensions to input-output systems.

5.3 Time delay - Auto mutual information

Before we calculate the optimal embedding dimension, we need to consider another problem: Is every sampled point needed? Let us consider the Lorenz system which is defined as

$$\begin{cases} \dot{x} = \sigma(y - x) \\ \dot{y} = x(\rho - z) - y \\ \dot{z} = xy - \beta z \end{cases} \tag{5.3.1}$$

where the parameters $\sigma = 10, \rho = 28, \beta = 8/3$ are the typical values commonly used. If we measure variable *x* with 0.01 sampling time, we get the following plot. As can be seen from the plot, if we take every point in this trajectory to reconstruct the system we will oversample the *x*. In fact, we may only need 25 points to draw the same trace which originally has 300 points, see Figure 5.4 and 5.5.

[1] Note that, in Casdagli's paper, the delay embedding coordinate is constructed with a scalar input which is extended to the one with *m*-dimensional input in this work, i.e. $u \in \mathbb{R}^m$.

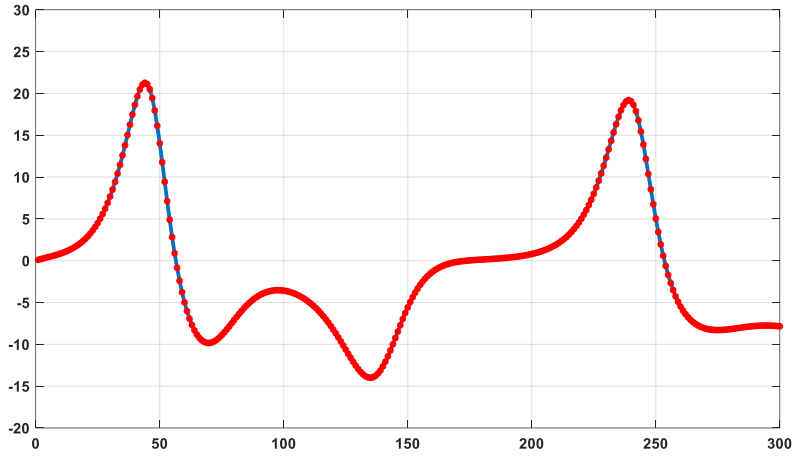

Figure 5.4 Trajectory of *x* with 0.01s sampling time

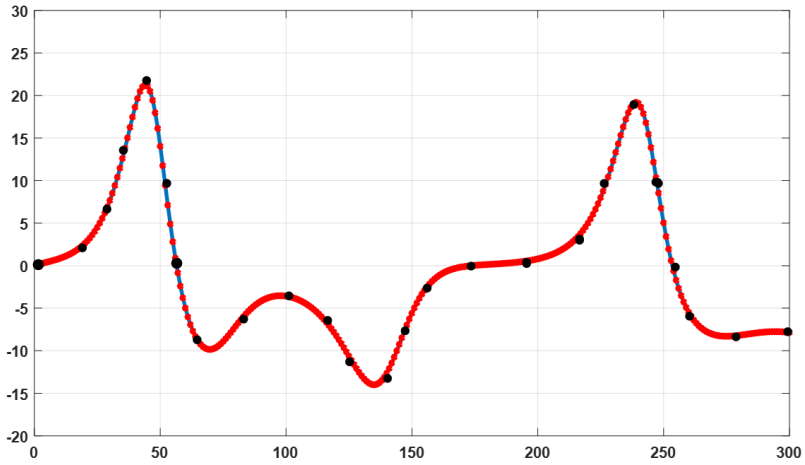

Figure 5.5 Trajectory of *x* with 0.12s sampling time

In order to calculate the optimal time delay between y_k and y_{k+1}, Fraser and Swinney proposed a method to compute the time delay such that the delayed coordinates are as uncorrelated between each other as possible [77]. In other word, they developed a way to quantify dependence between the original time series y_k and its time-shifted version $y_{k+\tau}$ as mutual information $I(y_k; y_{k+\tau})$. The mutual information between y_k and $y_{k+\tau}$ is named as average (auto) mutual information (AMI). It is formulated as

$$I(y_k, y_{k+\tau}) = \sum_{i,j} p_{ij}(\tau) \log\left(\frac{p_{ij}(\tau)}{p_i p_j}\right) \tag{5.3.2}$$

where p_i is the probability that y_k is in bin i of the histogram drawn from the data points in y, and $p_{ij}(\tau)$ is the probability that y_k is in bin i while $y_{k+\tau}$ is in bin j.

Now the question is what does (5.3.2) mean? Let us first quantify the amount of information. The amount of information is named as entropy. In general, entropy is the average amount of information sent by an event considering all the possible outcomes. Entropy is formulated as

$$H(X) = -\sum_{x \in \mathcal{X}} P(x) \log P(x) \tag{5.3.3}$$

where $P(x)$ is the possibility of every x in $\mathcal{X}$. For example, If the weather station tells you there is 75% possibility that tomorrow will be sunny and 25% possibility that tomorrow will be rainy. We can quantify the amount of information obtained from the weather station by calculating its entropy as

$$H = -0.75 \times \log(0.75) - 0.25 \times \log(0.25) = 0.81$$

Now we can answer the question, AMI tells us the amount of information obtained about y_k through observing $y_{k+\tau}$. Generally, the less y_k and $y_{k+\tau}$ are correlated, the smaller the $I(y_k, y_{k+\tau})$. As shown in Figure 5.6, the less the two circles are overlapping the smaller the AMI.

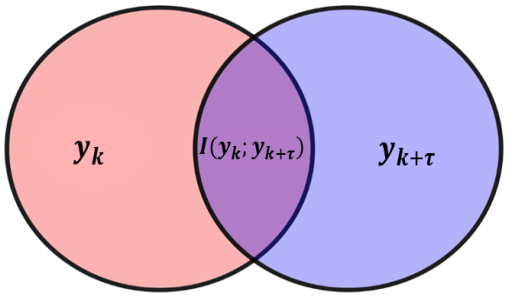

Figure 5.6 Mutual information diagram

There are various way to select τ such as the position of the first minimum [77]. However, the local minimum may not be able to locate in practice [78]. [79] provides another method to look for τ; AMI may monotonically decrease as a function of τ and τ is the smallest number for

which AMI reaches the value *1/e*. The previous discussion about AMI is for scalar time series data, what if we have a multidimensional time series data? [80] proposed a uniform multivariate AMI method; τ is estimated by averaging over the AMI of all variables. The paper adopts this method for simplicity.

As a result, the process of AMI computation can be drawn by the following flowchart

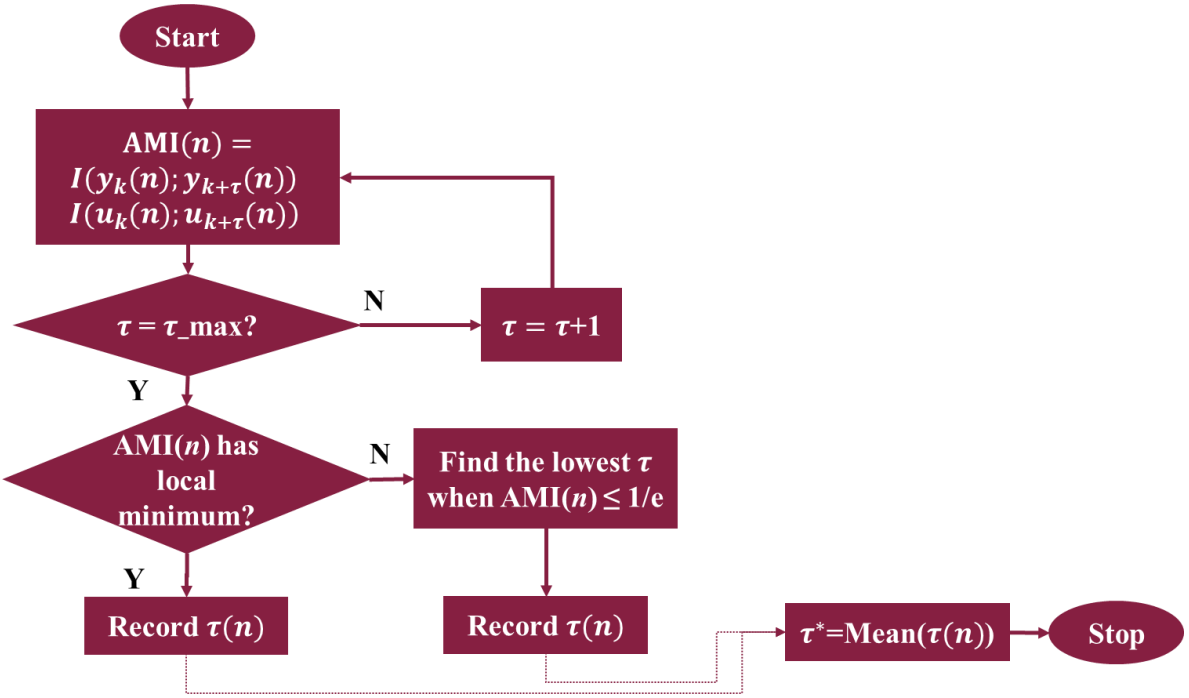

Figure 5.7 Flowchart of multivariate AMI procedure

where

$$I(V_k, V_{k+\tau}) = \sum_{i,j} p_{v,ij}(\tau) \log\left(\frac{p_{v,ij}(\tau)}{p_{v,i}\, p_{v,j}}\right) \tag{5.3.4}$$

$$V_k = \left[y_1, \ldots, y_h, u_1, \ldots, u_m\right]^T$$

Take the Lorenz system as example, the AMI of *x* and for all the variables are given in the figures below. Since the AMI of *x* and *y* cannot reach *1/e*, τ is computed as the mean of the time lags of the local minimum of all the three variables.

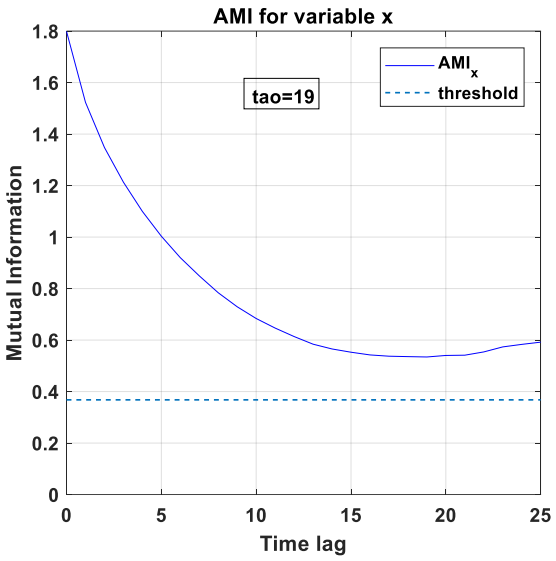

Figure 5.8 AMI of *x*

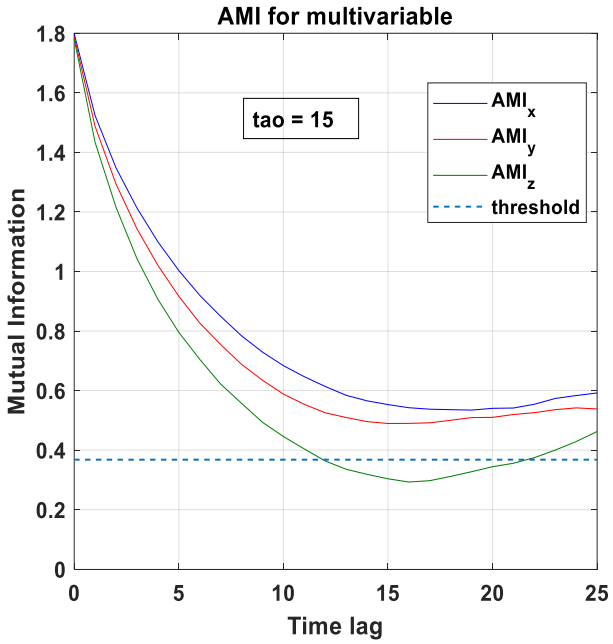

Figure 5.9 AMI for *x*, *y*, *z*

5.4 Optimal embedding dimension algorithms

Takens theory states that under mild conditions, the time-delay vector with embedding dimension $n_d \geq 2n+1$ can certainly construct the diffeomorphism of the original state space. However, this inequality is a sufficient but not necessary condition. In other words, you may be

able to get away with fewer embedding dimension which also reconstruct the dynamics accurately.

For instance, the Lorenz system is a three-dimension system. According to Takens theory, we need as least seven time-delay in the embedding coordinate to assure that the reconstruction is true embedding. However, it has been shown that you can successfully embed data from the Lorenz system in three dimensions [78]. Now the question is: why do we pick three as the number of embedding?

5.4.1 False nearest neighbor algorithm

False Nearest Neighbor (FNN) is a standard method to estimate the optimal embedding dimension. It was first introduced by Kennel *et al* in [34]. The neighboring points refer to two data points that are adjacent to each other. In order to determine whether the embedding dimension is sufficient, we examine the distance between these two points. This process is repeated for all the data points, the percentage of the points which have FNN is calculated before we continue to higher dimension. If the distance does not change appreciable (the percentage of FNN drops to zero or a small value), then this is the embedding dimension we are looking for. Otherwise, a higher embedding is needed. Figure 5.10 provides a simple example to illustrate the basic idea of FNN.

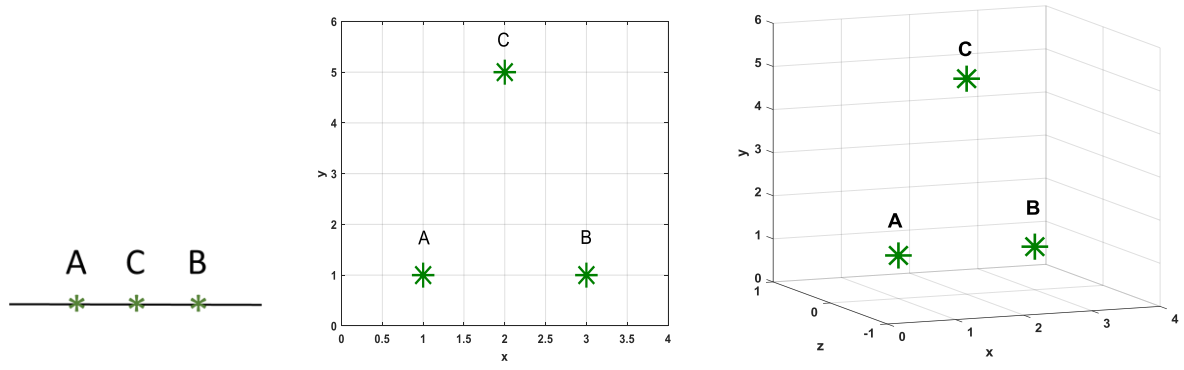

(a) n_d =1 (b) n_d =2 (c) n_d =3

Figure 5.10 Example of true nearest neighbors with different embedding dimension n_d

Point *A*=(1,1), *B*=(3,1), *C*=(2,5) are three points in a two-dimension state space as shown in Figure 5.10. *A* and *B* are true nearest neighbors in the original state space. However, by

projecting these three points onto one-dimension space, *A* and *C* become neighbors which is against the truth. If we further embed the space onto a three-dimensional one, we can still identify *A* and *B* as the true nearest neighbors. However, we choose the minimum embedding dimension n_d =2 as the optimal embedding dimension. Now, we move to the numerical procedure of FNN.

Consider the autonomous system in (5.1.2), FNN algorithm first identifies the nearest neighbors of each embedded point $\zeta_{n_d,k}$ in the n_d - dimensional embedding coordinate. The dimension n_d is estimated by evaluating the change in distance between neighbors, as we literately embed the phase space with a higher dimension. If conditions (5.4.1) and (5.4.2) are both satisfied then those neighbors are true, vice versa. The optimal embedding dimension is obtained when the proportion of FNN becomes adequately small and remains from then on.

$$\sqrt{\frac{R_{n_d+1,k}^2 - R_{n_d,k}^2}{R_{n_d,k}^2}} \le R_{tol} \tag{5.4.1}$$

$$\frac{R_{n_d+1,k}}{R_A} \le A_{tol} \tag{5.4.2}$$

where

$$R_{n_d,k} = \left\| \zeta_{n_d,k} - \zeta_{n_d,k}^r \right\|_2 \tag{5.4.3}$$

where $\zeta_{n_d,k}^r$ is the nearest neighbor of $\zeta_{n_d,k}$. R_A is the approximation of the attractor size. R_{tol} and A_{tol} are user-defined threshold parameters. $R_{n_d,k}$ is the Euclidean distance between point *k* and its nearest neighbor with n_d embedding. $R_{n_d+1,k}$ is the Euclidean distance between point *k* and its nearest neighbor with n_d+1 embedding. Going from n_d to n_d+1 embedding dimension can be achieved by adding a new embedding to $\zeta_{n_d,k}$, i.e.

$$R_{n_d+1,k}^2 = R_{n_d,k}^2 + \left\| y_{k+nd} - y_{k+nd}^r \right\|^2 \tag{5.4.4}$$

where $(\cdot)^{r}_{k,n_d}$ is the point such that $\zeta^{r}_{n_d,k}$ is the nearest neighbor of $\zeta_{n_d,k}$[1]. As indicated above, if the optimal embedding dimension is arrived, the distance between $\zeta_{n_d,k}$ and its neighbor should not change appreciably. '*appreciable*' is defined by the user-defined threshold R_{tol}. Furthermore, in real life, the collected data contains a lot of noise signals which may affect the result [81]. Therefore, another criterion is in used. The distance $R_{n_d+1,k}$ with respect to the attractor size should be less than another user-defined threshold parameter A_{tol}. This is used to distinguish the noises from the signals [34]. FNN algorithm can be summarized in the flowchart below.

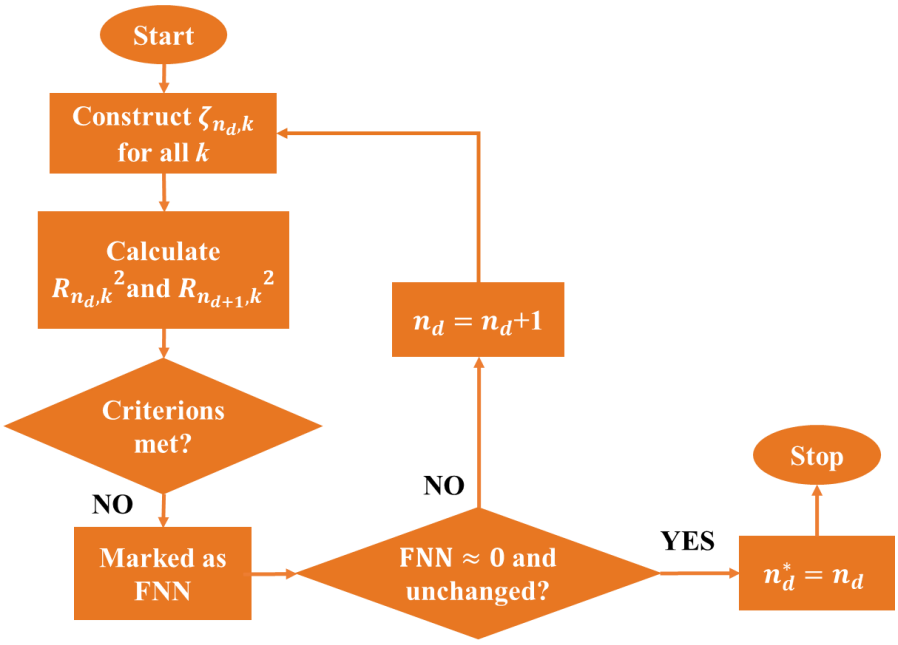

Figure 5.11 Flowchart of FNN

Take the Lorenz system in (5.3.1) as an example again to implement FNN algorithm. First, we collect the data from variable *x*, *y*, *z*. The corresponding Lorenz system is shown in Figure 5.12. Then we apply FNN algorithm for variable *x* with $R_{tol}=10$ and $A_{tol}=2$. These two thresholds are chosen according to [34]. The result is given in Figure 5.13. As can been seen from the plot, the optimal number of delayed embedding is 2 and hence the embedding dimension is 3; the current measurement is also needed to be included in the embedded space. Then We form the

[1] Note that, even though FNN is proposed originally for scalar time series data, it can be easily applied to multidimensional time series data as shown in [78].

three time-delay embedding coordinates of x as shown in Figure 5.14. With these three embedding coordinates, the phase-space is reconstructed as shown in Figure 5.15. It is obvious that the resulting phase-space is the diffeomorphism of original Lorenz system in Figure 5.12 due to the same topology. As we expect, the system dynamics is reconstructed with a smaller embedding dimension than the one given by Takens theory (d=7).

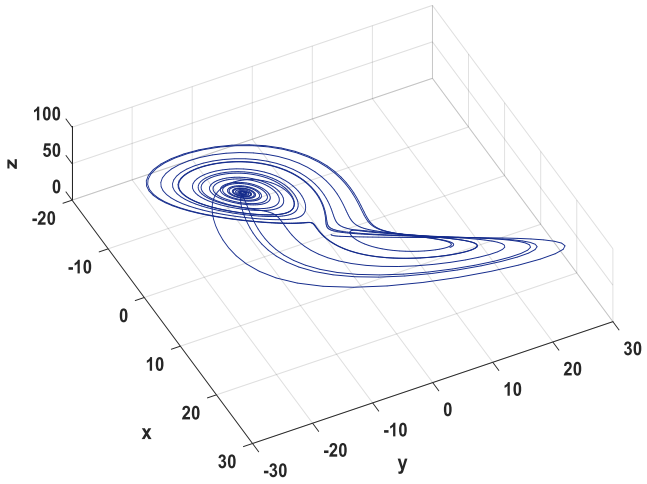

Figure 5.12 Lorenz system

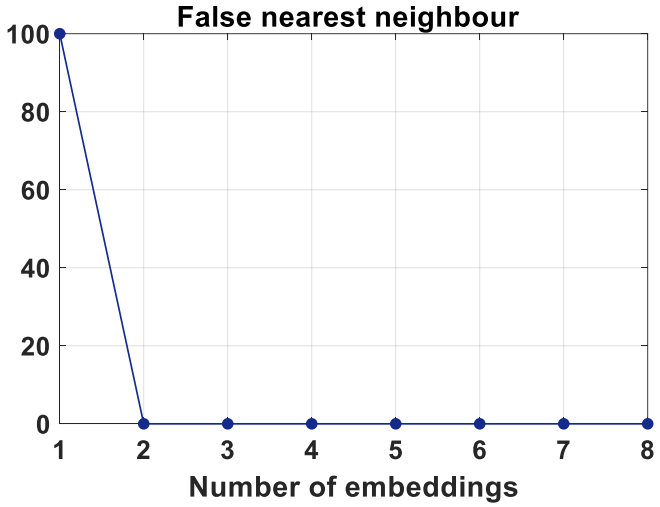

Figure 5.13 FNN plot of Lorenz system

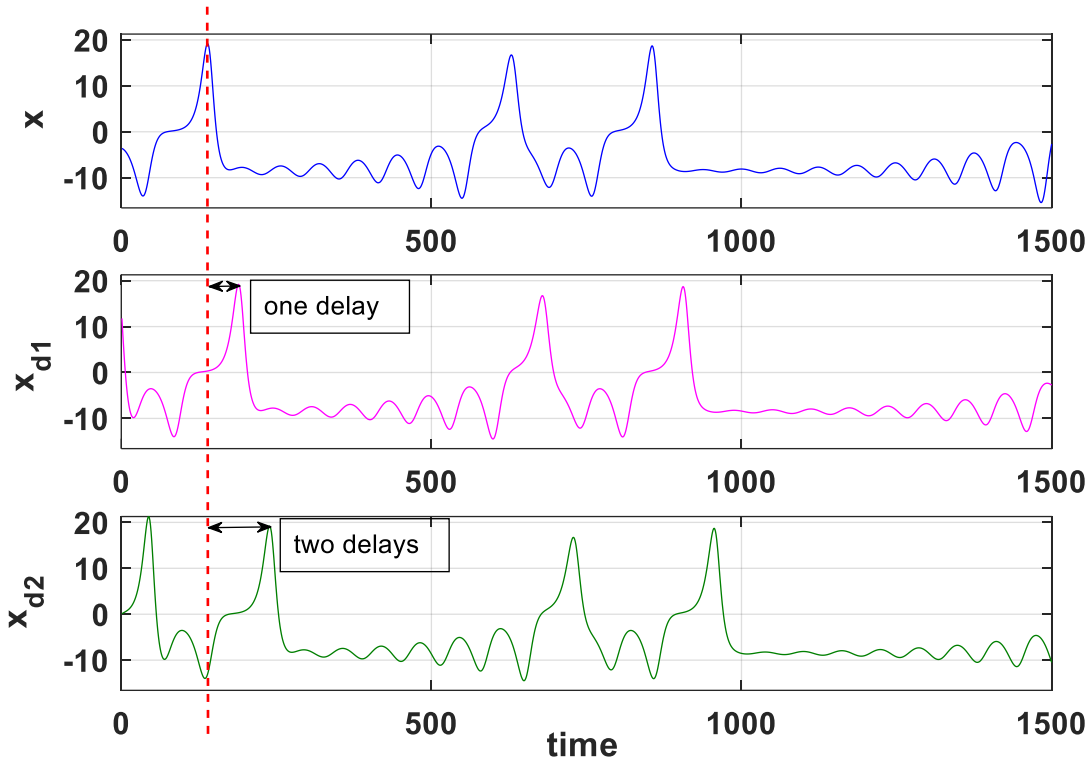

Figure 5.14 Time series data of *x*-axis for number of zero, one and two lags.

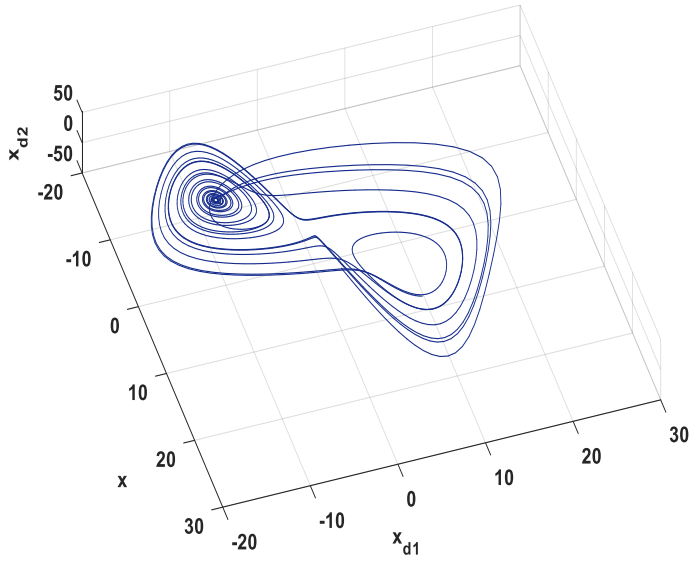

Figure 5.15 Reconstructed Lorenz system

5.4.2 False nearest neighbor algorithm for input-output systems

As explained in Chapter 4 and Section 5.2, a lot of systems especially in the area of engineering have control inputs in reality. We may have very limited access to the measurements of the system states due to the complexity of the system. As a result, the system becomes a blackbox which only allows us to collect the data of input and output signals.

Carl *et al* [37] extended FNN to the single-input-single-output (SISO) system by constructing the embedding coordinate given by Casdagli [35]. Without a loss of generality, the algorithm for SISO system can be extended to multi-input-multi-output (MIMO) system straightforwardly as following.

Consider the system given in (5.2.1), the conditions (5.4.1) to (5.4.2) of the original FNN are then modified as (5.4.5) to (5.4.6) accordingly. Similarly, the optimal combination of n_{dy} and n_{du} is reached when the percentage of FNN becomes sufficiently small.

$$\sqrt{\frac{R_{N_d+1,k}^2 - R_{N_d,k}^2}{R_{N_d,k}^2}} \le R_{tol}, \quad N_d = (n_{dy}, n_{du}) \tag{5.4.5}$$

$$\frac{R_{N_d+1,k}}{R_A} \le A_{tol} \tag{5.4.6}$$

where

$$R_{N_d,k} = \left\| \zeta_{N_d,k} - \zeta_{N_d,k}^r \right\|_2 \tag{5.4.7}$$

$$R_{N_d+1,k}^2 = R_{N_d,k}^2 + \left\| (y,u)_{k+N_d} - (y,u)_{k+N_d}^r \right\|^2 \tag{5.4.8}$$

$$\zeta_{N_d,k} = \left[y_k^T, y_{k+1}^T, ..., y_{k+n_{dy}}^T, u_k^T, u_{k+1}^T, ..., u_{k+n_{du}}^T \right]^T \tag{5.4.9}$$

where $(\cdot)_{k,N_d}^r$ is the point such that $\zeta_{N_d,k}^r$ is the nearest neighbor of $\zeta_{N_d,k}$, n_{dy} and n_{du} are the embedding dimensions of output and input respectively. Similarly, this extended FNN can also be summarized in this flowchart,

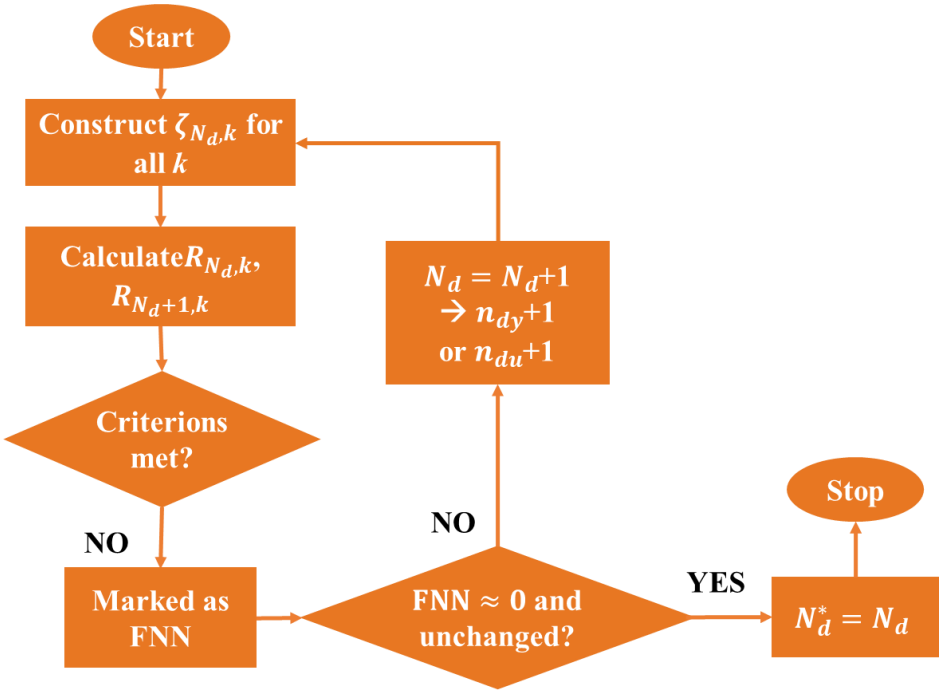

Figure 5.16 Flowchart of FNN for input-output system

5.4.3 *Cao*'s method – Averaged false nearest neighbors

There is a prerequisite for the application of both FNN and the extended FNN; a decision is needed to be made for the values of the threshold constants. These values determine the ratio of the false neighbors. Subjective choice of the threshold parameters leads to different embedding dimension. Therefore, choosing the appropriate values is extremely important. The optimal choice of the parameters will depend on the targeted systems [82]. However, how can we determine the parameters when the system dynamics is unknown? A modified method referred to as averaged false nearest neighbors was introduced by Cao to avoid this problem [36]. Instead of introducing the threshold constants to determine if the nearest neighbor of each point is true or false, Cao's algorithm compute the change of average distances between any individual point and its nearest neighbor after increasing embedding dimension.

First, we consider the autonomous system with the reconstructed delay coordinate $\zeta_{n_d,k}$ in the n_d -dimensional embedding space and define [1]

[1] Note that, if the denominator is zero, we take the second nearest neighbor instead of it.

$$a_{n_d,k} = \frac{\left\| \zeta_{n_d+1,k} - \zeta^r_{n_d+1,k} \right\|}{\left\| \zeta_{n_d,k} - \zeta^r_{n_d,k} \right\|}, k = 1,..., K - n_d \tag{5.4.10}$$

where $R_{n_d,k}$ is defined in (5.4.3). For fast computation purpose, $R_{n_d,k}$ can be calculated as the maximum norm rather than the Euclidean distance. Then we define a new quantify

$$E_1(n_d) = E(n_d + 1) / E(n_d) \tag{5.4.11}$$

where $E(n_d)$ is the mean of all $a_{n_d,k}$ defined by

$$E(n_d) = \frac{1}{K - n_d} \sum_{k=1}^{K-n_d} a_{n_d,k} \tag{5.4.12}$$

When n_d reaches its optimal, $E_1(n_d)$ will stop changing. Similar to the second criterion used against the noise signals in FNN, Cao also introduced another quantity to differentiate the deterministic signals from stochastic signals as

$$E_2(n_d) = E^*(n_d + 1) / E^*(n_d) \tag{5.4.13}$$

where $E^*(n_d)$ is the mean value of absolute change of distance between point y_{k+nd} and y^r_{k+nd}. $(\cdot)^r_{k+nd}$ is the point such that $\zeta^r_{n_d,k}$ is the nearest neighbor of $\zeta_{n_d,k}$.

$$E^*(n_d) = \frac{1}{K - n_d} \sum_{k=1}^{K-n_d} \left| y_{k+nd} - y^r_{k+nd} \right| \tag{5.4.14}$$

Based on [36], $E_2(n_d)$ should be equal to 1 for any embedding dimension for stochastic data because the future dynamics of the system is independent of its past . However, for deterministic system, there exists some n_d's such that $E_2(n_d)$ is not equal to 1. Therefore, we can obtain the optimal embedding dimension as well as distinguish the deterministic signals from the noise by computing $E_1(n_d)$ along with $E_2(n_d)$. The following diagram provides the procedure for this algorithm.

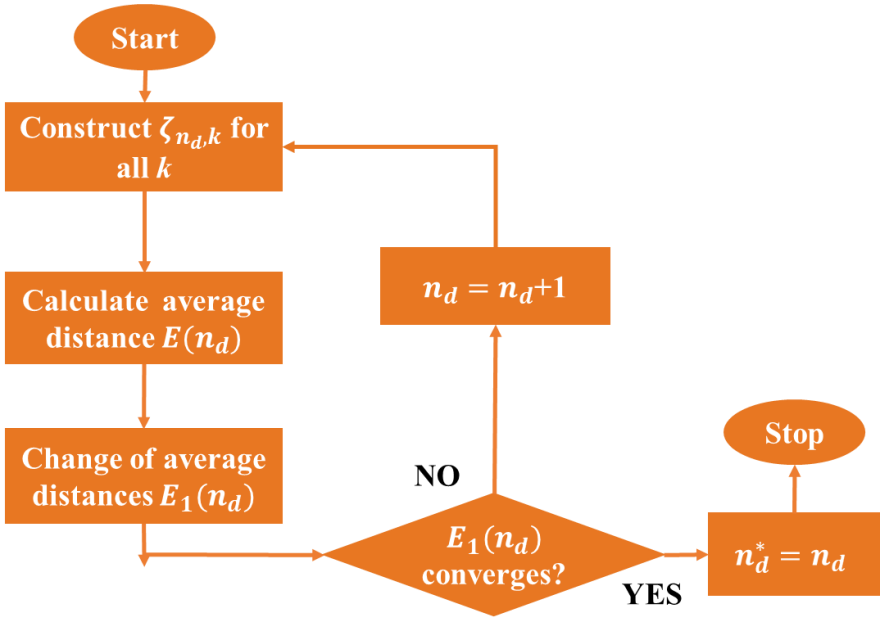

Figure 5.17 Flowchart of Cao's method

Use the same Lorenz system in Section 5.3.1 as an example. The results are shown in Figure 5.18. The E2 curve indicates that the tested data is not random (noise). E1 curve shows that the minimum number of delayed embedding is 2. Therefore, the dimension of the embedded space is 3. Remember that we also need to include the most current measurement in the embedding coordinate. This result is identical to the one provided in FNN.

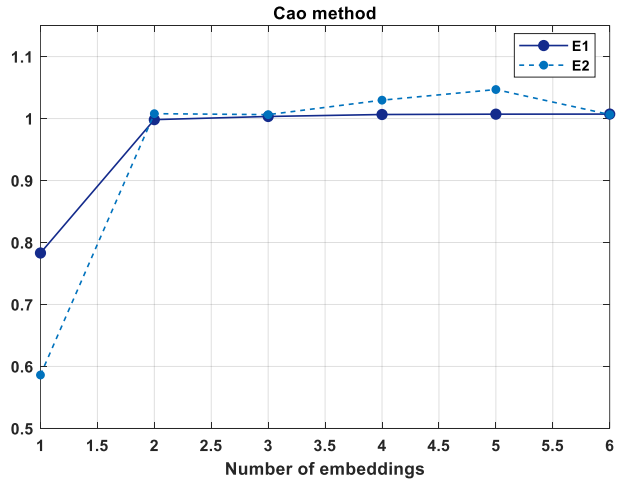

Figure 5.18 Embedding dimension computed by Cao's method

5.4.4 *Cao*'s method for input-output systems

This average FNN algorithm can be also used as a diagnostic to identify the optimal embedding dimension for SISO system [38]. Here, the average FNN is extended to MIMO system defined in (5.2.1) without lossing generality.

Consider the input-output system defined in (5.2.1), $E_1(d)$ and $E_2(d)$ are modified as

$$E_1(N_d) = E(N_d + 1) / E(N_d) \tag{5.4.15}$$

$$E_2(N_d) = E^*(N_d + 1) / E^*(N_d) \tag{5.4.16}$$

where

$$E(N_d) = \frac{1}{K-d} \sum_{k=1}^{K-d} a_{N_d,k}\,, \qquad d = \max(n_{dy}, n_{du}) \tag{5.4.17}$$

$$E^*(N_d) = \frac{1}{K-d} \sum_{k=1}^{K-d} \left\| (y,u)_{k+N_d} - (y,u)^r_{k+N_d} \right\| \tag{5.4.18}$$

$$a_{(n_{dy},n_{du}),k} = \frac{\left\| \zeta_{N_d+1,k} - \zeta^r_{N_d+1,k} \right\|}{\left\| \zeta_{N_d,k} - \zeta^r_{N_d,k} \right\|} \tag{5.4.19}$$

where $R_{N_d,k}$ is defined in Section 5.4.2 in (5.4.7). Similar to $(\cdot)^r_{k+nd}$, $(\cdot)^r_{k+N_d}$ is the point such that $\zeta^r_{N_d,k}$ is the nearest neighbor of $\zeta_{N_d,k}$. Again, this extended Cao's algorithm is concluded in the following diagram.

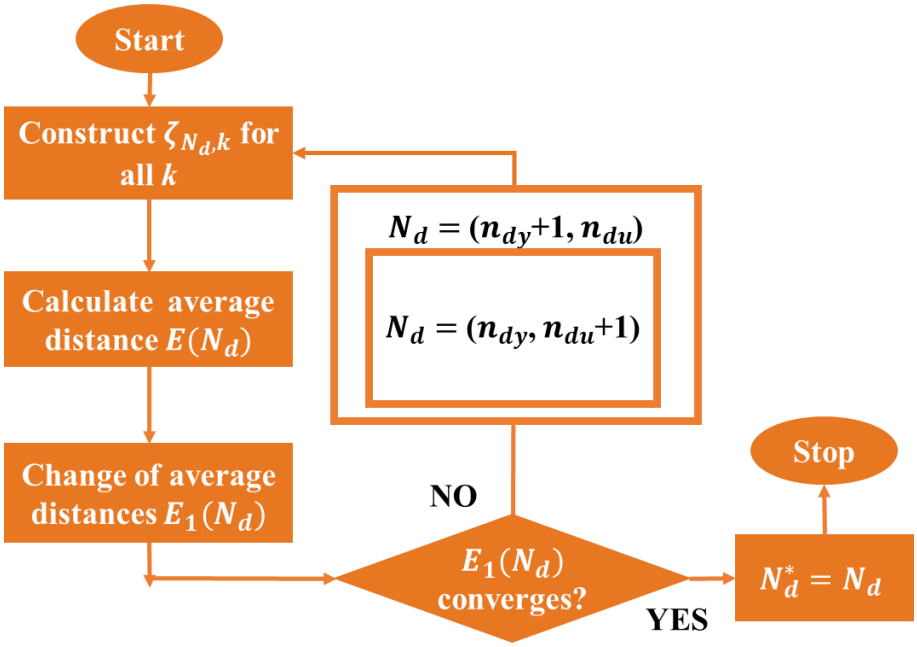

Figure 5.19 Flowchart of Cao's method for input-output system

Chapter 6 Model Predictive Control

Usually, nonlinear system is difficult to control. Fortunately, the proposed methodology in the previous sections transform the original nonlinear system into linear system. This allows us to design the control using the traditional linear algorithms. There are a lot of control techniques we can adopt. However, as stated in the Introduction section, power system control problems are always imposed by different constraints [83], [84].

model predictive control (MPC) is applied to this work because it avoids solving the difficult Hamilton differential equation of the systems with constraints. It aims to solve for the control input at every time step of the closed-loop operation. This is a convex quadratic program (QP) subject to the user-defined constraints and cost function [25]. In this study, the cost function is constructed as

$$\begin{aligned} \min_{u_k} J = & \sum_{k=0}^{N_p-1} (y_k^{ref} - y_k)^T Q (y_k^{ref} - y_k) + u_k^T R u_k \\ s.t. \quad & z_{k+1} = A z_k + B u_k, \ k = 0, ..., N_p \\ & y_k = C z_k \\ & z_0 = g(\zeta_0) \\ & |u_k| \le b_k, k = 0, ..., N_p - 1 \end{aligned} \tag{6.1.1}$$

where Q and R are the real symmetric positive-semidefinite weighting matrices. b_k is the constraint of input. ζ_0 denotes the most recent value for the embedding vector ζ. Since QP problem can be transformed in a dense form the complexity of the problem is shown to be independent of the size of lifting dimension [33]. As a result, a fast computation can be achieved by using QP solvers for linear MPC problem. In this work, qpOASES [88] is utilized as the QP solver. For more information of the Koopman operator-based MPC read references [25], [33].

The frequency and voltage controllers are constructed individually and therefore two cost functions with different variables are needed.

- Frequency control

$$\begin{cases} y_k = frequency \\ u_k = [P_{grid}, \Delta V_{dc}] \end{cases} \tag{6.1.2}$$

- Voltage control

$$\begin{cases} y_k = voltage \\ u_k = Q_{grid} \end{cases} \tag{6.1.3}$$

Finally, the proposed control algorithm can be summarized in the following flowchart diagram.

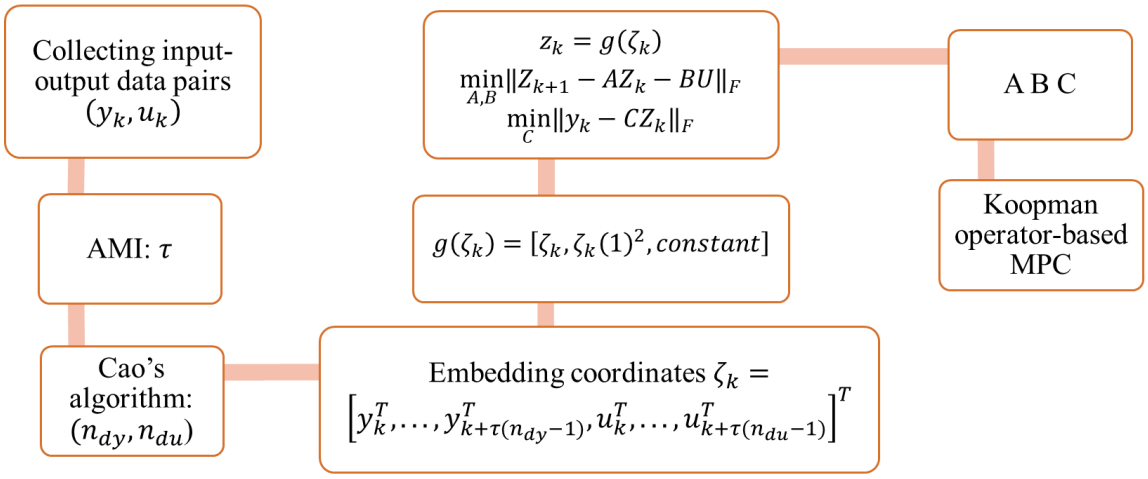

Figure 6.1 Flowchart for the proposed control algorithm

Chapter 7 Case Study and Discussion

In this chapter, two systems will be studied, i.e. Kundur-two area system and IEEE 39-bus system. To enlarge the stability region, many research has been done [84], [85]. In this research, in order to train the controllers to work under larger stability regions, a large numbers of contingencies which contain different loading/generation conditions, different faults with different fault impedances and locations and etc. will be applied randomly.

7.1 Kundur two-area system

The algorithm is firstly tested in the Kundur two-area system which is a sample model of *Matlab/Simulink*. The system diagram is given below. Generator No.3 is decommissioned and replaced with RESs which is represented by negative constant load. The major generator parameters, training parameters and the weighting matrices of KMPC are given in Table 7-1. The size of DC-link capacitor can be found in [18].

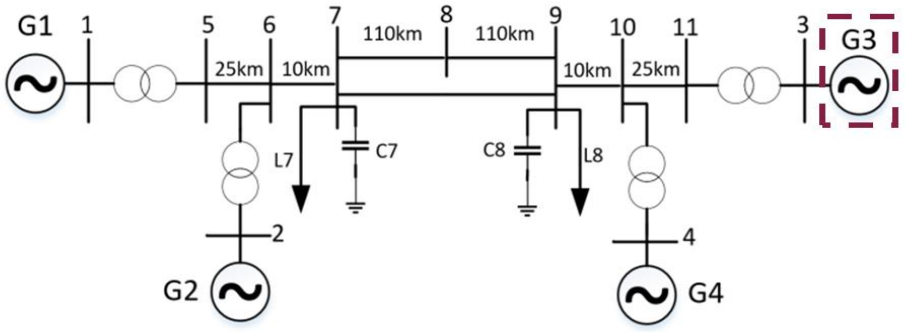

Figure 7.1 Kundur two-area system topology

Table 7-1 Generator and training parameters for Kundur two-area system

Generator No.3 parameters	
Normal power	900MVA
L-L RMS voltage	22kV
Nominal speed ω_0	120π
Rs+jXs	0.0025+j0.25 pu
Inertia coefficient H	6.175s
Training parameters	
Number of trajectories	5000
Sampling time	0.01s for frequency; 0.001s for voltage
Simulation window	5s for frequency; 0.5s for voltage
Range of P	[-0.1, 0.1]
Range of Q	[-0.2, 0.2]
Range of dVdc	[-0.1, 0.1]

KMPC parameters[1]	
Q	Q is chosen such that it only minimizes the norm of the current frequency or voltage
R	[1 0;0 1] for frequency case; 0.5 for voltage case

7.1.1 Time delay estimation for case of frequency control

As explained in section 4.1, the active power and the variation of DC-link voltage are the inputs *u* while the frequency is the output *y* in the frequency control case. The first step of designing the frequency-KMPC is to estimate the optimal time delay. Following the procedure of AMI algorithm given in section 5.3 yields Figure 7.2. As indicated in Figure 7.2, all the three variables cannot reach the threshold *1/e*. Therefore, the first local minimums are chosen as the time delay for the three signals. According to the AMI curves, the resultant time lags for frequency, real power and deviation of DC-link voltage are 9, 5, 5 respectively. Taking average over the three time lags yields $\tau = 6$.

[1] Rules for choosing Q & R: The parameters Q and R can be used as design parameters to penalize the state variables and the control signals. The larger these values are, the more you penalize these signals. Basically, choosing a large value for R means we try to stabilize the system with less (weighted) energy. Since there is a trade-off between the two, Q is kept as I (quasi-identity matrix) and we only alter R. We can choose a large R, if there is a limit on the control output signal, and choose a small R if having a large control signal is not a problem for your system. There are some methods to calculate R such as Searching Techniques. The idea is to look for a value such that it is suitable for most of the cases (likes system parametric changes, different contingencies and so on.). I did not apply this algorithm but I followed the same idea to find the value of R.

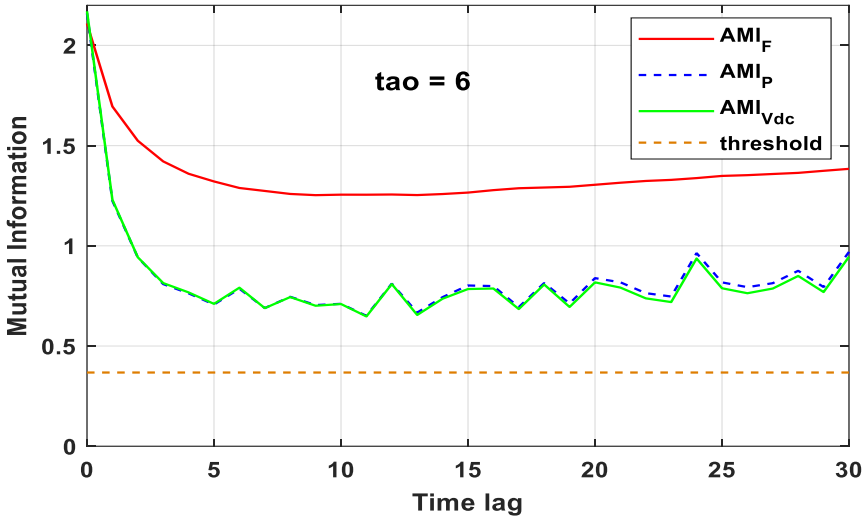

Figure 7.2 AMI of Kundur two-area system frequency case study

7.1.2 Embedding dimension estimation for case of frequency control

Since the optimal τ is 6, 0.06s is adopted as the time lag for the frequency control. Follow the steps of the renewed Cao's method for input-output system in section 5.4.4 we obtain Figure 7.3. The line with white dots is the boundary where indicates the minimum embedding dimensions. Here comes another question, which point laying on the boundary should we pick? This is in fact depending on different considerations. For instance, if the computation time is the most important factor in the study then we pick the point that yields the smallest sum of n_{dy} and n_{du}. From the point of this input-output system, the input and output are of the equal importance. Therefore, the same embedding dimension is chosen for both input and output. The idea is to pick the smallest one among all the combinations of n_{dy} and n_{du} which has the same number of embedding. As a result, $n_{dy} = n_{du} = 8$ is chosen to be the minimum embedding dimension along the boundary line.

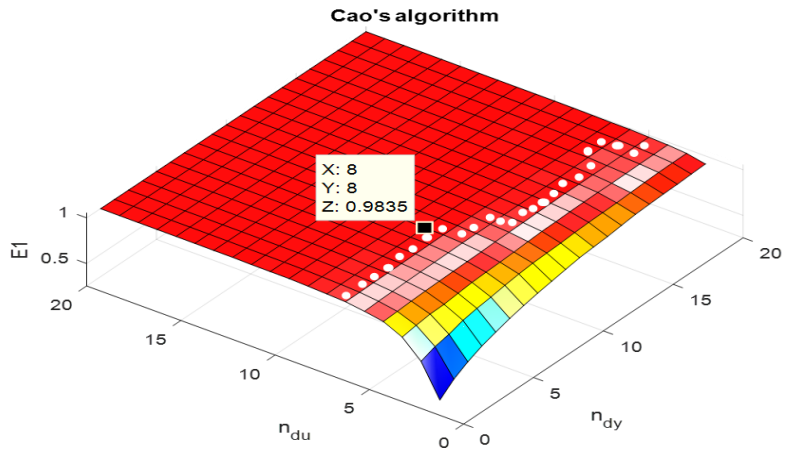

Figure 7.3 Embedding dimension for Kundur two-area system frequency case study

7.1.3 Frequency prediction

To test if the embedding parameters are correct, 200 random trajectories are simulated. The average root mean square error (RMSE) over these 200 trajectories is

$$RMSE = 100 \cdot \frac{\sqrt{\sum_k \left\| x_{pred}(kT_s) - x_{true}(kT_s) \right\|_2^2}}{\sqrt{\sum_k \left\| x_{true}(kT_s) \right\|_2^2}} = 1.54\% \tag{7.1.1}$$

with 4.0s prediction window. As can be seen from one example of the comparison between the prediction and true measurement, the proposed algorithm can achieve a very precise prediction in a relatively long prediction window with a large frequency deviation.

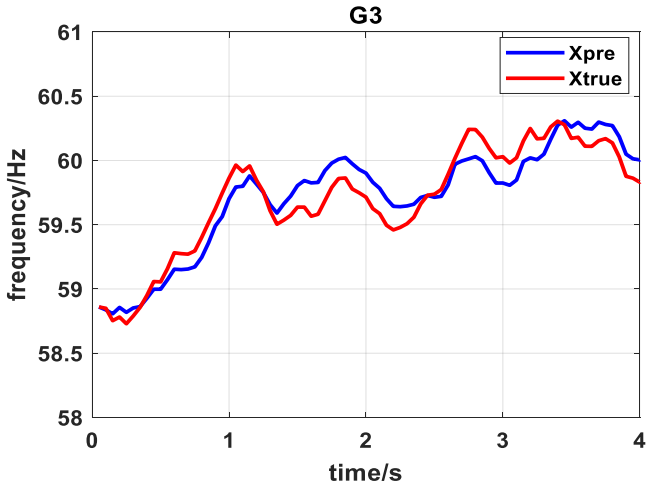

Figure 7.4 Frequency prediction of generator bus 3

7.1.4 Frequency controller performance

The performance of the proposed Koopman operator-based MPC is tested in the three-phase-to-ground fault at bus No.8 at 1s. This fault resulting tripping one of the double line connecting area 1 and 2, it is then reclosed at 6s. The system without KMPC is the original system with generator No.3 replaced by constant negative load while the system with KMPC is the system with generator No.3 replaced by the constant negative load and the proposed DSMS. It can be observed from the transient dynamics that the system with KMPC efficiently damps most of the oscillation while the system without KMPC has much higher magnitude of swings.

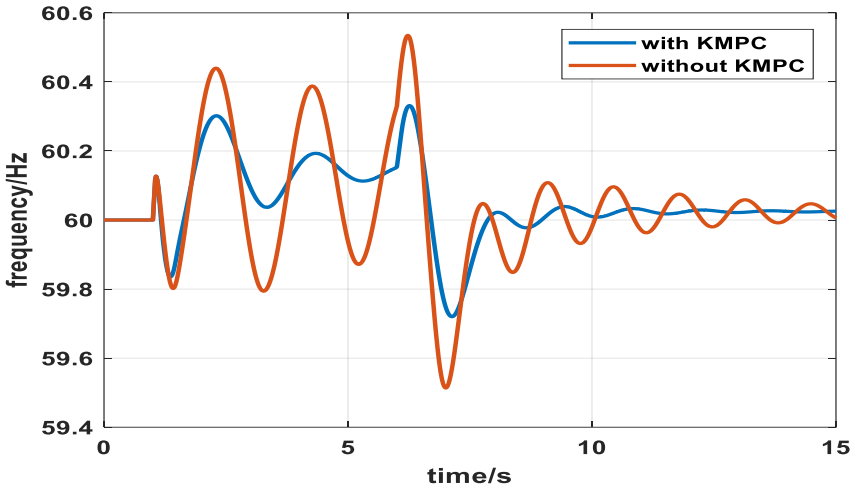

Figure 7.5 Frequency transient responses

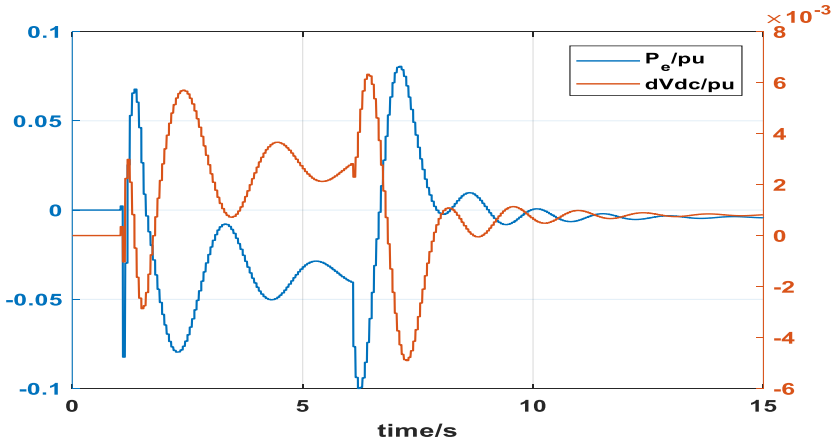

Figure 7.6 Input signals computed by frequency-KMPC

It is worth noting that there are three types of simulation mode in *Simulink*; continuous mode, discrete mode, and phasor mode. The phasor mode uses simplified models allowing fast simulation for very large-scale power grids. On the other hand, the continuous/discrete modes use detailed models based on differential equation solvers to evaluate system transient. Despite the speed advantage, the phasor mode presents limitation in terms of obtaining the local bus frequency because the phase-locked loop (PLL) block[1], given in *Simscape* library and run in continuous/discrete mode, cannot be implemented in the phasor mode. An algorithm referred to as Frequency Divider (FD) is adopted as an alternative in phasor mode simulation to estimate the local bus frequency based on the system topology and generator rotor speeds [90]. The previous frequency controller is built upon FD algorithm. Figure 7.7 compares the frequency responses measured by FD and PLL with low-pass filter while Figure 7.8 shows the control signals computed by KMPC with frequency measured by PLL. As shown in Figure 7.7, the frequency given by PLL has very notable numerical issue, showing large spikes even with the help of low-pass filter. By comparing Figure 7.6 and Figure 7.8, we can find that the control signals given by KMPC have slightly different responses when the numerical spikes appear. However, we can infer from these figures that KMPC can work with either frequency estimation technique under either simulation mode. Therefore, in the following study, the system model will be developed in phasor mode and the frequency will be estimated by FD algorithm.

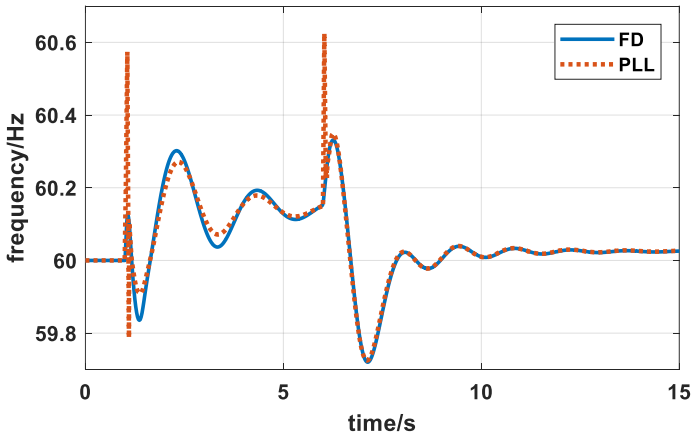

Figure 7.7 Frequency responses in the case of FD and PLL

[1] Phasor measurement unit (PMU) is used to measure frequency in power utilizes [86], [87] which can be found in the newer version of *Simulink.*

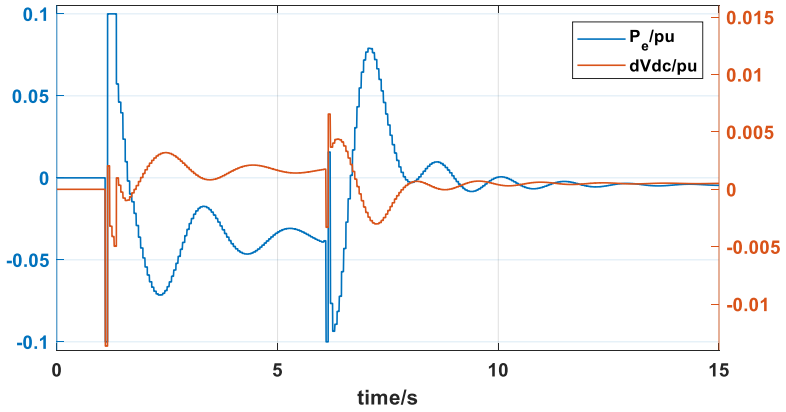

Figure 7.8 Control signals computed by KMPC with frequency measured by PLL

7.1.5 Time delay estimation for voltage control

The terminal bus voltage is regulated via the reactive power of DSMS. Therefore, the input *u* is the reactive power and output *y* is local bus voltage. As shown in Table 7.1, the sampling time of voltage control case is 0.001. After applying AMI the mutual information of voltage and reactive power versa time lag is given in the following figure.

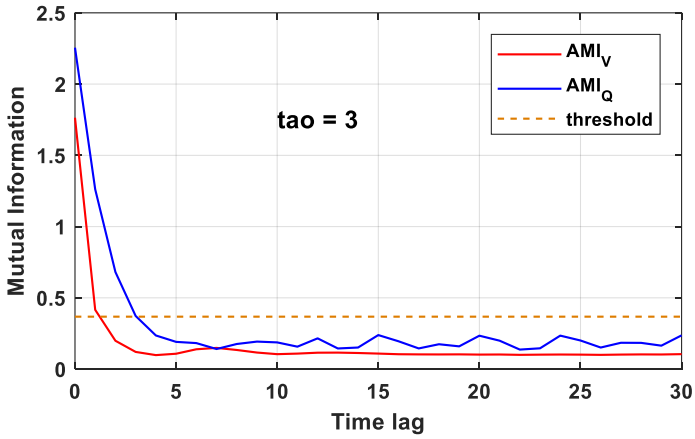

Figure 7.9 AMI of Kundur two-area system voltage case study

Unlike the frequency control case, the AMI of reactive power and voltage drop below the threshold *1/e*. As a result, the time lags for V and Q are 2 and 4 respectively which leads to the average AMI of 3.

7.1.6 Embedding dimension for case of voltage control

The resultant $\tau = 3$ leads to 0.003 time lag for the voltage control. Using this time lag and Cao's method, the embedding dimensions of voltage and reactive power are given in the 3-D surface below. Similar to the strategy used in frequency control case, the same embedding dimension of Q and V are adopted. The smallest number 11 of all the combinations which have the same number of n_{dy} and n_{du} is chosen to be the minimum embedding dimension.

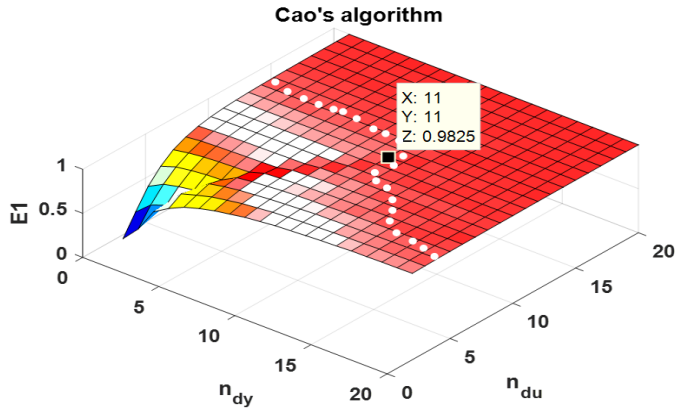

Figure 7.10 Embedding dimension for Kundur two-area system voltage case study

7.1.7 Voltage prediction

A shorter voltage prediction window (0.3s) is utilized because the voltage reacts much faster than grid frequency. In addition, the main purpose of the voltage controller is to improve the voltage performance during faults such as voltage sag problem caused by short circuit. To showcase the predictor performance, an example is also given in Figure 7.9.

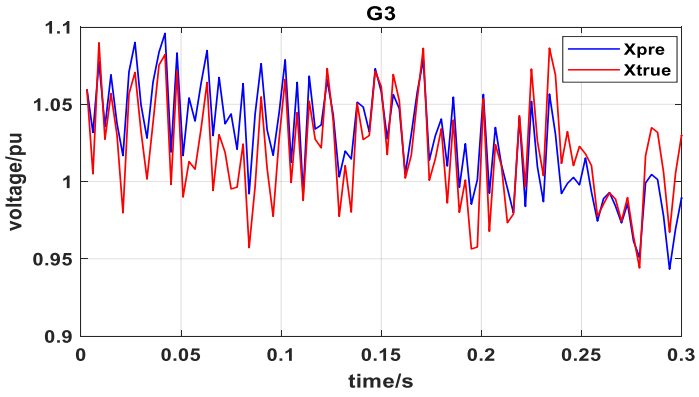

Figure 7.11 Voltage prediction of generator bus 3

Based on the figure, we can find that the predicted voltage generally follows the trace of the true voltage measurement. However, due to the sensitivity and the fast dynamics of voltage, the prediction error RMSE which is 8.8% over 200 random trajectories is a bit bigger than the frequency case. But this error is still a satisfactory result and it is sufficiently small for the purpose of control. This will be shown in next section.

7.1.8 Voltage controller performance

Under the same event and same system settings as the frequency case, apparently, the system with voltage-KMPC has less oscillation. In order to show more details during voltage dip, an enlarged plot is also given. As expected, with KMPC, the voltage dip during fault is reduced by 0.3 pu.

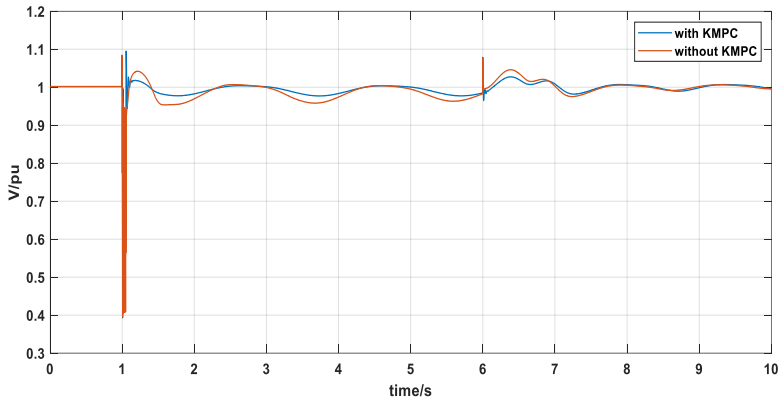

Figure 7.12 Voltage performance

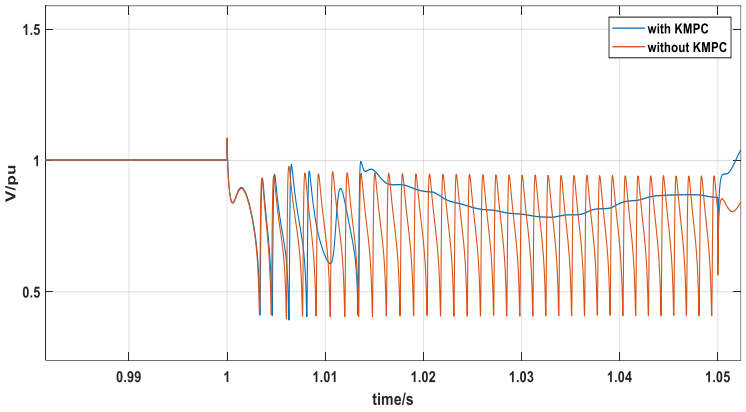

Figure 7.13 Voltage performance during fault

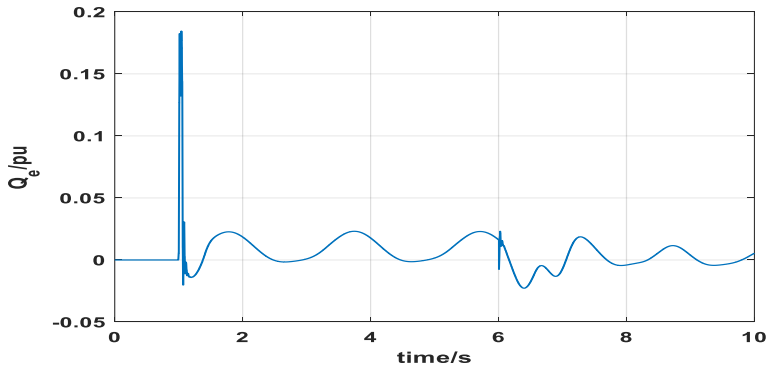

Figure 7.14 Input signals computed by voltage-KMPC

7.1.9 Critical clearing time study

Now, let us integrate the frequency-KMPC and voltage-KMPC (FV-KMPC). To showcase the beauty of FV-KMPC, severe contingencies are applied to the system. A three-phase-to-ground fault is occurred at bus No.9. As a result, the original system without replacing any generator displays 0.31 critical clearing time (CCT) under this event. At the same time, the system with FV-KMPC shows a higher CCT 0.36s. Figure 7.13 to 7.16 provide the transient performances of rotor angles and rotor angular speed of the FV-KMPC system and the original Kundur two-area system. FV-KMPC system regain steady-state in about 6s while the original system diverges in 1.5s.

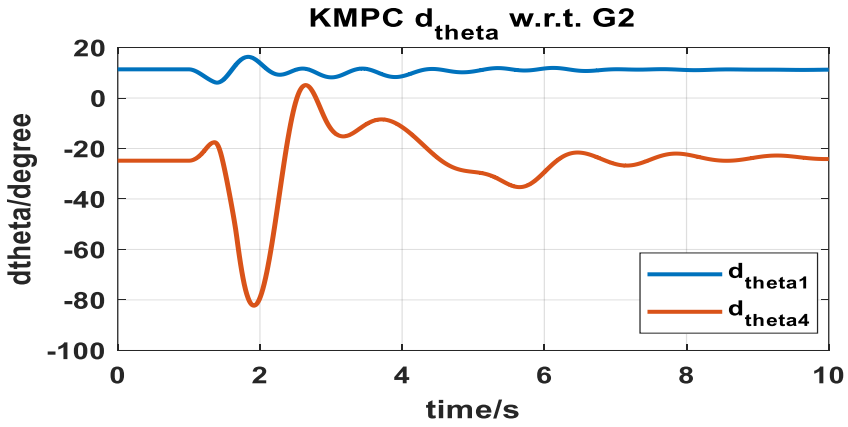

Figure 7.15 Rotor angles of generator 1 & 4 w.r.t. generator 2 of FV-KMPC system[1]

[1] Note that generator 3 is replaced with negative constant load and DSMS so its rotor angle and speed are not presented.

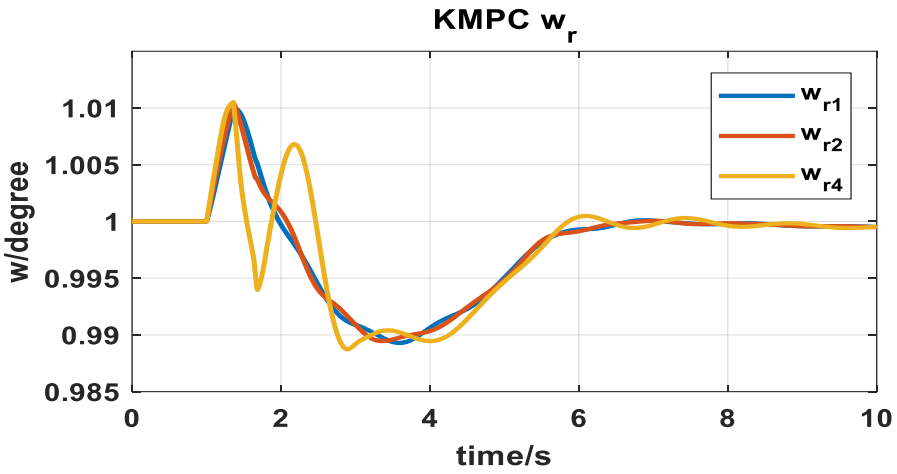

Figure 7.16 Rotor speeds of generator 1 & 4 of FV-KMPC system

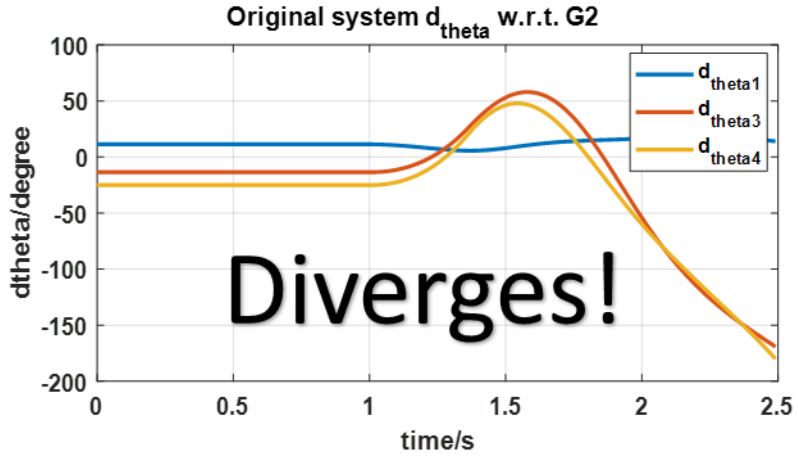

Figure 7.17 Rotor angles of generator 1, 3 & 4 w.r.t. generator 2 of original system

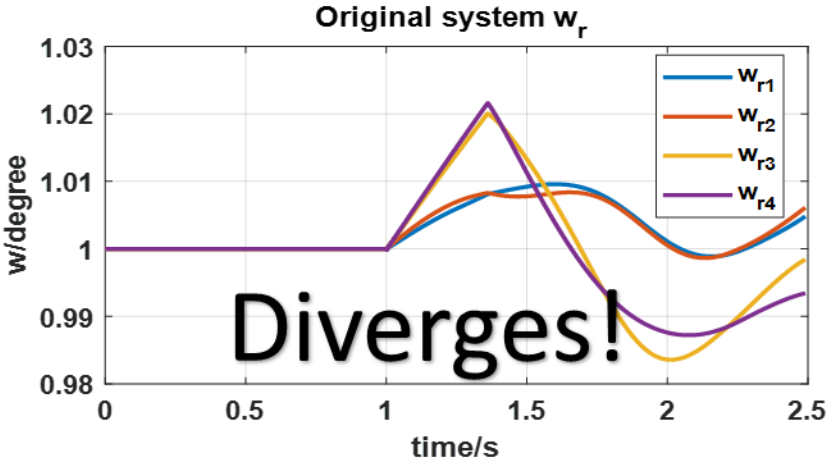

Figure 7.18 Rotor speeds of generator 1~4 of original system

7.1.10 Robustness study

To test the robustness of the proposed controller, several modifications of the system topologies have been applied. The first modification is load at bus 7 which is changed to 75% of its original value. The controller efficiently damps the oscillation and thereby improve the transient performance after the same three-phase bus fault studied in section 7.1.4. The second modification is that the generation of generator No.7 is reduced to 70% of its original. Again, the controller damps most of the oscillations. At last, different line impedances of the double lines are applied to study KMPC's robustness. As indicated from the Figure 7.17 to 7.19, KMPC is always able to do their jobs even the system topology encounters critical changes (the change of transmission line connecting area 1 and 2).

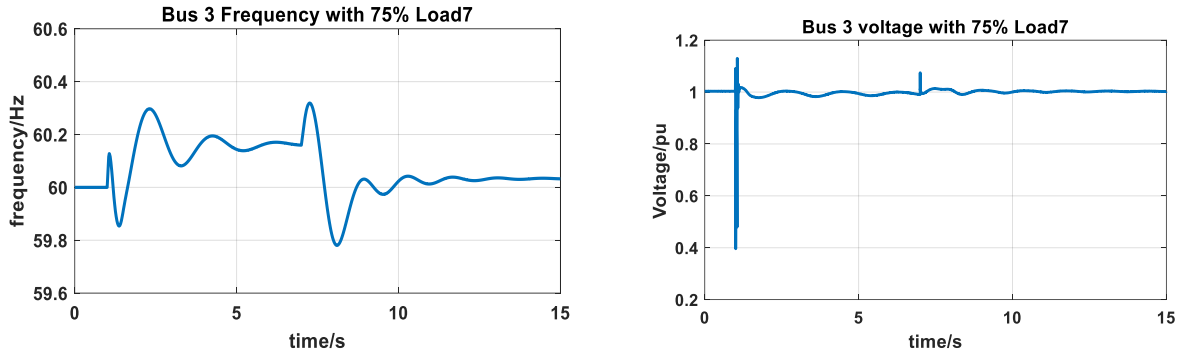

Figure 7.19 Frequency and voltage responses of generator 3 with 75% load at bus 7

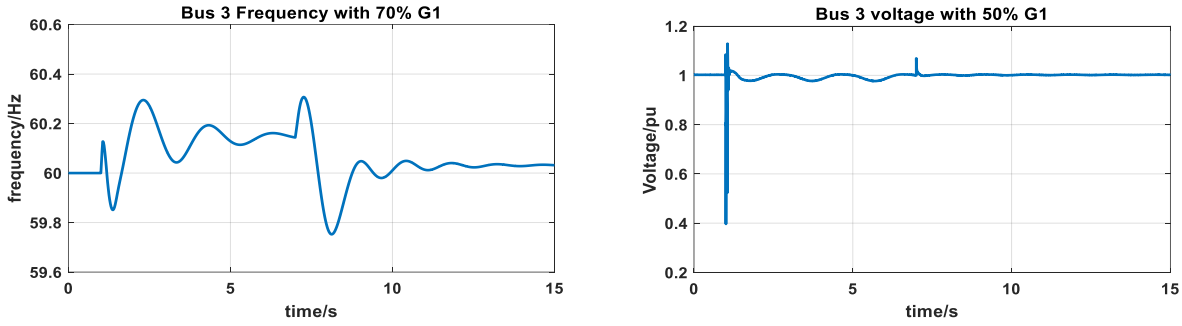

Figure 7.20 Frequency and voltage responses of generator 3 with 70% generation of generator 1

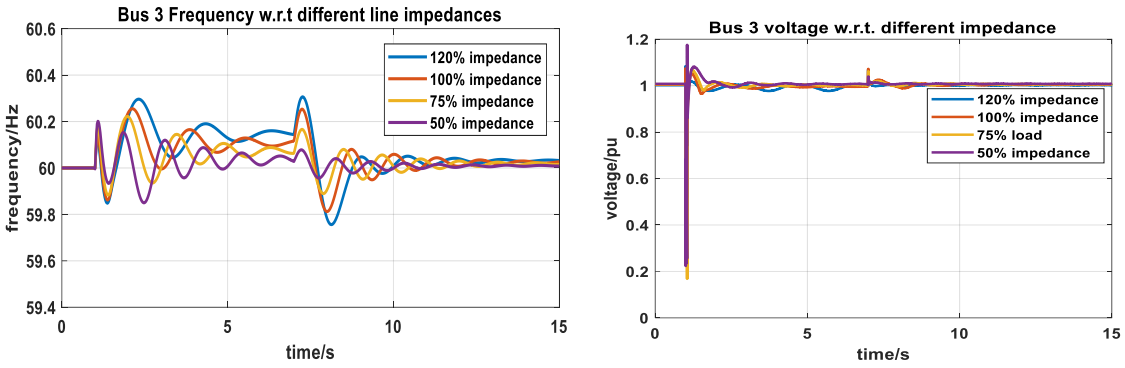

Figure 7.21 Frequency and voltage responses of generator 3 with different double-line impedances

7.2 IEEE 39-bus system

Now, let us study a bigger system with more complicated network. The system model is built in *Matlab/Simulink* which can be found in [89]. The system topology is shown in Figure 7.20. See [18] for the size of the DC-link capacitor. Generator No.10 is replaced by RESs (negative constant load) and the proposed system DSMS. Similar to the Kundur two-area case study, the data is collected from different contingencies. The main generator parameters, training parameters and the weighting matrices of KMPC are given in Table 7-2.

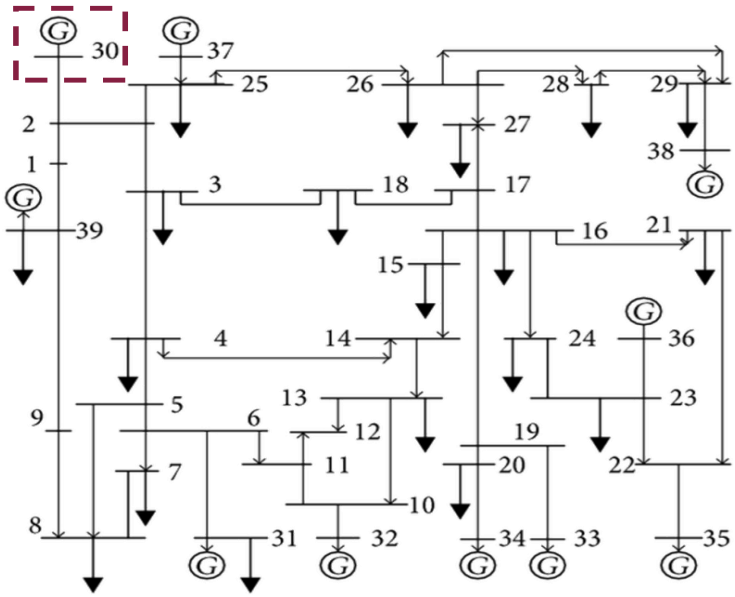

Figure 7.22 IEEE 39-bus system topology

Table 7-2 Generator and training parameters of IEEE 39-bus system

Generator No.10 parameters	
Normal power	1000MVA
L-L RMS voltage	20kV
Nominal speed ω_0	120π
Rs+jXs	0.0014+j0.31 pu
Inertia coefficient H	4.2s
Training parameters	
Number of trajectories	10000
Sampling time	0.01s for frequency; 0.001s for voltage
Simulation window	5s for frequency; 0.5s for voltage
Range of P	[-0.5, 0.5]
Range of Q	[-0.5, 0.5]
Range of dVdc	[-0.2, 0.2]
KMPC parameters	
Q	Q is chosen such that it only minimizes the norm of the current frequency or voltage
R	[0.02 0;0 0.02] for frequency case; 0.5 for voltage case

7.2.1 Time delay estimation for case of frequency control

Repeat the process I section 7.1, we first calculate time lag. The result is given in Figure 7.21. According to the curves, AMI of the three variables cannot reach the threshold line and thereby the first local minimum is utilized. AMI_F, AMI_p, AMI_{Vdc} are 11, 5, 5 respectively resulting in the average time lag $\tau = 7$.

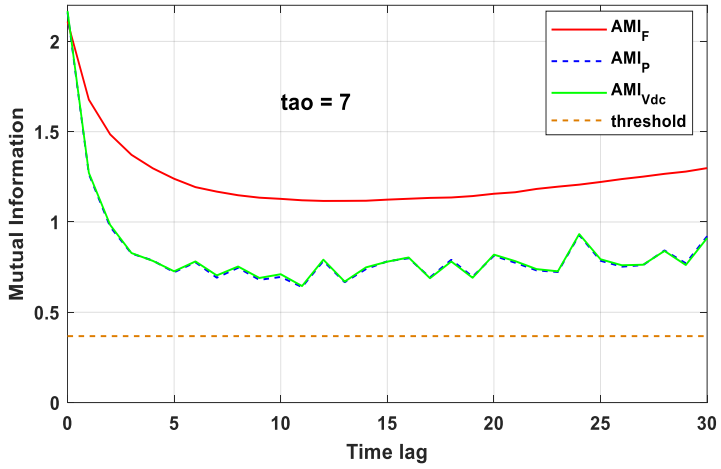

Figure 7.23 AMI of IEEE 39-bus system frequency case study

7.2.2 Embedding dimension estimation for case of frequency control

Adopt $\tau = 7$ to the embedding vector and apply the modified Cao's method yields Figure 7.22.

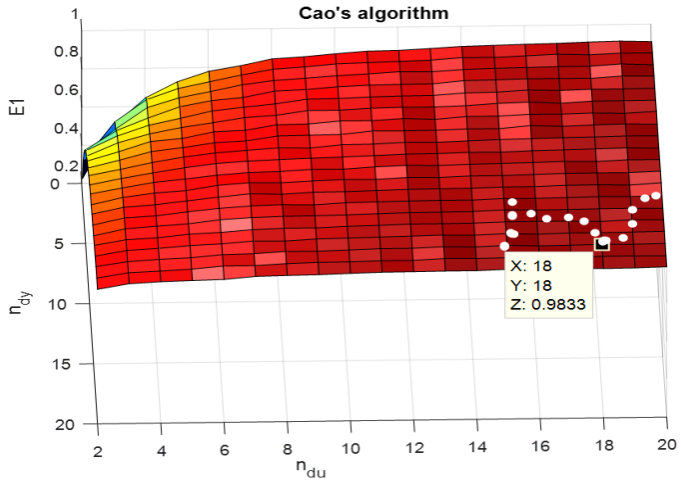

Figure 7.24 Embedding dimension for IEEE 39-bus system frequency case study

Follow the same rule in the previous case study, the minimum embedding dimension is $n_{dy} = n_{du} = 18$. This embedding dimension is larger than the one obtained in the Kundur two-area system. That is because the IEEE 39-bus system has more equipment than the Kundur system and thereby IEEE 39-bus system has more states than the Kundur system. However, the embedding dimension may not simply increase proportionally with the size of the system states. When we train the system, different contingencies and different levels of control inputs are applied. The effected states are unknown since those events occur randomly. If those events we use to train the controller are closed to the replaced generator, the states locate in other parts of the system may not be energized meaning that those states are not participating in the studied system dynamics.

7.2.3 Frequency prediction

The Koopman predictor is once again tested over 200 random trajectories from different events. The average RMSE is 1.7% with 4s prediction window. One prediction example is shown in the figure below.

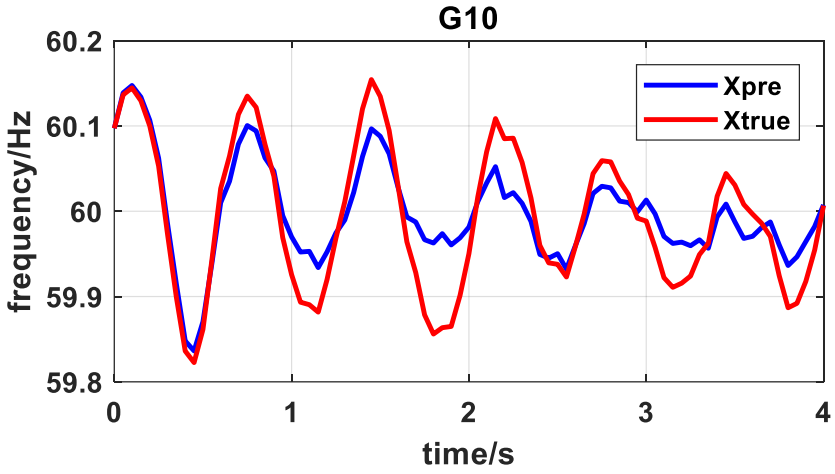

Figure 7.25 Frequency prediction of generator bus 10

7.2.4 Frequency controller performance

The performance of the proposed Koopman operator-based MPC is tested in the three-phase-to-ground fault at bus No.25 at 1s resulting tripping line connecting between bus 25 and 26 after three cycles. The system without KMPC is the original system with generator No.10 replaced by constant negative load while the system with KMPC is the system with generator No.10 replaced

by the constant negative load and the proposed DSMS. KMPC system efficiently damps most of the oscillation while the system without KMPC has much bigger swings.

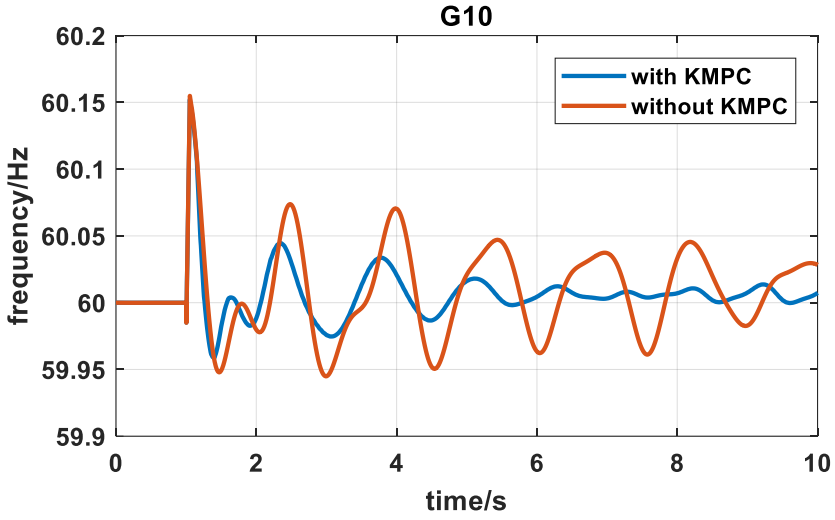

Figure 7.26 Frequency transient responses

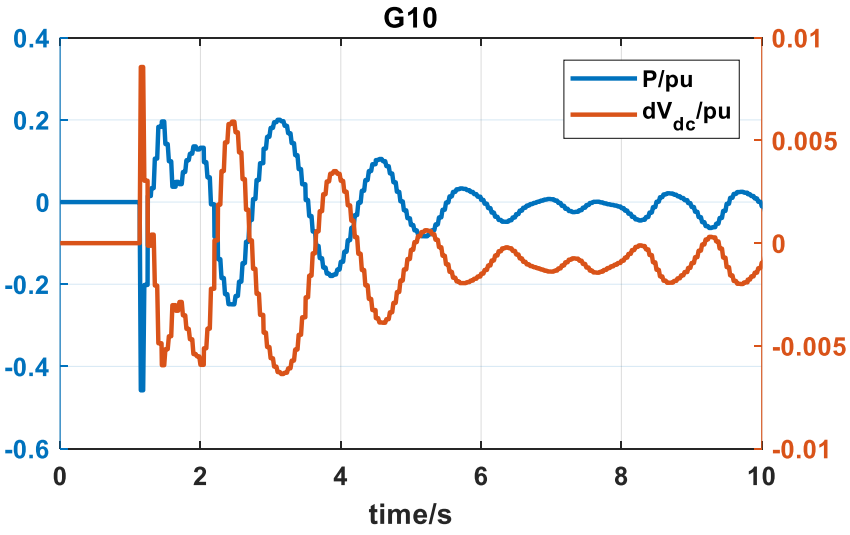

Figure 7.27 Input signals computed by frequency-KMPC

7.2.5 Time delay estimation for voltage control

The result of the time lag of the voltage control is $\tau = 4$ with 0.001 sampling time. Therefore, the time delay is 0.004s.

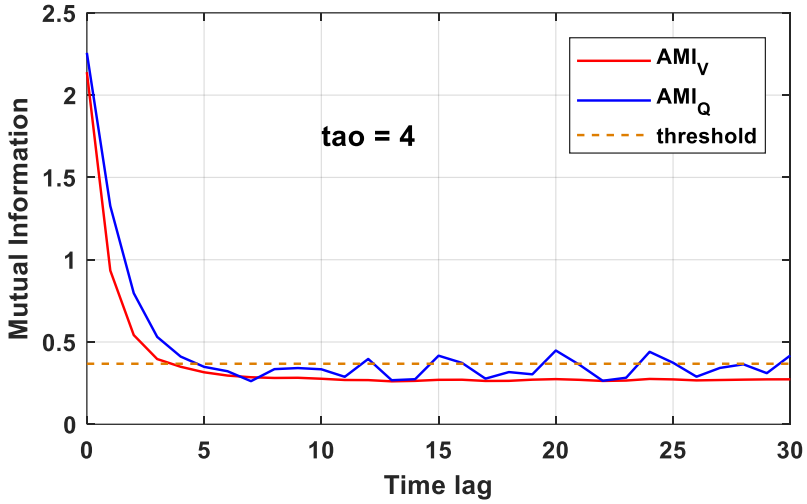

Figure 7.28 AMI of IEEE 39-bus system voltage case study

7.2.6 Embedding dimension for case of voltage control

The modified Cao's method generates the following 3-D plot which indicates $n_{dy} = n_{du} = 19$.

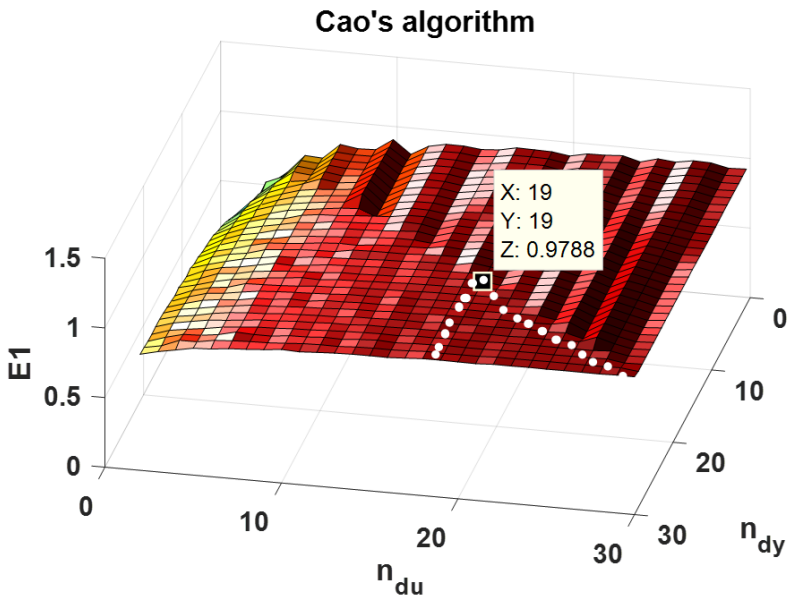

Figure 7.29 Embedding dimension for IEEE 39-bus system voltage case study

7.2.7 Voltage prediction

A 0.3s prediction window is applied for voltage prediction. The average RMSE over 200 trajectories is 9.9%.

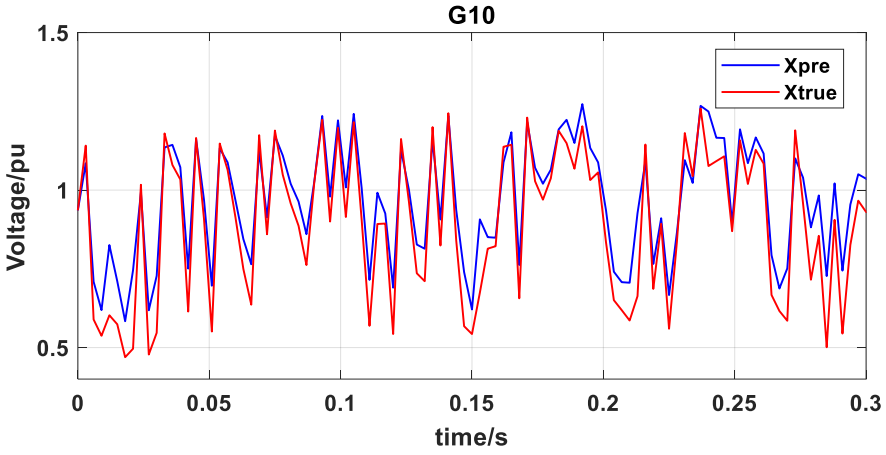

Figure 7.30 Voltage prediction of generator bus 10

7.2.8 Voltage controller performance

To study voltage-KMPC, the same fault and same system settings as the frequency case is applied. Once again, with KMPC, the voltage sag during fault is reduced by 0.25 pu as expected.

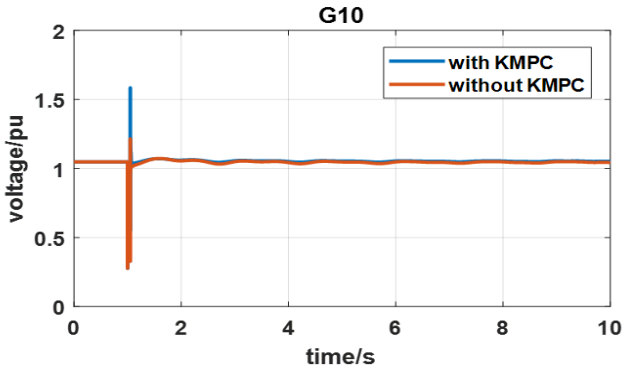

Figure 7.31 Voltage performance

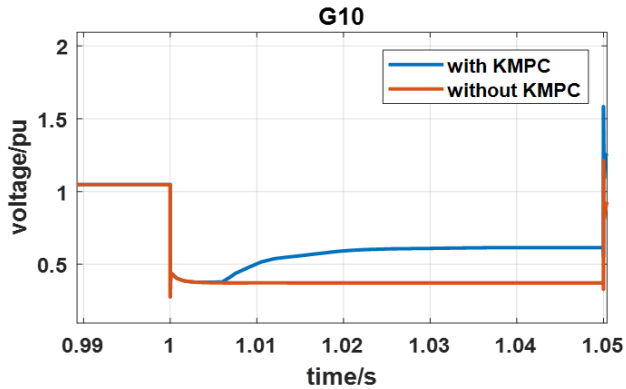

Figure 7.32 Voltage performance during fault

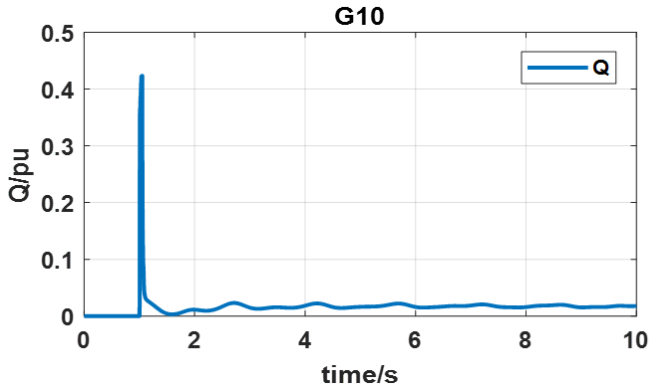

Figure 7.33 Input signals computed by voltage-KMPC

7.2.9 Critical clearing time study

Now, let us also apply FV-KMPC to the system with severe contingencies. A three-phase fault is occurred at bus 25. The original system has 0.20s CCT whilst the FV-KMPC system can return to the steady-state after 0.24s. So the CCT is increased by approximately 2 cycles.

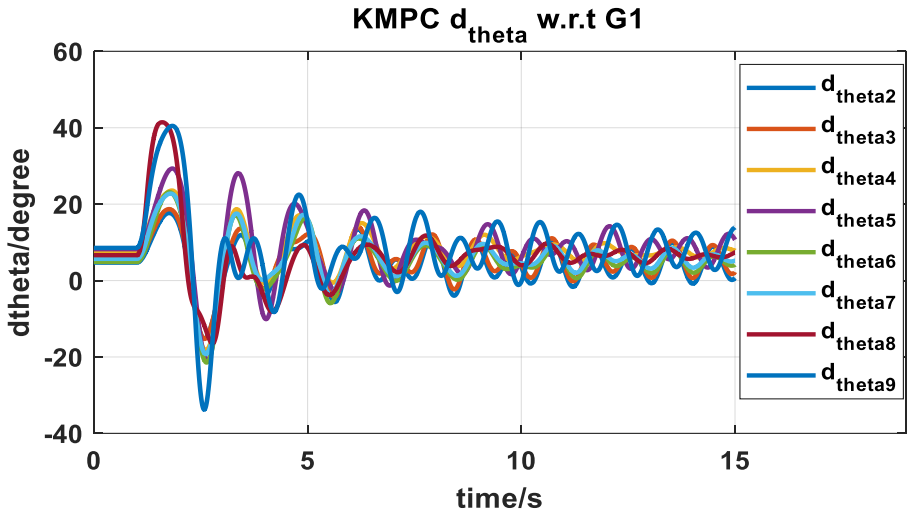

Figure 7.34 Rotor angles of generator 2 ~9 w.r.t. generator 1 of FV-KMPC system[1]

[1] Note that generator 3 is replaced with negative constant load and DSMS so its rotor angle and speed are not presented.

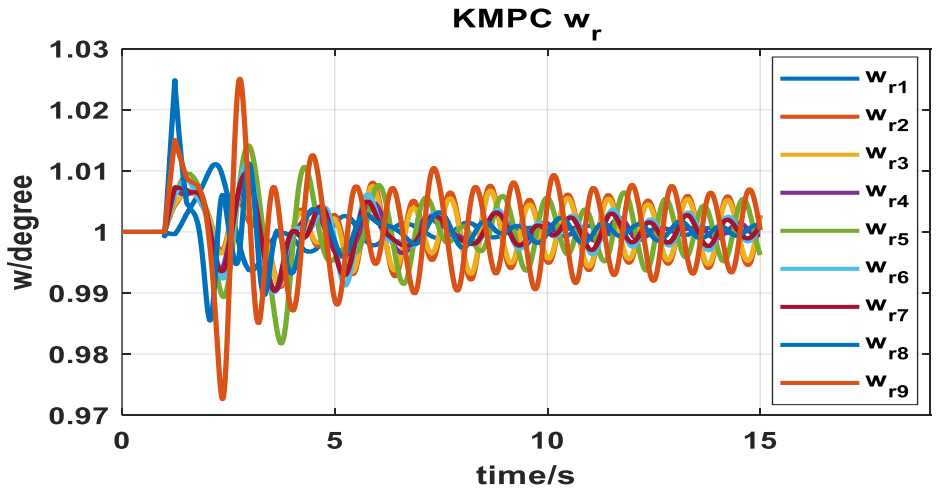

Figure 7.35 Rotor speeds of generator 1 ~ 9 of FV-KMPC system

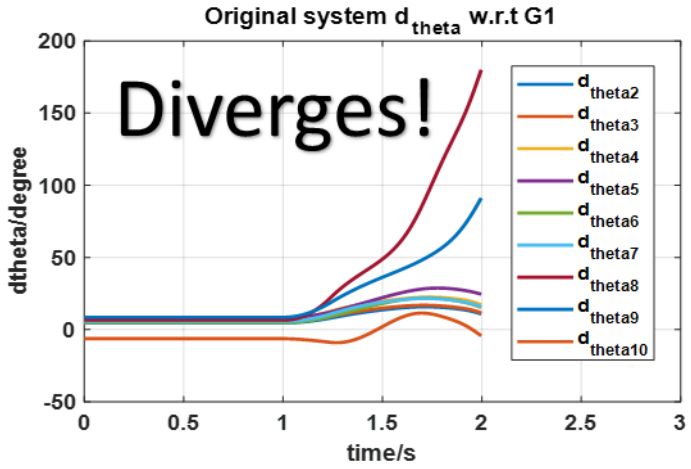

Figure 7.36 Rotor angles of generator 2 ~ 10 w.r.t. generator 1 of original system

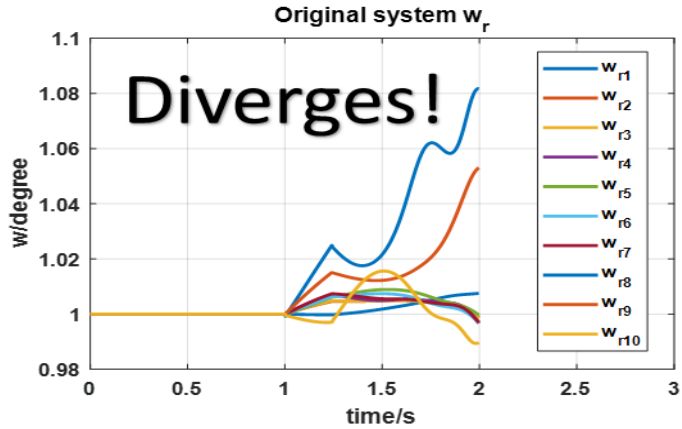

Figure 7.37 Rotor speeds of generator 1 ~ 10 of original system

7.2.10 Robustness study

To study the controllers' robustness, firstly, we pick the first two largest loads which are at bus 39 (over 1000MW) and bus 20 (over 600MW) respectively. In the first case, the load at bus 39 is reduced to 50%. The second case is the load at bus 20 is double on the top of the load modification of bus 39. In order to study the robustness against transmission line changes, we first need to find the 'important' line of the system. According to the load flow study, modifying the line impedance between bus 21 and 22 results in 60% change of load flow which is the largest change among the non-transformer branches. So in the third case study, a 5-time line impedance of the original one is applied on the top of the previous two changes. The results of these three case studies are given in Figure 7.36 to 7.38. The controllers perform perfectly against those topology changes.

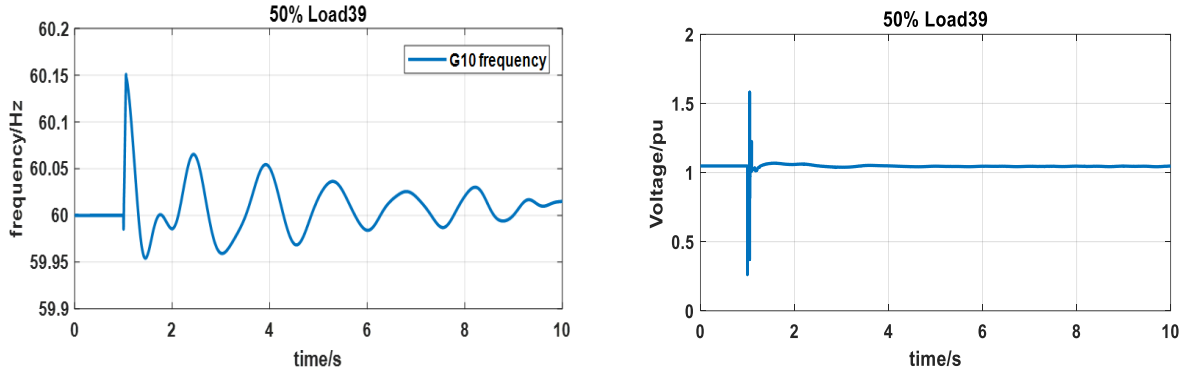

Figure 7.38 Frequency and voltage responses of generator 10 with V-

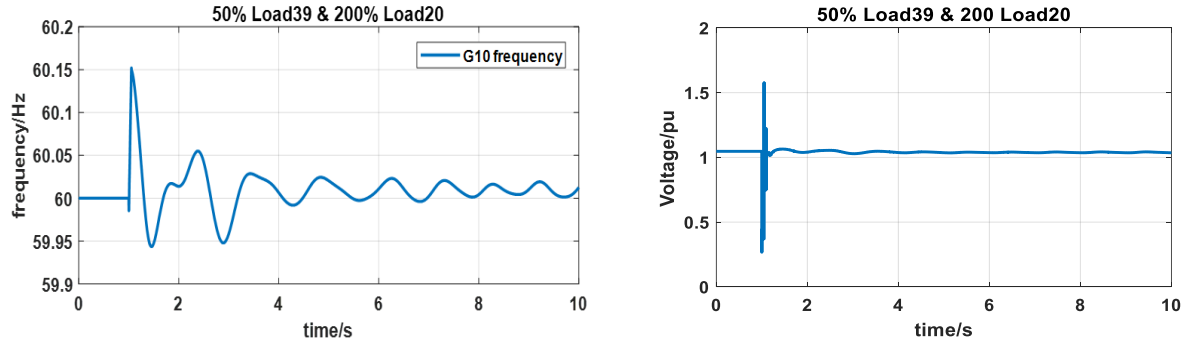

Figure 7.39 Frequency and voltage responses of generator 10 with 50% load at bus 39 & 200% load at bus 20

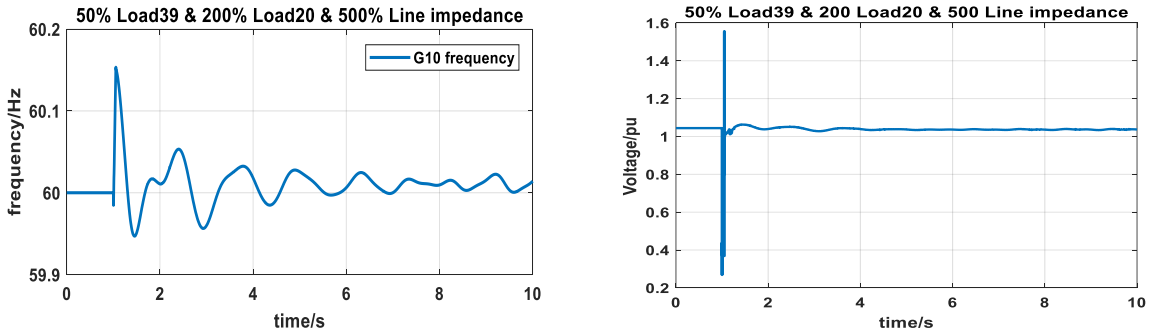

Figure 7.40 Frequency and voltage responses of generator 10 with 50% load at bus 39 & 200% load at bus 20 & 500% line impedance

7.3 Multi-machine system

So far we have studies the system with one generator replaced by DSMS. What if there are two DSMS located in different areas? Will they fight with each other during frequency transient? Kundur two-area system is a perfect system for this purpose of study. Generator 1 and 3 are replaced by DSMS and RESs.

7.3.1 System with KMPC v.s. system without KMPC

The line connecting bus 7 and 9 is open at 1s and reclosed at 5s. According to Figure 7.40, the system with KMPC apparently damp the frequency oscillation and return to steady-state at 7s. Meanwhile, the system without KMPC has more than 5 times magnitude of oscillation and it still oscillates at 15s. In terms of voltage, the system with KMPC quickly resumes steady-state while the system without KMPC has significant oscillations.

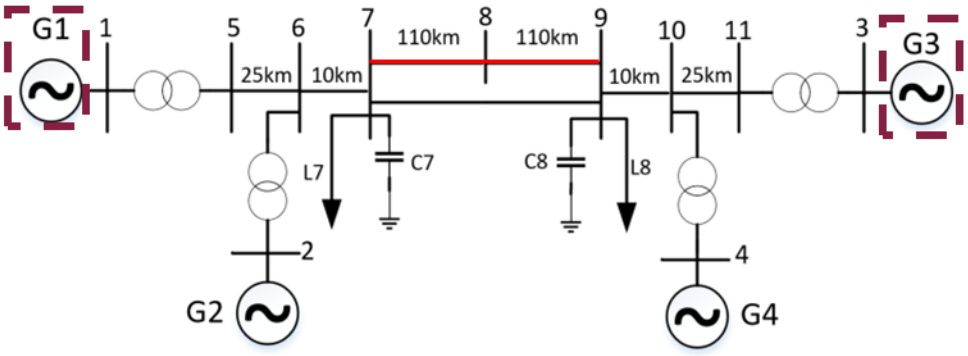

Figure 7.41 Kundur two-area system with two generator replaced

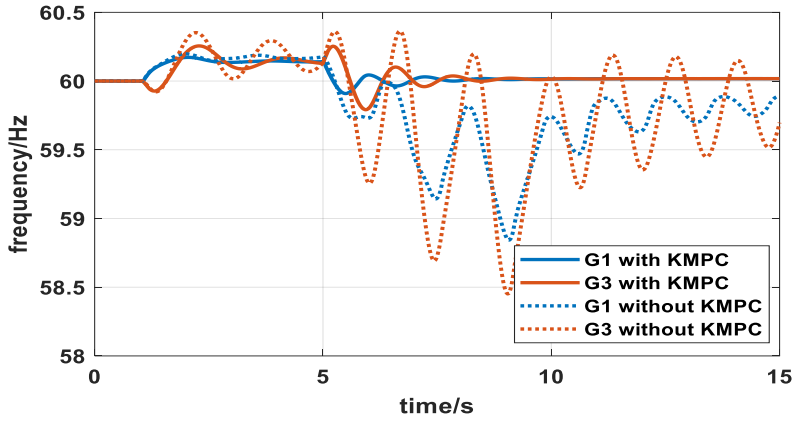

Figure 7.42 Frequency responses of multi-machine case

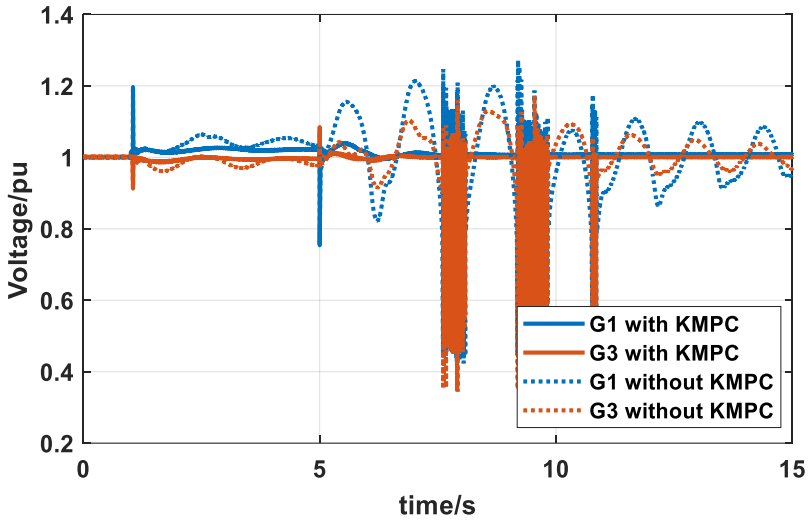

Figure 7.43 Voltage responses of multi-machine case

7.3.2 System with KMPC v.s. original system

To further showcase the advantages of the proposed KMPC, the same scenario given in section 7.1.9 is applied. Again, the original system has 0.31 CCT. However, the CCT is increased to 0.48s in the system with two KMPC as can be seen from the following figures. With 0.48 clearing time, the original system diverges faster (at 2.3s) than the CCT study of single KMPC in section 7.1.9.

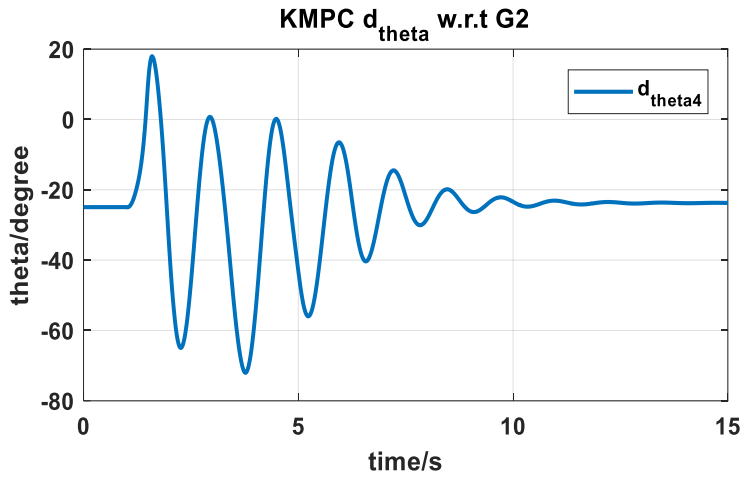

Figure 7.44 Rotor angles of generator 4 w.r.t. generator 2 of two KMPC system

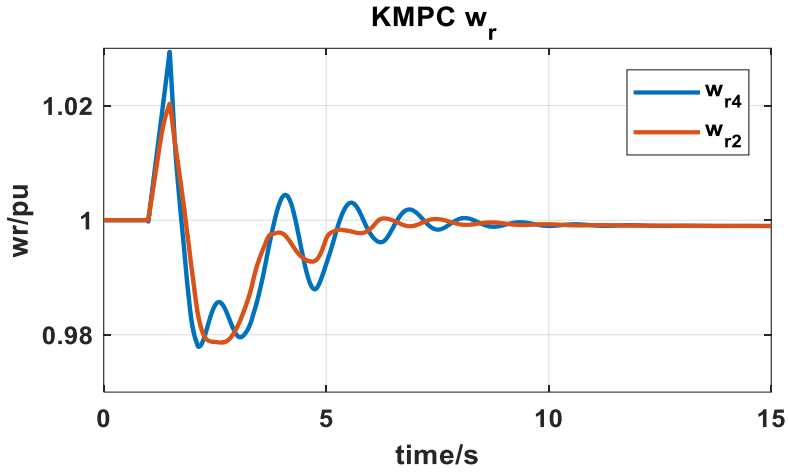

Figure 7.45 Rotor speed of generator 2 & 4 of two KMPC system

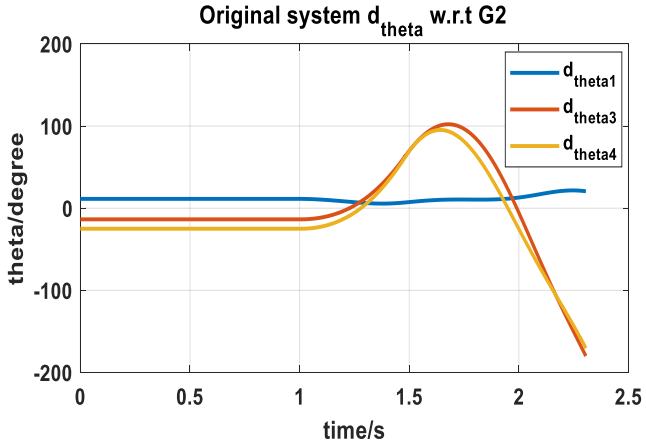

Figure 7.46 Rotor angles of generator 1, 3 & 4 w.r.t. generator 2 of original system

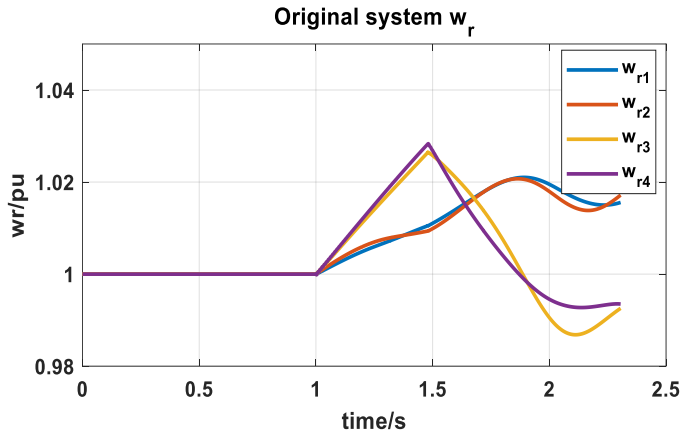

Figure 7.47 Rotor speeds of generator 1~ 4 of original system

Chapter 8 Conclusions and Outlook

8.1 Conclusions

- The DSMS device which consists of the converter-based system and a retired synchronous generator with no governor is proposed to eliminate the frequency oscillation by means of regulating active power output, deviation of DC-link voltage. Besides, it is also able to provide auxiliary voltage support via altering reactive power output. Therefore, it is capable of preventing losing step due to RESs penetration during large disturbances.
- A model-free, purely data-driven Koopman operator-based control framework involves transforming the original highly nonlinear system into a linear system is proposed. Due to its model-free nature, the proposed algorithm can be applied to but not limited to the power system utilities control equipment such as FACTs devices, battery systems and so on using only the field data. The proposed algorithm can also be applied to the nonlinear system dynamics prediction. This is extremely helpful especially for the large-scale power systems whose mathematical models are unobtainable.
- In order to unfold the nonlinear system dynamics, the choice of Koopman observable functions (lifting functions) is critical. The time-delay embedding technique has been widely used in system identification which makes itself a good candidate of observable function. The AMI algorithm for determining optimal time lag τ of the embedding coordinates is

extended and applied to the multivariate input-output system. The average FNN (Cao's method) is also extended and applied to the multivariate input-output system to determine optimal embedding dimension n_{dy} and n_{du}. As a result, a completed Koopman operator-based framework is established for predicting the nonlinear system dynamics. The frequency prediction average RMSE is less than 2% in both Kundur system and IEEE 39-bus system while the voltage predictions present up to 10% RMSE.

- In order to control frequency and voltage, the model predictive control is adopted to cooperate with the Koopman predictor. The resulting system shows very promising performance for damping frequency oscillation under large disturbances. The frequency-KMPC can work with different frequency measurement techniques with/without numerical spikes. The auxiliary voltage-KMPC is capable of reducing voltage sag during faults. The combination of the frequency-KMPC and voltage-KMPC increase the critical clearing time from 0.31s to 0.36s for the Kundur two-area system while the one of IEE 39-bus system is increased from 0.2s to 0.24s.
- In addition, the proposed controllers are robust to system topologies even under the critical topology changes such as the change of the impedance of the critical lines and the change of the heavy loads.
- The KMPC is trained locally. However, it is able to work with another local KMPC located in another area without fighting with each other. This further proves the robustness of KMPC. Meanwhile, CCT is increased by another 7 cycles compared to the system with one DSMS in Kundur two-area system.

8.2 Outlook

- A more advanced control algorithm which can handle different time delay of input and output can be studies.
- An adaptive KMPC can be studies to handle online control with high accuracy.
- The proposed framework is only tested under ideal simulation environment, a further investigation using field data especially the studies in power utilities [91] should be done to test its robustness against the potential noises.

- The proposed framework should be applied to other applications to test its effectiveness such as FACTS devices, synchronous condensers, battery system and etc.
- The proposed DSMS can effectively damp frequency oscillation in the two benchmark systems, but it should also be applied to larger systems to investigate its upper limit of inertia support.

References

[1] J. Dong, G. Xue, M. Dong, and X. Xu, “Energy-saving power generation dispatching in China: Regulations, pilot projects and policy recommendations—A review,” *Renew. Sustain. Energy Rev.*, vol. 43, pp. 1285–1300, Mar. 2015.

[2] M. Dreidy, H. Mokhlis, and S. Mekhilef, “Inertia response and frequency control techniques for renewable energy sources: A review,” *Renew. Sustain. Energy Rev.*, vol. 69, pp. 144–155, Mar. 2017.

[3] J. B. Bushnell, S. P. Holland, J. E. Hughes, and C. R. Knittel, “Strategic Policy Choice in State-Level Regulation: The EPA’s Clean Power Plan,” *Am. Econ. J. Econ. Policy*, vol. 9, no. 2, pp. 57–90, May 2017.

[4] “Updated renewable portfolio standards will lead to more renewable electricity generation - Today in Energy - U.S. Energy Information Administration (EIA).html.” .

[5] C. Mishra, J. S. Thorp, V. A. Centeno, and A. Pal, “Transient Stability Assessment of Cascade Tripping of Renewable Sources Using SOS,” in *2018 IEEE Power & Energy Society General Meeting (PESGM)*, Portland, OR, 2018, pp. 1–5.

[6] Li, Xiawen, Chetan Mishra, and Jaime De La Ree. "Frequency Control of Decoupled Synchronous Machine Using Koopman Operator Based Model Predictive." arXiv preprint arXiv:1901.05341 (2019).

[7] D. E. Olivares *et al.*, “Trends in Microgrid Control,” *IEEE Trans. Smart Grid*, vol. 5, no. 4, pp. 1905–1919, Jul. 2014.

[8] J. Ekanayake and N. Jenkins, “Comparison of the Response of Doubly Fed and Fixed-Speed Induction Generator Wind Turbines to Changes in Network Frequency,” *IEEE Trans. Energy Convers.*, vol. 19, no. 4, pp. 800–802, Dec. 2004.

[9] F. M. Gonzalez-Longatt, “Effects of the synthetic inertia from wind power on the total system inertia: simulation study,” in *2012 2nd International Symposium On Environment Friendly Energies And Applications*, Newcastle upon Tyne, United Kingdom, 2012, pp. 389–395.

[10] Y. Sun, Z. Zhang, G. Li, and J. Lin, “Review on frequency control of power systems with wind power penetration,” in *2010 International Conference on Power System Technology*, Zhejiang, Zhejiang, China, 2010, pp. 1–8.

[11] P. P. Zarina, S. Mishra, and P. C. Sekhar, “Deriving inertial response from a non-inertial PV system for frequency regulation,” in *2012 IEEE International Conference on Power Electronics, Drives and Energy Systems (PEDES)*, Bengaluru, Karnataka, India, 2012, pp. 1–5.

[12] L. Miao, J. Wen, H. Xie, C. Yue, and W.-J. Lee, “Coordinated Control Strategy of Wind Turbine Generator and Energy Storage Equipment for Frequency Support,” *IEEE Trans. Ind. Appl.*, vol. 51, no. 4, pp. 2732–2742, Jul. 2015.

[13] Sakis A. P. Meliopoulos *et al*, “Stability, Protection and Control of Systems with High Penetration of Converter Interfaced Generation,” Power Systems Engineering Research Center, *PSERC Publication 16-03*, March 2016

[14] C. A. Hill, M. C. Such, D. Chen, J. Gonzalez, and W. M. Grady, “Battery Energy Storage for Enabling Integration of Distributed Solar Power Generation,” *IEEE Trans. Smart Grid*, vol. 3, no. 2, pp. 850–857, Jun. 2012.

[15] D. K. Molzahn *et al.*, “A Survey of Distributed Optimization and Control Algorithms for Electric Power Systems,” *IEEE Trans. Smart Grid*, vol. 8, no. 6, pp. 2941–2962, Nov. 2017.

[16] Mayne, David Q., et al. "Constrained model predictive control: Stability and optimality." Automatica 36.6 (2000): 789-814.

[17] F. Allgöwer, R. Findeisen, and Z. K. Nagy, “Nonlinear Model Predictive Control: From Theory to Application,” *Nonlinear Model Predict. Control*, vol. 35, no. 3, p. 17, 2004.

[18] Imhof, Markus. Voltage Source Converter Based HVDC-Modelling and Coordinated Control to Enhance Power System Stability. Diss. ETH Zurich, 2015.

[19] Fuchs, Alexander, et al. "Grid stabilization through VSC-HVDC using wide area measurements." 2011 IEEE Trondheim PowerTech. IEEE, 2011.

[20] Mc Namara, Paul, et al. "Optimal coordination of a multiple HVDC link system using centralized and distributed control." IEEE Transactions on Control Systems Technology 21.2 (2012): 302-314.

[21] Zhang, Junbo, et al. "Power system sensitivity identification—Inherent system properties and data quality." IEEE Transactions on Power Systems 32.4 (2016): 2756-2766.

[22] Bonis, Ioannis, Weiguo Xie, and Constantinos Theodoropoulos. "A linear model predictive control algorithm for nonlinear large‐scale distributed parameter systems." AIChE Journal 58.3 (2012): 801-811.

[23] Lambert, Romain SC, Pedro Rivotti, and Efstratios N. Pistikopoulos. "A Monte-Carlo based model approximation technique for linear model predictive control of nonlinear systems." Computers & Chemical Engineering 54 (2013): 60-67.

[24] S. L. Brunton, B. W. Brunton, J. L. Proctor, and J. N. Kutz, “Koopman invariant subspaces and finite linear representations of nonlinear dynamical systems for control,” *PLOS ONE*, vol. 11, no. 2, p. e0150171, Feb. 2016.

[25] H. Arbabi, M. Korda, and I. Mezic, “A data-driven Koopman model predictive control framework for nonlinear flows,” *ArXiv180405291 Phys.*, Apr. 2018.

[26] S. L. Brunton, B. W. Brunton, J. L. Proctor, E. Kaiser, and J. N. Kutz, “Chaos as an Intermittently Forced Linear System,” *Nat. Commun.*, vol. 8, no. 1, Dec. 2017.

[27] E. Kaiser, J. N. Kutz, and S. L. Brunton, “Data-driven discovery of Koopman eigenfunctions for control,” *ArXiv170701146 Math*, Jul. 2017.

[28] Arbabi, Hassan. "Introduction to Koopman operator theory of dynamical systems." (2018).

[29] Tbaileh, Ahmad Anan. "Power System Coherency Identification Using Nonlinear Koopman Mode Analysis." PhD diss., Virginia Tech, 2014.

[30] S. Hanke, S. Peitz, O. Wallscheid, S. Klus, J. Böcker, and M. Dellnitz, “Koopman Operator Based Finite-Set Model Predictive Control for Electrical Drives,” *ArXiv180400854 Math*, Apr. 2018.

[31] Korda, Milan, Yoshihiko Susuki, and Igor Mezić. "Power grid transient stabilization using Koopman model predictive control." IFAC-PapersOnLine 51.28 (2018): 297-302.

[32] Netto, Marcos. "Robust Identification, Estimation, and Control of Electric Power Systems using the Koopman Operator-Theoretic Framework." PhD diss., Virginia Tech, 2019.

[33] M. Korda and I. Mezić, “Linear predictors for nonlinear dynamical systems: Koopman operator meets model predictive control,” *Automatica*, vol. 93, pp. 149–160, Jul. 2018.

[34] M. B. Kennel, R. Brown, and H. D. I. Abarbanel, “Determining embedding dimension for phase-space reconstruction using a geometrical construction,” *Phys. Rev. A*, vol. 45, no. 6, pp. 3403–3411, Mar. 1992.

[35] Casdagli, Martin. "A dynamical systems approach to modeling input-output systems." SANTA FE INSTITUTE STUDIES IN THE SCIENCES OF COMPLEXITY-PROCEEDINGS VOLUME-. Vol. 12. ADDISON-WESLEY PUBLISHING CO, 1992.

[36] L. Cao, “Practical method for determining the minimum embedding dimension of a scalar time series,” *Phys. Nonlinear Phenom.*, vol. 110, no. 1–2, pp. 43–50, Dec. 1997.

[37] C. Rhodes and M. Morari, “Determining the model order of nonlinear input/output systems directly from data,” in *Proceedings of 1995 American Control Conference - ACC’95*, Seattle, WA, USA, 1995, vol. 3, pp. 2190–2194.

[38] D. M. Walker and N. B. Tufillaro, “Phase space reconstruction using input-output time series data,” *Phys. Rev. E*, vol. 60, no. 4, pp. 4008–4013, Oct. 1999.

[39] R. H. Park, “Two-reaction theory of synchronous machines generalized method of analysis-part I,” *Trans. Am. Inst. Electr. Eng.*, vol. 48, no. 3, pp. 716–727, Jul. 1929.

[40] P. C. Krause, O. Wasynczuk, S. D. Sudhoff, and S. Pekarek, *Analysis of electric machinery and drive systems*, Third edition. Hoboken, New Jersey: Wiley, 2013.

[41] Ong, Chee-Mun. Dynamic simulation of electric machinery using Matlab/Simulink. Prentice-Hall PTR, 1998.

[42] “PSS®E v34.01 manual,” p. 698.

[43] Wang, C., Mishra, C., Thomas, K. Voltage Security Analysis of VSC-HVDC Transmission Lines. In Grid of the Future Symposium, 2018 CIGRE.

[44] Wildi, Theodore. "Electrical machines, drives, and power systems." New Jersey: Upper Saddle River (2002).

[45] Kundur, Prabha, Neal J. Balu, and Mark G. Lauby. Power system stability and control. Vol. 7. New York: McGraw-hill, 1994.

[46] M. Imhof and G. Andersson, “Dynamic modeling of a VSC-HVDC converter,” in *2013 48th International Universities’ Power Engineering Conference (UPEC)*, Dublin, 2013, pp. 1–6.

[47] G. F. Franklin, J. D. Powell, and A. Emami-Naeini, *Feedback control of dynamic systems*, Eighth edition. Ny, NY: Pearson, 2019.

[48] A. Junyent-Ferre, Y. Pipelzadeh, and T. C. Green, “Blending HVDC-Link Energy Storage and Offshore Wind Turbine Inertia for Fast Frequency Response,” *IEEE Trans. Sustain. Energy*, vol. 6, no. 3, pp. 1059–1066, Jul. 2015.

[49] S. H. Strogatz, *Nonlinear dynamics and Chaos: with applications to physics, biology, chemistry, and engineering*. Reading, Mass: Addison-Wesley Pub, 1994.

[50] S. Chen, C. Li, C. Ma, T.-C. Poon, and Y. Zhu, “Phase sensitivity of off-axis digital holography,” *Opt. Lett.*, vol. 43, no. 20, p. 4993, Oct. 2018.

[51] S. Chen and Y. Zhu, “Phase sensitivity evaluation and its application to phase shifting interferometry,” *Methods*, vol. 136, pp. 50–59, Mar. 2018.

[52] Mishra, Chetan. "Studying the Impact of Solar Photovoltaic on Transient Stability of Power Systems using Direct Methods." PhD diss., Virginia Tech, 2017.

[53] R. Sun, M. McVey, D. Yang, and J. R. Stage, “A Study of Synchronous Breaker Switching With Preinsertion Resistor for Capacitors Banks,” *IEEE Trans. Power Deliv.*, vol. 33, no. 2, pp. 821–829, Apr. 2018.

[54] Arbabi, Hassan. "Introduction to Koopman operator theory of dynamical systems.", p.24, (2018).

[55] Wiggins, Stephen. Introduction to applied nonlinear dynamical systems and chaos. Vol. 2. Springer Science & Business Media, 2003.

[56] Chen Wang, Di Wu, Haibo Zeng, and V. Centeno, “CPS based electric vehicle charging directing system design in Smart Grid,” in *2016 IEEE Power & Energy Society Innovative Smart Grid Technologies Conference (ISGT)*, Minneapolis, MN, USA, 2016, pp. 1–5.

[57] C. Wang, “The investment allocation of the distribution system optimization based on an improved PSO,” in *2014 IEEE PES General Meeting | Conference & Exposition*, National Harbor, MD, USA, 2014, pp. 1–5.

[58] D. Yang, Z. Nie, K. Jones, and V. Centeno, “Adaptive decision-trees-based regional voltage control,” in *2017 North American Power Symposium (NAPS)*, Morgantown, WV, 2017, pp. 1–6.

[59] C. Wang, J. Delport, and Y. Wang, “Lateral Motion Prediction of On-Road Preceding Vehicles: A Data-Driven Approach,” *Sensors*, vol. 19, no. 9, p. 2111, May 2019.

[60] D. Yang, “A power system network partition framework for data-driven regional voltage control,” in *2017 North American Power Symposium (NAPS)*, Morgantown, WV, 2017, pp. 1–6.

[61] Yang, Duotong. "A Data Analytics Framework for Regional Voltage Control." PhD diss., Virginia Tech, 2017.

[62] Koopman, Bernard O. "Hamiltonian systems and transformation in Hilbert space." Proceedings of the National Academy of Sciences of the United States of America 17.5 (1931): 315.

[63] M. Budišić and I. Mezić, “Geometry of the ergodic quotient reveals coherent structures in flows,” *Phys. Nonlinear Phenom.*, vol. 241, no. 15, pp. 1255–1269, Aug. 2012.

[64] Y. Lan and I. Mezić, “Linearization in the large of nonlinear systems and Koopman operator spectrum,” *Phys. Nonlinear Phenom.*, vol. 242, no. 1, pp. 42–53, Jan. 2013.

[65] P. Gupta, A. Pal, C. Mishra and T. Wang, “Design of a Coordinated Wide Area Damping Controller by employing Partial State Feedback,” (Accepted in 2019 IEEE Power & Energy Society General Meeting (PESGM), Atlanta, GA, USA).

[66] A. Mauroy and I. Mezic, “Global stability analysis using the eigenfunctions of the Koopman operator,” *ArXiv14081379 Math*, Aug. 2014.

[67] A. Mauroy and I. Mezić, “On the use of Fourier averages to compute the global isochrons of (quasi)periodic dynamics,” *Chaos Interdiscip. J. Nonlinear Sci.*, vol. 22, no. 3, p. 033112, Sep. 2012.

[68] I. Mezic, “On applications of the spectral theory of the Koopman operator in dynamical systems and control theory,” in *2015 54th IEEE Conference on Decision and Control (CDC)*, Osaka, 2015, pp. 7034–7041.

[69] Mezic, Igor. "Koopman operator spectrum and data analysis." arXiv preprint arXiv:1702.07597 (2017).

[70] J. L. Proctor, S. L. Brunton, and J. N. Kutz, “Generalizing Koopman Theory to allow for inputs and control,” *ArXiv160207647 Math*, Feb. 2016.

[71] M. O. Williams, I. G. Kevrekidis, and C. W. Rowley, “A Data–Driven Approximation of the Koopman Operator: Extending Dynamic Mode Decomposition,” *J. Nonlinear Sci.*, vol. 25, no. 6, pp. 1307–1346, Dec. 2015.

[72] Prochazka, Ales, et al. Signal analysis and prediction. Springer Science & Business Media, 2013.

[73] M. Kamb, E. Kaiser, S. L. Brunton, and J. N. Kutz, “Time-Delay Observables for Koopman: Theory and Applications,” *ArXiv181001479 Math*, Sep. 2018.

[74] F. Takens, “Detecting strange attractors in turbulence,” in *Dynamical Systems and Turbulence, Warwick 1980*, vol. 898, D. Rand and L.-S. Young, Eds. Berlin, Heidelberg: Springer Berlin Heidelberg, 1981, pp. 366–381.

[75] J. Stark, “Delay Embeddings for Forced Systems. I. Deterministic Forcing,” *J. Nonlinear Sci.*, vol. 9, no. 3, pp. 255–332, Jun. 1999.

[76] J. Stark, D. S. Broomhead, M. E. Davies, and J. Huke, “Delay Embeddings for Forced Systems. II. Stochastic Forcing,” *J. Nonlinear Sci.*, vol. 13, no. 6, pp. 519–577, Dec. 2003.

[77] Fraser, Andrew M., and Harry L. Swinney. "Independent coordinates for strange attractors from mutual information." Physical review A 33.2 (1986): 1134.

[78] S. Wallot and D. Mønster, “Calculation of Average Mutual Information (AMI) and False-Nearest Neighbors (FNN) for the Estimation of Embedding Parameters of Multidimensional Time Series in Matlab,” *Front. Psychol.*, vol. 9, Sep. 2018.

[79] H. Kantz and T. Schreiber, *Nonlinear time series analysis*, 2nd ed. Cambridge, UK ; New York: Cambridge University Press, 2004.

[80] I. Vlachos and D. Kugiumtzis, “State Space Reconstruction from Multiple Time Series,” in *Topics on Chaotic Systems*, Chania, Crete, Greece, 2009, pp. 378–387.

[81] S. Chen, C. Li, and Y. Zhu, “Sensitivity evaluation of quantitative phase imaging: a study of wavelength shifting interferometry,” *Opt. Lett.*, vol. 42, no. 6, p. 1088, Mar. 2017.

[82] B. Feil, J. Abonyi, and F. Szeifert, “Determining the Model Order of Nonlinear Input-Output Systems by Fuzzy Clustering,” in *Advances in Soft Computing*, J. M. Benítez, O. Cordón, F. Hoffmann, and R. Roy, Eds. London: Springer London, 2003, pp. 89–98.

[83] Mitchell-Colgan, Elliott, Chetan Mishra, and Virgilio A. Centeno. "Optimal wind farm placement considering system constraints and investment and uncertainty costs." In *2015 IEEE Power & Energy Society General Meeting*, pp. 1-5. IEEE, 2015.

[84] C. Mishra, J. S. Thorp, V. A. Centeno and A. Pal, "Stability region estimation under low voltage ride through constraints using sum of squares," *2017 North American Power Symposium (NAPS)*, Morgantown, WV, 2017, pp. 1-6. doi: 10.1109/NAPS.2017.8107353

[85] C. Mishra, J. S. Thorp, V. A. Centeno and A. Pal, "Estimating Relevant Portion of Stability Region using Lyapunov Approach and Sum of Squares," *2018 IEEE Power & Energy Society General Meeting (PESGM)*, Portland, OR, USA, 2018, pp. 1-5. doi: 10.1109/PESGM.2018.8586345

[86] Phadke, Arun G. "Synchronized phasor measurements in power systems." *IEEE Computer Applications in power* 6.2 (1993): 10-15.

[87] A. Pal, C. Mishra, A. K. S. Vullikanti and S. S. Ravi, "General optimal substation coverage algorithm for phasor measurement unit placement in practical systems," in *IET Generation, Transmission & Distribution*, vol. 11, no. 2, pp. 347-353, 1 26 2017. doi: 10.1049/iet-gtd.2016.0553

[88] H. J. Ferreau, C. Kirches, A. Potschka, H. G. Bock, and M. Diehl, “qpOASES: a parametric active-set algorithm for quadratic programming,” *Math. Program. Comput.*, vol. 6, no. 4, pp. 327–363, Dec. 2014.

[89] A. Moeini, I. Kamwa, P. Brunelle, and G. Sybille, “Open data IEEE test systems implemented in SimPowerSystems for education and research in power grid dynamics and control,” in *2015 50th International Universities Power Engineering Conference (UPEC)*, Stoke On Trent, United Kingdom, 2015, pp. 1–6.

[90] Milano, Federico, and Alvaro Ortega. "Frequency divider." *IEEE Transactions on Power Systems* 32.2 (2017): 1493-1501.

[91] Y. Wang, H. Chou, R. Sun, W. Ju, C. Mishra, “Dynamic study of Dominion’s system restoration plan in RTDS,” (Accepted in *2019 IEEE Innovative Smart Grid Technologies (ISGT)*, Washington DC, USA, 2019, USA).